**Department of Precision and Microsystems Engineering**

# Toward 3D printed suspended microchannel resonators

Jikke de Winter



| | | |
|---|---|---|
| Report no | : | 2022.075 |
| Coach | : | dr. ir. T. Manzaneque García |
| Professor | : | dr. M.K. Ghatkesar |
| Specialisation | : | Micro and Nano Engineering |
| Type of report | : | Master thesis |
| Date | : | 18 November 2022 |



100 µm

TU Delft Delft University of Technology

Challenge the future

# Toward 3D printed suspended microchannel resonators

## A study on damping and mass resolution of 3D printed microbeam resonators

by

Jikke de Winter

in fulfillment of the requirements for the degree of Master of Science
in Mechanical Engineering,
at the Department of Precision and Microsystems Engineering,
of the Delft University of Technology.
To be defended publicly on Friday, November 18, 2022 at 13:00 CEST.



| | | |
|---|---|---|
| Student number: | 4716256 | |
| Defence Date: | 18-11-2022 | |
| Thesis Supervisors: | dr. M.K. Ghatkesar, | TU Delft, Supervisor (PME[1]) |
| | dr. ir. T. Manzaneque García, | TU Delft, Daily Supervisor (ME[2]) |



*This thesis is confidential and cannot be made public until 18 November 2023.*
*An electronic version of this thesis is available at http://repository.tudelft.nl/*

[1] Department of Precision and Microsystems Engineering (PME)
[2] Department of Microelectronics (ME)

TU Delft

# Abstract

Mechanical properties of cells are fundamentally connected with (sub)cellular processes and functions. Biosensing of properties like mass, density and stiffness on a single cell level can help in diagnosing diseases. Mass sensing of cells and subcellular components is typically performed with resonant microstructures. Such structures are typically made of silicon-based materials with lithography fabrication technology. Recently, resonant microstructures were fabricated using an emerging 3D printing technique called two-photon polymerization (2PP). This novel fabrication technique yields increased design freedom and a high prototyping speed.

The suspended microchannel resonator (SMR) is a resonant microstructure with an embedded fluidic channel typically used for high throughput buoyant mass sensing of micro-sized particles and cells. SMRs fabricated using 2PP have not yet been mentioned in the literature, providing an opportunity for further development. This work aimed to 3D print an SMR with a sufficient mass resolution to detect the buoyant mass of E. Coli bacteria ($\sim 175\ fg$ in water), in order to demonstrate the potential of 3D printed SMRs.

This was realized by first characterizing the previously unmapped damping in 3D printed polymer microbeam resonators. Characterization was performed across a range of systematic device variations to find the dominating damping sources and fundamentally understand the damping behavior of the 3D printed polymer microbeam resonators. This was followed by maximizing the resonator quality factor, consequently improving mass resolution and finally fabricating an optimized prototype SMR with multi-scale 3D printing accordingly.

The dominant damping source in 3D printed polymer microbeam resonators was identified by eliminating damping sources based on experimental results and theoretical dependencies. It was concluded that bulk friction damping was the dominant damping source for all devices. The damping of the polymer devices showed a strong resonance frequency dependency with record-breaking quality factors up to $1000$ above a resonance frequency of $200\ KHz$. This is in contrast to the state of the art in polymer microbeam resonators, which were evaluated to typically have low quality factors ($< 100$) in matching frequency ranges. Furthermore, methods of improving the quality factor were investigated experimentally. Results showed that thermal post-development treatment did not improve the quality factor of resonators significantly, but it had increased Young's modulus of the polymer material (IP-S) by a factor of 1.5 and also shrank the material substantially. This effect was later incorporated to enhance the quality factor of one specific device design to $1819$, by creating a tensile stress in a narrowed bridge structure. Subsequently, it was concluded that the polymer resonators have a mass resolution advantage over similar silicon-based devices when working in lower quality factor ($Q < 1000$) conditions, due to the low mass density of the polymer material. Finally, prototypes of the suspended microchannel resonator were fabricated with multi-scale 3D printing containing a plug-and-play connection to fluidics and measurement equipment. Their theoretical mass resolution was estimated to be $\leq 60\ fg$, which is sensitive enough to detect E. Coli bacteria (buoyant mass of $\sim 175\ fg$ in water) and compete with conventional fabricated SMRs.

Mapping previously unknown damping of the 3D printed polymer material and exploring treatment methods for changing material properties contribute to general knowledge and future development of 2PP fabricated microstructures. Furthermore, the theoretical sensitivity of the prototype SMR indicates the potential of multi-scale 3D printed SMRs. To conclude, this work paves the path towards actual biosensing 3D printed SMRs with the capabilities of lithography-based fabricated devices, but with additional design and fabrication flexibility.

# Acknowledgements

I would like to express my gratitude to my supervisors Tomás Manzaneque García and Murali Krishna Ghatkesar for their weekly advice, discussions and constructive feedback. Their contribution to this work are of great value. I would like to thank Murali for initialising this project and having a decisive role in terms of the research scope throughout the project. I am thankful for Tomás his guidance and experimental expertise during this project. In addition to that, I would like to thank both for their support and understanding in overcoming personal and research setbacks. Furthermore, I would like to thank my colleague Pieter van Altena for the practical training and lab brainstorming sessions. I am thankful for the practical training and support of Ahmed Sharaf, Daniel Fan and the MNE lab staff. Consequently, I would like to show appreciation to my colleagues Maarten, Qais, Henrie, Damla, Halis, Saleh, Nastaran, Ebrahim, Gürhan and Thijs for creating a positive work environment focused on helping each other and improving research.

Finishing this project and master's degree could not have been possible without the support of my parents Sandra and Walter, my girlfriend Lisanne, all of my friends and family.

*Jikke de Winter*
*Rotterdam, November 2022*

# Contents

**Abstract** i

**Acknowledgements** iii

**Contents** v

**List of Figures** viii

**Nomenclature** ix
- List of Symbols . . . ix
- List of Abbreviations . . . xi
- List of Derived SI units . . . xii

**I Literature review**

**Suspended microchannel resonators: Mass sensing, fabrication methods and characterization** 1
- 1.1 Introduction . . . 3
- 1.2 Mass sensing on the micro-scale . . . 3
  - Different devices for mass sensing . . . 3
  - Resonant cantilever and bridge fundamentals . . . 4
  - Damping . . . 4
  - Suspended microchannel resonator . . . 6
  - Mass resolution limits and measurement speed . . . 6
- 1.3 E.Coli bacteria . . . 6
- 1.4 Multiparameter sensing . . . 7
  - Density sensing . . . 7
  - Stiffness sensing . . . 7
- 1.5 Fabrication techniques . . . 8
  - Techniques used for polymer microbeams . . . 8
  - Two photon polymerization . . . 8
  - Material analysis . . . 8
  - Existing polymer microresonators . . . 9
- 1.6 Research aim . . . 9
  - Experiments . . . 10
  - Milestones and planning . . . 11
- 1.7 References . . . 11

**II Paper**

**Toward 3D printed suspended microchannel resonators** 15
- 2.1 Introduction . . . 17
- 2.2 Damping theory . . . 18
  - Medium interaction damping . . . 18
  - Clamping damping . . . 19
  - Friction damping . . . 19
  - Thermoelastic damping . . . 19
- 2.3 Material and methods . . . 19
  - Resonant beam fabrication . . . 20
  - Pillar fabrication . . . 20

Fluidic interface fabrication . . . 20
Young’s modulus quantification . . . 20
Resonator characterization . . . 21
2.4 Results . . . 21
3D printed microbeam resonators . . . 21
Young’s modulus after post-development treatments . . . 21
Frequency spectra of 3D printed devices . . . 22
Substrate material vs. Quality factor . . . 23
Thermal treatment vs. Quality factor . . . 23
Modelling damping source(s) . . . 24
Thermal treatment of narrowed bridges . . . 24
Suspended microchannel resonator . . . 26
2.5 Discussion . . . 27
Post development treatments . . . 27
Origins of multiple resonance peaks . . . 27
Acoustic mismatch substrate materials . . . 28
Discrepancy damping models and experimental results . . . 28
Dominant damping source . . . 28
Effects of thermal treatment on quality factor . . . 28
State of the art . . . 29
Multiscale 3D printed suspended microchannel resonator . . . 29
2.6 Conclusion . . . 29
2.7 Outlook . . . 30
2.8 References . . . 30

**Conclusion** **33**

**III Appendices** **35**

**Appendix A: Fabrication protocol** **37**
A.1 Introduction . . . 37
A.2 Fluidic interface fabrication . . . 37
A.3 Sputtercoating gold . . . 39
A.4 Suspended microchannel resonator fabrication . . . 39
A.5 2PP printing code . . . 46

**Appendix B: Pillar shrinkage and Young’s modulus experiments** **54**

**Appendix C: Resonator characterization data** **56**

**Appendix D: Resonator deflection** **57**

**Appendix E: Polymer substrates adhesion experiment** **61**
E.1 Methodology . . . 61
E.2 Results and conclusions . . . 62

# List of Figures


(1.1) Single and double clamped resonator microstructures (schematic) . . . 4
(1.2) Suspended microchannel resonator (schematic) . . . 6
(1.3) Photographs and schematic representation of E.Coli bacteria . . . 7
(1.4) Working principle schematic of real-time deformability cytometry . . . 7
(1.5) Acoustic velocity magnitude at node of SMR in second resonant mode . . . 8
(1.6) Polymer cantilever fabrication process steps . . . 8
(1.7) Schematic overview of a two photon polymerization fabrication setup . . . 9
(1.8) Plot of reported polymer microbeam resonators . . . 9
(1.9) Schematic of experimental setup . . . 10
(1.10) Gantt chart of research project . . . 11
(2.11) Polymer microbeam resonators state of the art . . . 18
(2.12) Thick type microbeams consisting of IP-S on Silicon substrates . . . 21
(2.13) Thin type microbeams consisting of IP-S on Silicon substrates . . . 21
(2.14) Thin type narrowed bridge consisting of IP-S on Silicon substrate . . . 21
(2.15) Young's modulus and volumetric shrinkage of IP-S pillars after different post-development treatments . . . 22
(2.16) The frequency spectrum of a thin type cantilever . . . 22
(2.17) The frequency spectrum of a thin type bridge . . . 23
(2.18) The frequency spectrum of a thin type narrowed bridge . . . 23
(2.19) Quality factors of thick cantilevers and thick bridges printed on three different substrate materials . . . 25
(2.20) Quality factors of thick cantilevers, thin cantilevers, thick bridges and thin bridges with and without thermal treatment . . . 25
(2.21) The quality factor of thin type narrowed bridges with and without thermal treatment . . . 26
(2.22) Frequency shift factor F and tensile stress of thin type narrowed bridges of different beam lengths . . . 26
(2.23) Colored electron microscopy image of suspended microchannel resonator . . . 27
(2.24) Schematic cross-section and pictures of SMR and fluidic interface . . . 27
(2.25) State of the art for the performance of polymer microbeam resonators including this work . . . 29

**Appendix A: Fabrication protocol**

(A.1) Fabrication process flowchart for the SMR mounted on top of a plug-and-play fluidic interface. 37
(A.2) Printing tray filled with resin. . . . 38
(A.3) Envisiontec control menu. . . . 38
(A.4) 2PP adapter with 8 fluidic interfaces. . . . 39
(A.5) Sputtercoating gold. . . . 39
(A.6) SMR with named parts: "Dome 1", "Beam" and "Dome 2". . . . 40
(A.7) Adjusted setting in "Hatching" tab. . . . 40
(A.8) Adjusted setting in "Output" tab. . . . 41
(A.9) Removing "FindInterface" commands. . . . 41
(A.10) Programming assembly code. . . . 42
(A.11) Mounted substrate fixed with tape in 2PP substrate holder. . . . 42
(A.12) The graphs at the bottom of the control screen indicate reflected light. . . . 43
(A.13) Surface of the fluidic interface in focus. . . . 44
(A.14) The fluidic channel holes. . . . 44
(A.15) Nearly finished SMR during printing. . . . 45
(A.16) Removing devices from adapter with tweezers. . . . 46
(A.17) Flushing device with connected tube. . . . 46

**Appendix B: Pillar shrinkage and Young's modulus experiments**

(B.1) Volumetric shrinkage visualized: SEM pictures of IP-S pillars after different post-development treatments. Images shown have equal scaling. . . . . . . . . . . . . . . . . . . . . . . . . . . 55
(B.2) Experimental approach for pillar Young's modulus quantification. . . . . . . . . . . . . . . . . 56

**Appendix D: Resonator deflection**
(D.1) Visualized deflection of narrowed bridge 100 $\mu m$ long untreated. . . . . . . . . . . . . . . . . 59
(D.2) Visualized deflection of narrowed bridge 100 $\mu m$ long 200°C - 15 min. . . . . . . . . . . . . 59
(D.3) Visualized deflection of narrowed bridge 150 $\mu m$ long untreated. . . . . . . . . . . . . . . . . 59
(D.4) Visualized deflection of narrowed bridge 150 $\mu m$ long 200°C - 15 min. . . . . . . . . . . . . 59
(D.5) Visualized deflection of narrowed bridge 200 $\mu m$ long untreated. . . . . . . . . . . . . . . . . 60
(D.6) Visualized deflection of narrowed bridge 200 $\mu m$ long 200°C - 15 min. . . . . . . . . . . . . 60
(D.7) Visualized deflection of narrowed bridge 250 $\mu m$ long untreated. . . . . . . . . . . . . . . . . 60
(D.8) Visualized deflection of narrowed bridge 250 $\mu m$ long 200°C - 15 min. . . . . . . . . . . . . 60
(D.9) Visualized deflection of narrowed bridge 300 $\mu m$ long untreated. . . . . . . . . . . . . . . . . 60
(D.10) Visualized deflection of narrowed bridge 300 $\mu m$ long 200°C - 15 min. . . . . . . . . . . . . 60

**Appendix E: Polymer substrates adhesion experiment**
(E.1) Experimental approach for pillar adhesion strength quantification. . . . . . . . . . . . . . . 61
(E.2) Pillar adhesion strength quantification confirmation of detachment. (a) Raw data confirmation of detachment in displacement force plot, arrows show temporal order. (b) Visual confirmation before detachment. (c) Visual confirmation after detachment. . . . . . . . . . 61
(E.3) Pillar adhesion strength for different substrate materials with and without a sputtered gold layer of 2nm. . . . . . . . . . . . . . . . . . . . . . . . . . . . . . . . . . . . . . . . . . . 62

# List of symbols

| | |
|---|---|
| $A$ | Area |
| $a_n$ | Mode constant |
| $C_F$ | Correction factor |
| $c_p$ | Specific heat capacity |
| $d_0$ | Distance beam to substrate |
| $E$ | Stored energy |
| $F$ | Frequency shift factor |
| $F_Q$ | Normalized quality factor |
| $f_{R,n}$ | Resonance frequency at the nth mode |
| $f_0$ | Mean frequency of the entire measurement segment |
| $\bar{f}$ | Average frequency |
| $h$ | Height |
| $I$ | Cross-sectional moment of inertia |
| $k_b$ | Boltzmann constant, |
| $k_eff$ | Effective stiffness |
| $l$ | Length |
| $L_p$ | Peripheral length |
| $m$ | mass |
| $m_eff$ | Effective mass |
| $M_m$ | Molar mass |
| $n$ | Mode number |
| $p$ | Pressure |
| $Q$ | Quality factor |
| $R_{gas}$ | Universal gas constant |
| $SNR$ | Signal-to-noise ratio |
| $T$ | Temperature |
| $T_0$ | Reference temperature |
| $T_1$ | Changed temperature |
| $w$ | Width |
| $X$ | Total number of intervals |
| $Y$ | Young's modulus |
| $Y_r$ | Relaxed Young's modulus |
| $Y_u$ | Unrelaxed Young's modulus |
| $Z$ | Distance of the center of the microchannel from the neutral axis |
| $\bar{Z}$ | Normalized off-axis placement of the channel |
| $z0$ | Specific acoustic impedance |

| | |
|---|---|
| $\alpha$ | Thermal expansion coefficient |
| $\beta$ | Reynolds number |
| $\delta f$ | Standard deviation of frequency fluctuations |
| $\delta m$ | Mass resolution |
| $\Delta E$ | Lost energy |
| $\Delta f$ | Frequency difference |
| $\Delta H$ | Activation energy |
| $\Delta m$ | Mass difference |
| $\Delta Y$ | Difference between relaxed and unrelaxed Young's modulus |
| $\eta$ | Loss coefficient |
| $\kappa$ | Thermal conductivity |
| $\lambda$ | Wavelength |
| $\Lambda_f$ | Frequency score |
| $\mu$ | Dynamic viscosity |
| $\pi$ | Pi constant |
| $\rho$ | Mass density |
| $\sigma$ | Tensile stress |
| $\sigma_A(\tau)$ | Allan deviation |
| $\bar{\tau}$ | Averaged relaxation rate |
| $\bar{\tau}_T$ | Temperature dependent averaged relaxation rate |
| $\tau_c$ | Characteristic amplitude timescale |
| $\tau_e$ | Relaxation rate at constant strain |
| $\tau_s$ | Relaxation rate at constant stress |
| $\tau_{TED}$ | Relaxation rate of thermoelastic damping |
| $\omega$ | Angular frequency |
| $\omega_r$ | Angular resonant frequency |
| $\partial$ | Partial derivative |
| $\Re$ | Mass responsivity |

# List of Abbreviations

| | |
|---|---|
| **2.5D** | Two-and-a-half dimensional |
| **2PP** | Two photon polymerization |
| **3D** | Three-dimensional |
| **DLP** | Digital light processing |
| **E. Coli** | Escherichia Coli |
| **FEM** | Finite element method |
| **LOR** | Lift-off resist |
| **MEMS** | Microelectromechanical system |
| **MNE** | Micro and Nano Engineering department |
| **N.a.N.** | Not a number |
| **NEMS** | Nanoelectromechanical systems |
| **PC** | Personal computer |
| **QCM** | Quartz crystal microbalances |
| **Q-factor** | Quality factor |
| **RNA** | Ribonucleic acid |
| **SEM** | Scanning electron microscope |
| **SMR** | Suspended microchannel resonator |
| **SNR** | Signal-to-noise ratio |
| **TED** | Thermoelastic damping |
| **UV** | Ultraviolet |

# Derived SI Units

**SI Derived Units of Length**

| Multiple | Name | Symbol |
|---|---|---|
| $10^{0}$ | Metre | m |
| $10^{-3}$ | Millimetre | mm |
| $10^{-6}$ | Micrometre | $\mu$m |
| $10^{-9}$ | Nanometre | nm |

**SI Derived Units of Mass**

| Multiple | Name | Symbol |
|---|---|---|
| $10^{3}$ | Kilogram | kg |
| $10^{0}$ | Gram | g |
| $10^{-3}$ | Milligram | mg |
| $10^{-6}$ | Microgram | $\mu$g |
| $10^{-9}$ | Nanogram | ng |
| $10^{-12}$ | Picogram | pg |
| $10^{-15}$ | Femtogram | fg |

# Part I

# Literature review
# Suspended microchannel resonators: Mass sensing, fabrication methods and characterization

# Suspended microchannel resonators: Mass sensing, fabrication methods and characterization

A literature survey report

Jikke de Winter

*Abstract*—**Mechanical properties of cells are fundamentally connected with (sub)cellular processes and functions. Biosensing of properties like mass, density and stiffness on a single cell level can help in diagnosing diseases. Suspended microchannel resonators are an established method for sensing buoyant mass of micro-sized particles and cells. Those devices are typically made of silicon-based materials with semiconductor fabrication technology, yielding the disadvantages of low prototyping speed and 2.5D design space. A novel fabrication technique called two-photon polymerization, has recently been emerging as a 3D printing method with nanoscale resolution and high prototyping speed. Fabrication of polymer suspended microchannel resonators is proposed using this technology. Literature on fundamentals of microbeam resonators has been reviewed to create polymer suspended microchannel resonators with high quality factors, in order to achieve the best performance in terms of mass resolution. The state of the art in polymer microbeam resonators is evaluated to have typically low quality factors ($< 100$) and have not been used for buoyant mass sensing. Mechanical multiparameter sensing of cells is explored for implementation in this device. Experiments will initially be performed on the device to optimize the design and fabrication parameters. Finally, the buoyant mass of E.Coli bacteria will be measured to demonstrate biosensing capability of the device.**

*Index Terms*—**Suspended microchannel resonator, 3D printed, two photon polymerization, polymer microbeam resonator, E.Coli bacteria, mass sensing and multiparameter sensing.**

## I. Introduction

Mechanical biosensing can be of great benefit to the fields of biology and medicine. Research has shown that mechanical properties like mass and stiffness of cells can be linked to a variety of diseases [1]–[5]. For example, blood cells can be distinguished from circulating tumor cells based on their deformability and mass [6]. This label-free method could help with diagnosing and treatment of cancer. Mechanical analysis of biological material on a single cell level has a big potential, but the technology still needs to be improved in order to reach point of care application.

Microelectromechanical systems (MEMS) can be used to measure parameters such as mass and stiffness on a microscale size. These systems often use electrical transducers combined with mechanical moving parts, just like the gyroscope built in a smartphone. Mass sensing with MEMS and NEMS (nanoelectromechanical systems) has reached spectacular resolutions down to the boundary of single atoms [7]. Measuring stiffness of cells still remains a topic of improvement with results typically differing orders of magnitude and low measurement speeds of 1 up to 2000 cells per hour [8]. Simultaneously sensing mass and stiffness with a high throughput still remains a challenge. Mass sensing of cells is commonly performed with resonant cantilevers. A special case is a cantilever with an embedded microfluidic channel, the suspended microchannel resonator (SMR). This yields the advantages of higher throughput of particles and the possibility to operate in a vacuum. Higher quality factors are achieved with vacuum operation by decreasing the viscous drag and damping of air, this is key in achieving a higher mass resolution [9]. Typically SMRs are fabricated out of silicon-based materials using semiconductor manufacturing processes, which can be complex and expensive. These processes also limit geometrical freedom, material choice and prototyping speed. Recently 3D printed cantilevers were fabricated using two-photon polymerisation [10], [11]. Polymer cantilevers with more geometrical freedom can be fabricated using this technique, opening up new possibilities for improvements. Polymers have distinct mechanical properties compared to silicon-based materials, leading to higher intrinsic damping of the resonant cantilevers. This results in a lower measurement sensitivity and a higher measurement speed [12]. High intrinsic damping can be mitigated by inducing tensile stress in double-clamped beams.

Different types of microscale mass sensing will be exhibited in section II. Fundamentals of cantilever-like mass sensing methods will also be discussed here. The basis of damping phenomena in resonant cantilevers will be reviewed leading to the special case of SMRs. Finally, resolution limits and measurement speed caused by those fundamentals will be explained. Section III will discuss E.Coli bacteria and mechanical measurements performed on those bacteria. Section IV will discuss the working principles of different MEMS-based multiparameter sensing methods and their potential to be used in a 3D printed SMR. The two-photon polymerization fabrication technique will be explained in section V. Following by a material analysis of existing photoresists for optimal choice in cantilever material. Finally, section VI will present the research aim; mechanical characterization of E.Coli bacteria using 3D printed suspended microchannel resonators.

## II. Mass sensing on the micro-scale

### *Different devices for mass sensing*

Micro-scale mass sensing is a method of label-free biomolecular detection. Three kinds of mass sensing devices can be identified: Quartz crystal microbalance, surface acoustic wave sensor and mass sensors consisting of microcantilevers or microbridges.

Quartz crystal microbalances utilize the piezoelectric properties of quartz crystal. The crystal plates transduce electrical

energy to mechanical expansion. An alternating current is used to create a resonant standing wave in the microbalance. A change in resonance frequency can be converted into a change of mass by bonded particles on the surface of the microbalance. The typical thickness of the device is in the order of millimeters, which results in a resonance frequency in the order of $10MHz$. The relatively high mass of the device, caused by the thickness, limits the minimal detectable mass. [4].

Surface acoustic wave sensors have a similar working principle compared to QCM's. Surface acoustic wave sensors use piezoelectric crystals to actuate and detect standing acoustic waves in a surface. The increased mass on the surface of the piezoelectric crystal can be measured by a change in the wave velocity of the standing wave. The frequency can get as high as a few $GHz$, however acoustic wave sensors suffer from large damping in liquid submerged operation [4], [13].

Mass sensing with suspended microstructures, such as microcantilevers and microbridges, is shown in Figure 1. This can be executed statically and dynamically. The working principle of static measurements is based on the bending of the cantilever beam due to the added mass or changing surface stress. The cantilever's deflection is measured with optical or electrical detection techniques, while particles are deposited on the surface. Deflection can be converted into mass or surface stress using the stiffness and curvature of the cantilever. Static measurements with microcantilevers are generally performed to determine surface stress by molecular adsorption or biological binding, because deflections due to changing mass can be extremely small [4], [14]. This method is very sensitive to temperature changes, flow and binding of particles causing changes in surface stress.

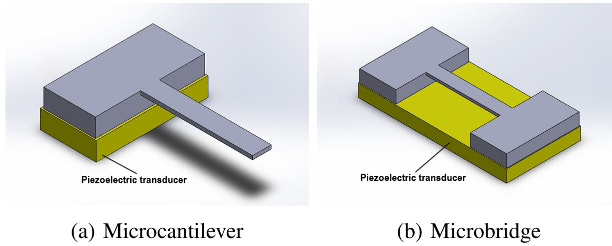


(a) Microcantilever (b) Microbridge

Fig. 1: Single and double clamped resonator microstructures

Dynamic mass sensing with microcantilevers and microbridges is performed using resonant vibration. The microstructure is excited by a piezoelectric actuator at the resonance frequency. This frequency creates an amplitude peak and is most sensitive to changes in mass and stiffness. The displacement of the structure is measured with optical or electrical detection techniques. A change in frequency can be translated to a change in mass, as described by equation 1 for the angular resonant frequency ($\omega_R$) of an undamped mechanical oscillator. Where $k_{eff}$ and $m_{eff}$ are the effective stiffness and effective mass of resonant mode. This project will be focused on dynamic mass sensing, due to its inherent superior resolution.

$$\omega_R = \sqrt{\frac{k_{eff}}{m_{eff}}} \quad (1)$$

*Resonant cantilever and bridge fundamentals*

The theoretical resonance frequency ($f_R$) of cantilevers and bridges can be calculated using equation 2, with the constant $a_n$ from equation 3 with mode number $n = 1, 2, 3, 4, 5..n$ [15], [16]. Mode number 1 is defined as the fundamental frequency. The resonance frequency is related to angular resonant frequency ($\omega_R$) by $\omega_r = 2\pi f_R$. Young's modulus is depicted as $Y$, I as the moment of inertia of the beam's cross-section and $l$ as the length of the beam.

$$f_{R,n} = \frac{a_n^2}{2\pi}\sqrt{\frac{YI}{ml^2}} \quad (2)$$

$$a_n = \begin{cases} 1.875, 4.694, 7.854, 11.0, (n-0.5)\pi & Cantilever \\ 4.7300, 7.8532, 10, 9956, (n+0.5)\pi & Bridge \end{cases} \quad (3)$$

The relation between a change in mass $\Delta m$ and a change in resonance frequency $\Delta f$ can be derived from this equation by assuming $m \gg \Delta m$. The mass of a particle adhered to the resonant sensor is calculated with equation 4 [17].

$$\Delta m = \frac{2m\Delta f}{f_{R,n}} \quad (4)$$

Mass responsivity is an indicator of how sensitive a resonator's frequency is to change in mass. Equation 5 describes the mass sensitivity as a function of the resonant frequency [17]. It can be observed that a higher frequency due to higher resonant modes results in an increased mass responsivity, assuming the stiffness of the microstructure remains constant [16], [18].

$$\Re = \frac{\partial f}{\partial m} \approx -\frac{f_{R,n}}{2m_{eff}} \quad (5)$$

An important performance indicator for resonating mass sensors is the minimal detectable mass, known as mass resolution. The mass resolution $\delta m$ can be calculated with equation 6 adapted from [4]. The mass resolution is not only dependent on frequency and effective mass, but also on the quality factor $Q$, the measured signal-to-noise ratio ($SNR$). The standard deviation of frequency fluctuations is denoted with $\delta f$. Further insight into mass resolution will be given in subsection "Mass resolution limits and measurement speed".

$$\delta m \approx \frac{\delta f}{\Re} = -2m_{eff}\frac{\delta f}{f_{R,n}} \approx -2m_{eff}\frac{1}{Q}\frac{1}{SNR} \quad (6)$$

The quality factor is also considered as a performance indicator for resonating sensors. It is measured by the sharpness of the amplitude peak at a resonance frequency. This sharpness is dependent on the dissipated energy in one cycle at resonance. This leads to the general definition of the quality factor, shown in equation 7. Where $E$ is the stored energy and $\Delta E$ is the dissipated energy in one resonant cycle [19]. Damping is the source of dissipated energy and will be reviewed in the next subsection.

$$Q = 2\pi\frac{E}{\Delta E} \quad (7)$$

*Damping*

The quality factor of a microcantilever or microbridge is determined by the rate of energy dissipation caused by damping. Four groups of damping can be defined: Medium interaction damping, clamping damping, intrinsic damping and other damping. The inverse quality factor of a resonator can be calculated by summing up the inverted quality factors of individual damping sources, see equation 8 [19].

$$\frac{1}{Q} = \frac{1}{Q_{medium}} + \frac{1}{Q_{clamping}} + \frac{1}{Q_{intrinsic}} + \frac{1}{Q_{other}} \tag{8}$$

Medium interaction damping are losses caused by gaseous or fluidic media interacting with the vibrating beam. Clamping damping is caused by energy dissipation at the connection between the beam and the substrate. Intrinsic damping originates from phenomena such as internal friction and thermoelasticity inside the beam material. Other damping sources are caused by electrostatic charges and magnetic fields, which are more affecting resonators using magnetic actuation and electric sensing.

Medium interaction damping can be subdivided into damping by liquid or gas. Damping by surrounding liquid typically results in very small quality factors for microcantilevers and microbridges. This arises from the viscous loading of the beam by the fluid. Quality factors close to unity have been reported at the fundamental resonant mode of microcantilevers, but increasing mode number yields better quality factors up to 30 [20], [21]. Gas damping is dependent on the geometry of the microstructure, vibrational frequency, gas type and gas pressure. A ballistic and a fluidic regime can be defined for the gas interacting with the vibrating beam. In the fluidic regime the gas can be modeled as a continuous fluid and in the ballistic regime, it can be modeled as an exchange of kinetic energy between the gas molecules and the beam. Quality factors can increase orders of magnitude by moving from the fluidic regime to the ballistic regime, as depicted by Schmid et al. in [19]. Pressure dependency of the quality factor is linear, until an intrinsic limit is reached inside the ballistic regime. Vacuum pressure allows the resonator to be operated at this limit, yielding minimal gas damping.

Clamping damping is defined as a transfer of vibrational kinetic energy from the beam to the supporting substrate, this is highly dependent on the geometry of the beam and the substrate. Two equations can be used to approximate the quality factor due to clamping damping of a cantilever resonating at the fundamental mode, see equation 9 [19]. Where $h$, $w$ and $l$ are the cantilever dimensions, subscript $sub$ stands for substrate and $\lambda$ is the wavelength. The clamping damping of a double-clamped bridge resonator, expressed as a quality factor, can be calculated with equation 10 [22]. The factor in front of the brackets is only valid for the fundamental mode and varies per resonant mode. It should be noted that clamping losses increase with the mode number. Generally clamping losses can be reduced by increasing the slenderness of the cantilever and increasing the thickness of the supporting substrate.

$$Q_{clampsc} \approx \begin{cases} 1.05\frac{l}{w}\frac{h_{sub}^2}{h^2}, & h_{sub} \leq \lambda \\ 3.2\frac{l}{w}\left(\frac{l}{h}\right)^4, & h_{sub} > \lambda \end{cases} \tag{9}$$

$$Q_{clampdc} \approx 0.638\left(\frac{l}{h}\right)^3 \tag{10}$$

Intrinsic damping is caused by energy losses inside the beam material. Those losses are dependent on material properties, fabrication processes and temperature. The following loss mechanisms are defined as intrinsic damping: Friction losses, thermoelastic damping and phonon-phonon interaction losses. The latter is an atomic interaction with the strain field, which only occurs in crystalline materials. Friction losses arise from atomic motions which are not reversible. The effect of this loss mechanism depends on a material's relaxation rate $\bar{\tau}$ and the angular frequency of the beam $\omega$. Significant damping occurs when the angular frequency and the relaxation rate are in the same order of magnitude. The relaxation rate at constant strain and constant stress can be calculated with equation 11 and 12. The geometrical average of the relaxation rate can be calculated by $\bar{\tau} = \sqrt{\tau_\epsilon \tau_\sigma}$. The unrelaxed Young's modulus caused by stress $Y_u$ and the relaxed Young's modulus $Y_r$ are related through as $Y_u = Y_r + \Delta Y$. Finally, $\eta$ is the loss coefficient of the beam material. The resulting quality factor for friction losses can be calculated with equation 13 [19].

$$\tau_\epsilon = \frac{\eta}{\Delta Y} \tag{11}$$

$$\tau_\sigma = \tau_\epsilon \frac{Y_r + \Delta Y}{Y_r} \tag{12}$$

$$Q_{friction}^{-1} = \left(\frac{\Delta Y}{\sqrt{Y_r Y_u}}\right)\frac{\omega\bar{\tau}}{1+\omega^2\bar{\tau}^2} \tag{13}$$

Friction losses are also temperature dependent. Changing the temperature can result in significant improvement of the quality factor. This change can be calculated by replacing $\bar{\tau}$ in equation 13 with $\bar{\tau}_T$ from equation 14 [19]. Where $\Delta H$ is the activation energy, $k_B$ the Boltzmann constant, $T_1$ the changed temperature and $T_0$ the reference temperature.

$$\bar{\tau}_T = \bar{\tau}\exp\frac{\Delta H}{k_B}\left(\frac{1}{T_1} - \frac{1}{T_0}\right) \tag{14}$$

Thermoelastic damping is a loss mechanism that is caused by local strain inside the beam material, resulting in local temperature differences. Energy dissipation occurs because of the localized heat flow creating entropy. The relaxation time of thermoelastic damping can be calculated using equation 15 and the quality factor can be calculated using equation 16 [19]. The material properties are denoted with the following variables: Thickness of the beam $h$, specific heat capacity $c_p$, thermal conductivity $\kappa$, thermal expansion coefficient $\alpha$ and $T_0$ is the temperature of the environment.

$$\tau_{TED} = \frac{h^2\rho c_p}{\pi^2\kappa} \tag{15}$$

$$Q_{TED}^{-1} = \left(\frac{Y\alpha^2 T_0}{\rho c_p}\right)\frac{\omega\tau_{TED}}{1+\omega^2\tau_{TED}^2} \tag{16}$$

Surface friction is a loss phenomenon caused by imperfections and roughness of the beam top and bottom surfaces. This damping phenomenon can become dominant when the beam's thickness is below a micrometer and the surface-to-volume ratio is high [19].

*Suspended microchannel resonator*

The suspended microchannel resonator is a special kind of microbeam resonator with an embedded microfluidic channel, shown in Figure 2. This design can measure cells and biological molecules without requiring a fluid to surround the cantilever. Even vacuum operation is possible using this design, which leads to a large reduction of damping by surrounding gasses or fluids. Previous research has shown an increase of 3 orders of magnitude in Q-factor, using an SMR in a vacuum instead of liquid [9]. The device still experiences a small damping caused by the liquid inside the embedded channel, which can be calculated as a Q-factor of the first resonant mode with equation 17 [23]. This equation is derived with the following assumptions: Incompressible flow inside the microchannel, the oscillation amplitude is smaller than the cantilever length, the length of the cantilever is much larger than the width and height and the microchannel width is larger than the microchannel height.

$$Q_{liq} = F_Q(\beta)\left(\frac{\rho_{average}}{\rho_{liq}}\right)\left(\frac{h}{h_c}\right)\left(\frac{w}{w_c}\right)\left(\frac{l}{h_c}\right)^2 \quad (17)$$

The average mass density of the whole cantilever including fluid is depicted as $\rho_{average}$, the mass density of the fluid as $\rho_{liq}$, the height as $h$ width as $w$ and the length as $l$. Subscript $_c$ denoted the internal channel and $liq$ the liquid environment. $F_Q$ is the normalized Q-factor and $\beta$ is the Reynolds number both can be calculated in equation 18 and 19 respectively [23].

$$F_Q(\beta) = \begin{cases} \frac{38.73\beta}{\beta^2+564.6\bar{Z}^2\left(1+\frac{\beta^2}{8400}\right)}, & \beta \to 0 \\ \frac{\sqrt{\beta}}{6.573+1.718\bar{Z}^2}, & \beta \to \infty \end{cases} \quad (18)$$

$$\beta = \frac{\rho_{liq}\omega h_{liq}^2}{\mu_{liq}} \quad (19)$$

In equation 18, normalized off-axis placement of the channel is defined as $\bar{Z} = Z/h_{liq}$, where $Z$ is the deviation of the center of the microchannel from the neutral axis of the cantilever. The shear viscosity of the liquid is depicted as $\mu_{liq}$ in equation 19.

*Mass resolution limits and measurement speed*

Mass resolution is a performance indicator for mass sensors and describes the minimal detectable mass of the device. As described in equation 6, the mass resolution is dependent on the measured frequency noise, $\delta f$. This noise is typically quantified by the Allan deviation $\sigma_A(\tau)$. *"The Allan deviation is calculated by averaging subsequent sections of the normalized frequency data of length $\tau$, and then taking the difference between the means of contiguous segments"*, see equation 20 [24]. The average frequency of each measurement is denoted by $\bar{f}$ and the mean frequency of the entire measurement segment is $f_0$. Each interval is denoted with subscript $j$ and the total number of intervals is denoted with $X$.

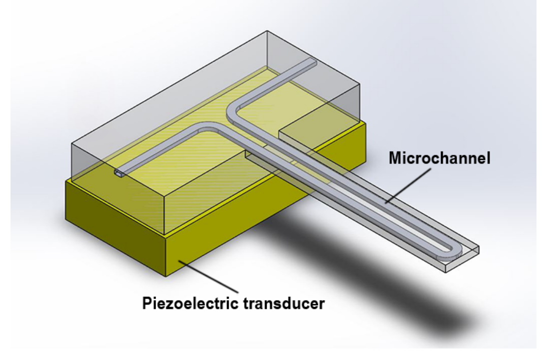


Fig. 2: Suspended microchannel resonator

$$\sigma_A(\tau) = \sqrt{\sigma_A^2(\tau)} \approx \sqrt{\frac{1}{2(X-1)}\sum_{j=2}^{X}\left(\frac{\bar{f}_j - \bar{f}_{j-1}}{f_0}\right)^2} \quad (20)$$

The mass resolution of a device can be calculated by substituting the Allan deviation in equation 6 for $\frac{\delta f}{f_{R,n}}$, see equation 21 for the resulting definition [25], [26].

$$\delta m \approx \frac{\delta f}{\Re} = 2m_{eff}\frac{\delta f}{f_{R,n}} = 2m_{eff}\sigma_A(\tau) \quad (21)$$

Improved mass resolutions can be achieved with tactics different than increasing frequency, reducing damping and minimizing beam mass. Operating the beam just below the onset of non-linearity is a tactic to increase mass resolution. A decreasing Allen deviation is achieved by increasing the driving power without extra noise of non-linear effects. Non-linear jumps in frequency amplitude around the resonant frequency make the device more sensitive to changes in mass [27]. Simultaneous excitation of the beam at multiple resonant modes has proven to decrease mass resolutions and increase measurement speed [28]. Operating the device with closed-loop control is a tactic for improving measurement speed. Open-loop operation limits the measurement speed to the characteristic amplitude timescale $\tau_c = \frac{Q}{\pi f_{R,n}}$. On the contrary, closed-loop operation such as frequency-locked loop and self-sustaining oscillator has a flexible trade-off characteristic between the quality factor and measurement speed [29]. User-defined bandwidth can be set using these closed-loop control techniques.

## III. E.Coli bacteria

Escherichia Coli is a bacterial species commonly known as a pathogen causing food poisoning, diarrhea and urinal tract infections. Only certain strains are responsible for those diseases, while most strains are non-pathogenic [30]. Globally 1 million foodborne diseases and 135 million urinal tract infections are estimated to be caused by E.Coli bacteria every year [31]–[33]. The shape of an E.Coli bacterium is typically cylindrical with rounded ends, see Figure 3. Sizes vary between 1.0 and 6.0 $\mu m$ long and 0.5 and 1.5 $\mu m$ in diameter [30], [34], [35]. The dry mass of a single E.Coli bacterium is 0.30 $pg$, mainly determined by its proteins and

RNA [35]. The wet mass of the cell is estimated to be 1 $pg$ of which water is roughly 70% [35].

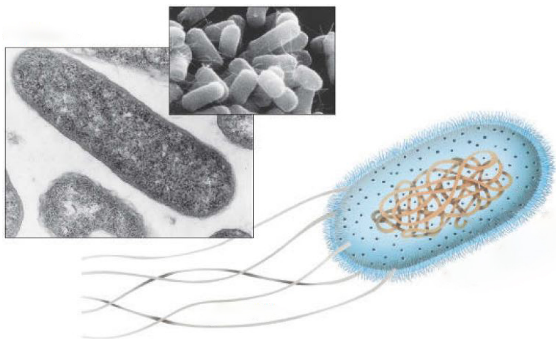

Fig. 3: Photographs and schematic representation of E.Coli bacteria, adapted from [34].

Not the mass but the buoyant mass of particles and cells is measured with suspended microchannel resonators, because of the required fluidic medium. Buoyant mass $m_b$ of a cell can be calculated with equation 22 [36]. The cell mass is denoted by $m_c$ and the mass density of the cell by $\rho_c$. The mass density of E.Coli bacteria (1.2 $kg/l$) is close to the mass density of water (1.00 $kg/l$), which is typically used as a medium for suspending living E.Coli bacteria [37], [38]. This makes measuring their buoyant mass challenging. The buoyant mass of E.Coli bacteria is measured in water-based salt solutions (mass density $\approx$ 1.01 $kg/l$) in previous work: 110 $\pm$ 30 $fg$, 75-210 $fg$ and 175 $fg$ average. [37], [39], [40]

$$m_b = m_c \left(1 - \frac{\rho_{liq}}{\rho_c}\right) \tag{22}$$

## IV. Multiparameter sensing

Change in physical and mechanical properties of cells are fundamentally connected with (sub)cellular processes and functions [35], [41]. Mechanical biosensing of single cell properties like mass, density and stiffness have been proven to indicate disease, aging and cell differentiation [36], [42], [43]. Measurement of those properties simultaneously would provide even more information. This section discusses existing biosensing methods for measuring density and stiffness. Different methods of single and multiparameter sensing will be reviewed to evaluate their potential for implementation in a 3D printed suspended microchannel resonator.

### *Density sensing*

Cell density can be used to accurately characterize cells when they have a similar mass or volume [44]. Density measurements of cells in SMR's are performed with different methods, but all of those methods rely on a single fundamental principle. The buoyant mass of the cell is measured in minimally two fluids with differing densities. The cell density can be calculated by rearranging equation 22 into equation 23, assuming the cell mass remains constant. The first and second measurement with different fluid densities are denoted with subscripts 1 and 2.

$$\rho_c = \frac{m_{b2}}{m_{b1}} \frac{\rho_{liq1}}{\rho_{liq2}} \tag{23}$$

Typically such experiments are performed with a single SMR pushing a cell forward and back in different fluids [36], [45]. This fluid switching for each cell limits the measurement speed. The second approach is to use two SMR's in parallel and mix the different fluids in between the two SMR's [44]. The main disadvantage of this method is the occurring fluid density uncertainty and error due to mixing.

### *Stiffness biosensing*

Mechanical sensing of stiffness is not a quantitatively reliable field of measurements. Recent research has compared the elasticity of human breast cancer cells with seven measurement technologies and concluded a 1000-fold variation in results between those technologies [8]. This can be accounted to differences in position on cell, deformation rates, probe geometry and applied forces. Measuring cell stiffness with technologies such as atomic force microscopy, particle tracking microrheology, parallel plate rheology and stretching with optical tweezers can be quite invasive [46]. Those measurement strategies seem too fundamentally different for implementation in a 3D printed SMR. However a few techniques stand out in terms of invasiveness and implementation potential.

The first technique is to implement a constriction in the embedded microchannel of the SMR around the apex [6]. This strategy determines deformability by measuring the passage time for a cell to squeeze through the constriction. The passage time is not only dependent on the deformability but also on the cell size, cell orientation and friction of the cell with the constriction wall. Buoyant mass is simultaneously measured with this technique, which can be used to account for differences in cell size. Implementing this multiparameter sensing technique in a 3D printed SMR seems rather feasible.

Real-time deformability cytometry is a technique with high throughput, capable of measuring large cell populations ($> 10^5$ cells) [47], [48]. This technique utilizes a fluidic constriction larger than the cell to deform it hydrodynamicly at high flow speeds, see Figure 4. The deformability is measured with optical imaging and fitted to theoretical models. The required transparent fluidic channel for optical imaging is a disadvantage for implementation in a 3D printed SMR, where a non-transparent beam is necessary for its buoyant mass detection technique. Possibility of scaling down and adjusting to the shape of E.Coli bacteria are also concerns for application of real-time deformability cytometry in this research project.

It has been shown that size-normalized acoustic scattering in a SMR, measures a cells stiffness in a non-invasive way [46]. A point with a zero vibrational amplitude (node) will appear by operating the SMR in the second resonant mode, see Figure 5. Change in mass will not result in a change in resonant frequency at this point. Nonetheless a shift in resonant frequency is observed due to acoustic scattering from the surface of the measured cells. This acoustic scattering is dependent on acoustic interactions with the deforming cell at

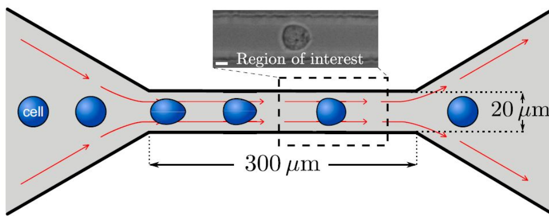


Fig. 4: Working principle schematic of real-time deformability cytometry, adapted from [48].

the node. Which means the resonant frequency shift at the node of the SMR is dependent on the global stiffness of the cell. Buoyant mass is simultaneously measured, which can be used to account for differences in cell size. This multiparameter sensing technique can be implemented readily in a 3D printed SMR, since no design changes are necessary.

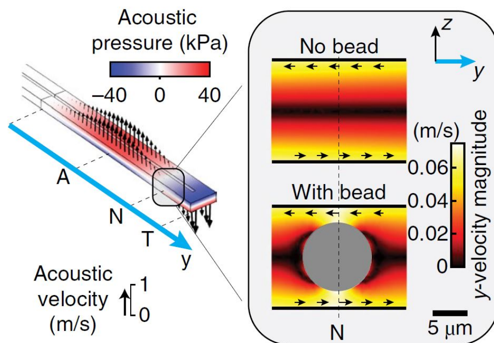


Fig. 5: Acoustic velocity magnitude at node of SMR in second resonant mode, adapted from [46].

## V. Fabrication techniques

Microscale fabrication techniques used for MEMS originate from the semiconductor industry [49]. Bulk and surface micromachining are the most important MEMS fabrication techniques, typically using silicon or silicon-based materials. Devices are formed out of a silicon wafer or devices are formed on top of the wafer. Patterns are created on top of the material by illuminating a photoresists through masks. The devices are formed by etching out those patterns. Microcantilevers and microbridges are also fabricated from silicon-based materials. Creating the embedded channel of SMRs can make the fabrication process more challenging with extra steps often using sacrificial materials. This type of fabrication has a 2.5D design space and a low prototyping speed, due to the design-specific masks.

This section will focus on the fabrication of polymer microbeams and SMRs. Conventional and novel techniques will be discussed. Theoretical analysis will be performed to help determine the right material for the best device performance. Finally, existing polymer microresonators will be compared to identify the state of the art.

### *Techniques used for polymer microbeams*

Polymer microbeams are typically fabricated with surface micromachining on top of a silicon or glass substrate. Figure 6 shows the process steps for the fabrication of a SU-8 polymer cantilever with surface micromachining. The first step is to deposit lift-off resist and SU-8 on top of the glass wafer with spin-coating. An illuminated mask is used to cure a pattern in the photosensitive polymer layer during the second step. The third step shows the etching of the lift-off resist to detach the cantilever from the substrate. A complex process with more steps is needed to fabricate devices with more layers, different geometries or an embedded channel. This technique is limited to the fabrication of photopolymer devices and 2.5D geometries. Fabrication techniques like micro injection molding, vacuum injection molding and solvent casting have been used to create devices out of different polymers [50]–[53].

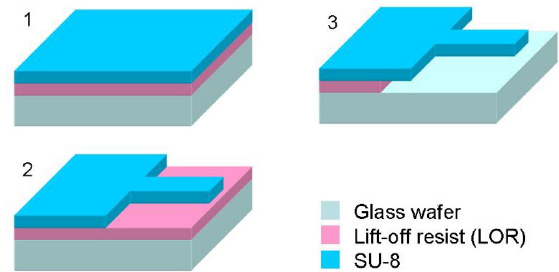


Fig. 6: Polymer cantilever fabrication process steps, adapted from [54].

### *Two photon polymerization*

Two-photon polymerization is an emerging three-dimensional micro and nano lithography fabrication technique. A wide range of research fields such as biomedical engineering, microfluidics and photonics have benefited from the possibilities created using this technique [55], [56]. A schematic overview of the fabrication setup is given in Figure 7. Structures are formed on the surface of the substrate, by focusing an infrared laser on small volumes inside the photoresist. Two-photon adsorption of the photon initiator molecules triggers a chemical reaction forming the polymer in a cigar-shaped volume [55]. Structures are formed by moving the focal point of the laser or using the 3D stage. Resolutions of tens of nanometers can be achieved by using femtosecond laser pulses and magnifying objectives [57], [58]. Rapid prototyping and a 3D design space are major advantages of this technique. The disadvantage of this technique are the available materials, having a typical Young's modulus below 5 $GPa$ and high friction damping.

### *Material analysis*

The available photoresists used in two-photon polymerization have variating material properties, which should be accounted for when picking a fabrication material. A material analysis will be performed in this subsection to determine the

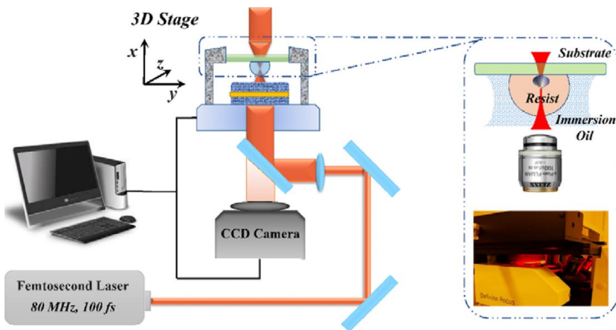


Fig. 7: Schematic overview of a two-photon polymerization fabrication setup, adapted from [55].

optimal material for the fabrication of a microbeam resonator with an embedded channel. Interpretation of equation 5 for mass sensitivity and equation 6 for mass resolution, leads to the conclusion that the resonant frequency and quality factor should become as high as possible for excellent performance. Scoring values will be created and derived from these two requirements, purely based on material properties. The first scoring value is based on maximizing the resonance frequency which is dependent on two material properties, see equation 24 for the frequency score denoted with $\Lambda_f$. Note that this score is derived from equation 2, by eliminating the geometric parameters and preserving the material properties

$$\Lambda_f = \sqrt{\frac{Y}{\rho}} \tag{24}$$

The quality factor is dependent on multiple damping mechanisms, which makes the quality factor score more complicated. The damping mechanisms for a polymer microbeam with an embedded channel, influenced by material properties are: Friction losses, thermoelastic losses and liquid inside resonator damping. See equation 25 for the material intrinsic quality factor $Q_{intrinsic}$. Note that this material's intrinsic quality factor is the total quality factor of friction losses and thermoelastic losses at their relaxation rate for maximal damping. Liquid inside resonator damping is eliminated since it is less dependent on material properties ($Q_{liq} \sim \rho$) and more dependent on the geometric properties of the device and hydrodynamic operating conditions.

$$Q_{intrinsic} = \left(\frac{1}{Q_{friction}(\omega)} + \frac{1}{Q_{TED}(\omega)}\right)^{-1} \tag{25}$$

Table I summarizes the material scoring values of five common photoresists. Unavailable data of mechanical and thermal properties cause the incomplete quality factor values, denoted with N.a.N. (not a number). IP-S is the best-scoring material for the fabrication of the SMR, but has the disadvantage of a relatively lower printing resolution due to the maximal objective magnification (25).

*Existing polymer microresonators*

Polymer microbeam resonators are not a recent development, but the applications are generally limited to the field of

TABLE I: Material analysis scoring values

| Material | $\Lambda_f$ [m/s] | $Q_{friction}$ [-] | $Q_{TED}$ [-] | Source |
|---|---|---|---|---|
| IP-DIP | 1497 | 13.2 | NaN | [59], [60] |
| IP-L 780 | 1938 | 14.5 | NaN | [60] |
| IP-S | 2073 | 20.5 | NaN | [11], [60] |
| SU-8 | 1845 | NaN | NaN | [61] |
| Ormocomp | 1191 | NaN | NaN | [60] |

research [53], [62]. They were developed for applications such as scanning probe microscopy, chemical sensing, biological sensing, humidity sensing and cellular handling [11], [63], [64]. The existing reports of polymer microbeam resonators will be reviewed based on their dimensions, operating conditions and performance. The performance will be indicated with frequency and quality factor displayed in Figure 8. Table II summarizes the beam material, performance, dimensions, measurement environment and beam type of reported polymer microbeam resonators. It should be noted that the pre-stressed bridge resonators have outstanding quality factors compared to the other microbeam resonators. The pre-stressed bridge resonators have an added tensile stress (axial direction) in the beam structure. The tensile stress $\sigma$ is utilized to enhance the quality factor which can be calculated with equation 26 [68]

$$Q_{Stressed} = \left(\frac{(n\pi)^2}{12}\frac{Y}{\sigma}\left(\frac{h}{l}\right)^2 + \frac{1}{\sqrt{3}}\sqrt{\frac{Y}{\sigma}}\frac{h}{l}\right)^{-1} Q_{friction} \tag{26}$$

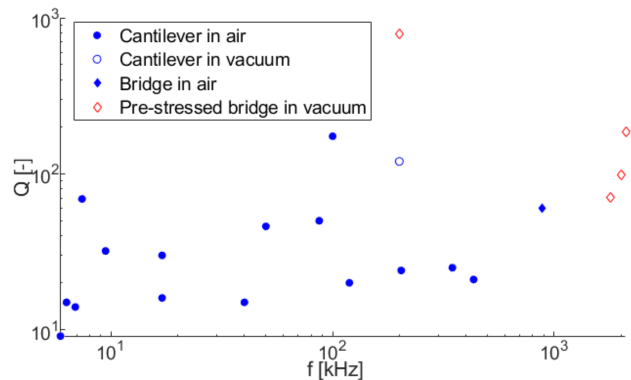


Fig. 8: Plot of reported polymer microbeam resonators with frequency on the x-axis and quality factor on the y-axis.

## VI. Research aim

The aim of the research subsequent to this literature review is displayed in this section. The research question is defined as: "What is the smallest mass resolution of a 3D printed polymer suspended microchannel resonator designed to detect E.Coli bacteria?" The following sub-questions are essential for answering the research question:

- Is buoyant mass sensing of E.Coli bacteria possible with a 3D printed suspended microchannel resonator?
- What is the optimal device geometry for sensing E.Coli bacteria?

TABLE II: Beam material, performance, dimensions, environment and beam type of reported polymer microbeam resonators

| Material | $f_r$ [kHz] | Q-factor [-] | Length [$\mu m$] | Width [$\mu m$] | Thickness [$\mu m$] | Environment | Beam type | Source |
|---|---|---|---|---|---|---|---|---|
| SU-8 | 87 | 50 | 150 | 31 | 6.6 | Air | Cantilever | Genolet, 1999 [62] |
| PS | 5.88 | 9 | 500 | 50 | 2 | Air | Cantilever | McFarland, 2004 [65] |
| PS | 6.3 | 15 | 500 | 50 | 1.5 | Air | Cantilever | McFarland, 2004 [65] |
| PS | 9.45 | 32 | 500 | 50 | 1 | Air | Cantilever | McFarland, 2004 [65] |
| PS | 7.4 | 69 | 572 | 128 | 8.9 | Air | Cantilever | McFarland, 2004(2) [52] |
| UVO-114 | 6.9 | 14 | 1500 | 100 | 50 | Air | Cantilever | Xu, 2004 [50] |
| SU-8 | 40 | 15 | 100 | 20 | 1.5 | Air | Cantilever | Calleja, 2005 [66] |
| SU-8 | 17 | 16 | 200 | 20 | 1.5 | Air | Cantilever | Calleja, 2005 [66] |
| SU-8 | 17 | 30 | 500 | 100 | 10 | Air | Cantilever | Mouaziz, 2006 [51] |
| PMMA | 2100 | 185 | 40 | 10 | 0.64 | Vacuum | Pre-stressed bridge | Zhang, 2007 [67] |
| PMMA | 2000 | 99 | 40 | 10 | 0.64 | Vacuum | Pre-stressed bridge | Zhang, 2007 [67] |
| PMMA | 1800 | 71 | 40 | 10 | 0.64 | Vacuum | Pre-stressed bridge | Zhang, 2007 [67] |
| SU-8 2000 | 200 | 120 | 185 | 12 | 1.45 | Vacuum (0.05 Pa) | Cantilever | Schmid, 2009 [54] |
| SU-8 2000 | 200 | 790 | 300 | 14 | 1.45 | Vacuum (0.05 Pa) | Pre-stressed bridge | Schmid, 2009 [54] |
| PP | 50 | 46 | 500 | 100 | 40 | Air | Cantilever | Urwyler, 2011 [53] |
| SU-8 | 880 | 60 | 200 | 20 | 20 | Air | Bridge | Accoto, 2014 [61] |
| SU-8 | 347 | 25 | 80 | 20 | 7 | Air | Cantilever | Hosseini, 2019 [12] |
| IP-DIP | 433 | 21 | 100 | 10 | 10 | Air | Cantilever | Frehner, 2018 [10] |
| IP-DIP | 204 | 24 | 100 | 5 | 5 | Air | Cantilever | Frehner, 2018 [10] |
| IP-DIP | 119 | 20 | 100 | 2 | 2 | Air | Cantilever | Frehner, 2018 [10] |
| IP-S | 100 | 174 | 350 | 30 | 30 | Air | Cantilever | Kramer, 2020 [11] |

- What is the dominant damping mechanism in 3D printed microbeam resonators?

Three types of suspended microchannel resonators will be designed and fabricated: Cantilevers, bridges and pre-stressed bridges. Fabrication of the pre-stressed bridge will be a challenging part of the project. The tensile stress will be applied during fabrication by quenching or incorporating the shrinkage of two-photon polymerization. Performing experiments on the fabricated devices will help answer the main and sub-questions. The methods and goals of the experiments will be described in the next subsection. Finally, the project milestones and planning will be shown in the last subsection.

*Experiments*

Experiments will be performed once successful fabrication of the suspended microchannel resonators is achieved. Five experiments are devised to help answer the research question and sub-questions. Each experiment will be performed using the experimental setup shown in Figure 9. The figure shows an SMR (sample) mounted on top of a piezoelectric actuator inside a temperature-controlled vacuum chamber. A laser Doppler vibrometer is used to optically detect the deflection of the SMR through the sight glass. The deflection will be processed in the PC to determine the amplitude and frequency of the device. The microfluidic channel is connected to the SMR for the supply and discharge of fluid and cells. The device can be controlled in closed-loop with feedback from the laser Doppler vibrometer. The first experiment will be performed to achieve a baseline and compare the performance of the three device types (cantilever, bridge and pre-stressed bridge). The performance will be measured as a quality factor at different resonant modes. The devices will be operated at room temperature, at high vacuum and without fluid inside. The second experiment will be performed to determine the influence of fluid inside the embedded channel on the performance of the devices. The quality factor will be measured at different resonant modes with different fluid flow speeds. Operating conditions will be at room temperature and high

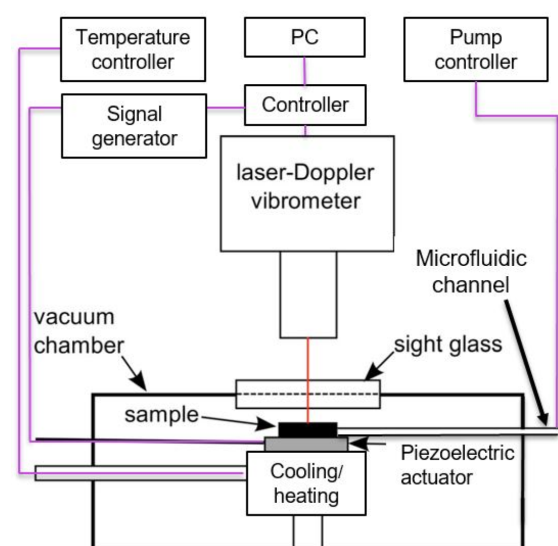


Fig. 9: Schematic of experimental setup, edited figure from [63]

vacuum. The goal of the third experiment is to determine whether the dominant type of damping in each device is clamping or intrinsic damping, but also to find an optimal operating temperature. Clamping damping is dependent on the geometry of the device and substrate, while intrinsic damping is dependent on temperature among other things. The quality factor of the devices will be measured at different temperatures between -40 °C up to 100°C and at different resonant modes. The devices will be operated at high vacuum and without fluid inside. The fourth experiment will help to characterize the mass resolution, calibrate the best-performing device and find the highest measurement speed. This will be performed by measuring the buoyant mass of microparticles in closed-loop control with different gate times. The device will be operated at optimal temperature and at high vacuum. Finally, the fifth

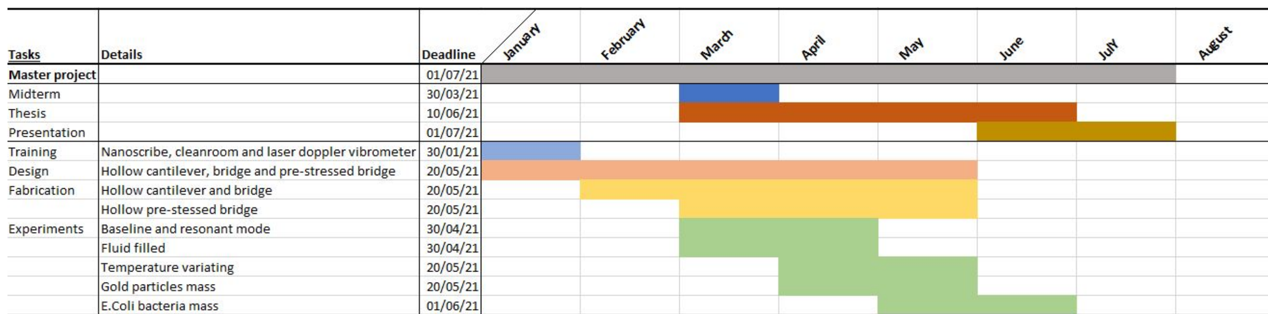


Fig. 10: Gantt chart of research project

experiment will be performed to demonstrate biological mass sensing capabilities using E.Coli bacteria. The mass of those bacteria will be measured under the same operating conditions as the microparticles, except the prerequisite that temperature should be kept between 0°C and 55°C to keep the E.Coli bacteria alive.

*Milestones and planning*

The following milestones are defined to keep track of progress and accomplishments during the research project:

- Fabrication of hollow microcantilevers and micro bridges
- Fabrication of pre-stressed microbridges
- Measure mass of microparticles
- Demonstrate biosensing capability with E.Coli bacteria

A Gantt chart is used to have a planned approach in executing the research project, see Figure 10. The project starts in January with lab equipment training and design. Fabrication starts in February and can take up until May with design improvements gained from experiments. The previously described experiments will start in March and will take until the start of June. Early results will be presented during the midterm evaluation in March. The thesis will be written throughout the project starting in March. Finally, the results and conclusions will be presented at the beginning of July.

## Acknowledgment

I would like to express my gratitude to my supervisors Tomás Manzaneque Garcia and Murali Krishna Ghatkesar for their weekly advice and constructive feedback. Their contribution to this work and the upcoming research project are of great value. I would like to thank Murali for initialising this project and having a decisive role in terms of the research aim. I am thankful for Tomás his patience en encouragement in reviewing my work throughout this project.

## References

[1] S. E. Cross, Y.-S. Jin, J. Rao, and J. K. Gimzewski, "Nanomechanical analysis of cells from cancer patients," *Nature nanotechnology*, vol. 2, no. 12, pp. 780–783, 2007.

[2] U. F. Greber, "Virus and host mechanics support membrane penetration and cell entry," *Journal of virology*, vol. 90, no. 8, pp. 3802–3805, 2016.

[3] S. Suresh, J. Spatz, J. Mills, A. Micoulet, M. Dao, C. Lim, M. Beil, and T. Seufferlein, "Reprint of: connections between single-cell biomechanics and human disease states: gastrointestinal cancer and malaria," *Acta biomaterialia*, vol. 23, pp. S3–S15, 2015.

[4] A. De Pastina and L. G. Villanueva, "Suspended micro/nano channel resonators: a review," *Journal of Micromechanics and Microengineering*, vol. 30, no. 4, p. 043001, 2020.

[5] E. Gil-Santos, J. J. Ruz, O. Malvar, I. Favero, A. Lemaître, P. M. Kosaka, S. García-López, M. Calleja, and J. Tamayo, "Optomechanical detection of vibration modes of a single bacterium," *Nature nanotechnology*, pp. 1–6, 2020.

[6] S. Byun, S. Son, D. Amodei, N. Cermak, J. Shaw, J. H. Kang, V. C. Hecht, M. M. Winslow, T. Jacks, P. Mallick *et al.*, "Characterizing deformability and surface friction of cancer cells," *Proceedings of the National Academy of Sciences*, vol. 110, no. 19, pp. 7580–7585, 2013.

[7] J. Chaste, A. Eichler, J. Moser, G. Ceballos, R. Rurali, and A. Bachtold, "A nanomechanical mass sensor with yoctogram resolution," *Nature nanotechnology*, vol. 7, no. 5, pp. 301–304, 2012.

[8] P.-H. Wu, D. R.-B. Aroush, A. Asnacios, W.-C. Chen, M. E. Dokukin, B. L. Doss, P. Durand-Smet, A. Ekpenyong, J. Guck, N. V. Guz *et al.*, "A comparison of methods to assess cell mechanical properties," *Nature methods*, vol. 15, pp. 491–498, 2018.

[9] T. P. Burg, A. R. Mirza, N. Milovic, C. H. Tsau, G. A. Popescu, J. S. Foster, and S. R. Manalis, "Vacuum-packaged suspended microchannel resonant mass sensor for biomolecular detection," *Journal of Microelectromechanical Systems*, vol. 15, no. 6, pp. 1466–1476, 2006.

[10] L. Frehner and D. Maillard, "Optimization of channel design and fabrication for suspended microchannels resonators with a 3d nanoprinter," Tech. Rep., 2018.

[11] R. C. Kramer, E. J. Verlinden, L. Angeloni, A. Van Den Heuvel, L. E. Fratila-Apachitei, S. M. Van Der Maarel, and M. K. Ghatkesar, "Multiscale 3d-printing of microfluidic afm cantilevers," *Lab on a Chip*, vol. 20, no. 2, pp. 311–319, 2020.

[12] N. Hosseini, M. Neuenschwander, O. Peric, S. H. Andany, J. D. Adams, and G. E. Fantner, "Integration of sharp silicon nitride tips into high-speed su8 cantilevers in a batch fabrication process," *Beilstein Journal of Nanotechnology*, vol. 10, no. 1, pp. 2357–2363, 2019.

[13] K. Länge, B. E. Rapp, and M. Rapp, "Surface acoustic wave biosensors: a review," *Analytical and bioanalytical chemistry*, vol. 391, no. 5, pp. 1509–1519, 2008.

[14] L. Senesac and T. Thundat, "Explosive vapor detection using microcantilever sensors," in *Counterterrorist Detection Techniques of Explosives*. Elsevier, 2007, pp. 109–130.

[15] A. Cleland and M. Roukes, "Noise processes in nanomechanical resonators," *Journal of applied physics*, vol. 92, no. 5, pp. 2758–2769, 2002.

[16] M. K. Ghatkesar, V. Barwich, T. Braun, J.-P. Ramseyer, C. Gerber, M. Hegner, H. P. Lang, U. Drechsler, and M. Despont, "Higher modes of vibration increase mass sensitivity in nanomechanical microcantilevers," *Nanotechnology*, vol. 18, no. 44, p. 445502, 2007.

[17] T. Braun, V. Barwich, M. K. Ghatkesar, A. H. Bredekamp, C. Gerber, M. Hegner, and H. P. Lang, "Micromechanical mass sensors for biomolecular detection in a physiological environment," *Physical Review E*, vol. 72, no. 3, p. 031907, 2005.

[18] K. Ekinci and M. Roukes, "Nanoelectromechanical systems," *Review of scientific instruments*, vol. 76, no. 6, p. 061101, 2005.

[19] S. Schmid, L. G. Villanueva, and M. L. Roukes, *Fundamentals of nanomechanical resonators*. Springer, 2016, vol. 49.

[20] M. K. Ghatkesar, T. Braun, V. Barwich, J.-P. Ramseyer, C. Gerber, M. Hegner, and H. P. Lang, "Resonating modes of vibrating microcantilevers in liquid," *Applied Physics Letters*, vol. 92, no. 4, p. 043106, 2008.

[21] J. E. Sader, "Frequency response of cantilever beams immersed in viscous fluids with applications to the atomic force microscope," *Journal of applied physics*, vol. 84, no. 1, pp. 64–76, 1998.

[22] Z. Hao, A. Erbil, and F. Ayazi, "An analytical model for support loss in micromachined beam resonators with in-plane flexural vibrations," *Sensors and Actuators A: Physical*, vol. 109, no. 1-2, pp. 156–164, 2003.

[23] J. E. Sader, T. P. Burg, and S. R. Manalis, "Energy dissipation in microfluidic beam resonators," 2010.

[24] S. Olcum, N. Cermak, S. C. Wasserman, K. S. Christine, H. Atsumi, K. R. Payer, W. Shen, J. Lee, A. M. Belcher, S. N. Bhatia *et al.*, "Weighing nanoparticles in solution at the attogram scale," *Proceedings of the National Academy of Sciences*, vol. 111, no. 4, pp. 1310–1315, 2014.

[25] M. Gagino, G. Katsikis, S. Olcum, L. Virot, M. Cochet, A. Thuaire, S. R. Manalis, and V. Agache, "Suspended nanochannel resonator arrays with piezoresistive sensors for high-throughput weighing of nanoparticles in solution," *ACS sensors*, vol. 5, no. 4, pp. 1230–1238, 2020.

[26] V. Agache, G. Blanco-Gomez, M. Cochet, and P. Caillat, "Suspended nanochannel in mems plate resonator for mass sensing in liquid," in *2011 IEEE 24th International Conference on Micro Electro Mechanical Systems*. IEEE, 2011, pp. 157–160.

[27] P. Belardinelli, M. Ghatkesar, U. Staufer, and F. Alijani, "Linear and non-linear vibrations of fluid-filled hollow microcantilevers interacting with small particles," *International Journal of Non-Linear Mechanics*, vol. 93, pp. 30–40, 2017.

[28] S. Olcum, N. Cermak, S. C. Wasserman, and S. R. Manalis, "High-speed multiple-mode mass-sensing resolves dynamic nanoscale mass distributions," *Nature communications*, vol. 6, no. 1, pp. 1–8, 2015.

[29] A. Demir, "Understanding fundamental tradeoffs in nanomechanical resonant sensors," *arXiv preprint arXiv:2010.04447*, 2020.

[30] S. L. Percival, R. Chalmers, M. Embrey, P. R. Hunter, J. Sellwood, P. Wyn-Jones *et al.*, *Microbiology of waterborne diseases*. Elsevier, 2014.

[31] A. H. Havelaar, M. D. Kirk, P. R. Torgerson, H. J. Gibb, T. Hald, R. J. Lake, N. Praet, D. C. Bellinger, N. R. De Silva, N. Gargouri *et al.*, "World health organization global estimates and regional comparisons of the burden of foodborne disease in 2010," *PLoS medicine*, vol. 12, no. 12, p. e1001923, 2015.

[32] W. E. Stamm and S. R. Norrby, "Urinary tract infections: disease panorama and challenges," *The Journal of infectious diseases*, vol. 183, no. Supplement_1, pp. S1–S4, 2001.

[33] L. Zhang and B. Foxman, "Molecular epidemiology of escherichia coli mediated urinary tract infections," *Front Biosci*, vol. 8, pp. e235–e244, 2003.

[34] C. M. Garrett, Reginald H.; Grisham, *Biochemistry*. Cengage Learning, 2017.

[35] R. Phillips, J. Kondev, J. Theriot, and H. Garcia, *Physical biology of the cell*. Garland Science, 2012.

[36] W. H. Grover, A. K. Bryan, M. Diez-Silva, S. Suresh, J. M. Higgins, and S. R. Manalis, "Measuring single-cell density," *Proceedings of the National Academy of Sciences*, vol. 108, no. 27, pp. 10 992–10 996, 2011.

[37] C. L. Lewis, C. C. Craig, and A. G. Senecal, "Mass and density measurements of live and dead gram-negative and gram-positive bacterial populations," *Applied and environmental microbiology*, vol. 80, no. 12, pp. 3622–3631, 2014.

[38] M. Godin, A. K. Bryan, T. P. Burg, K. Babcock, and S. R. Manalis, "Measuring the mass, density, and size of particles and cells using a suspended microchannel resonator," *Applied physics letters*, vol. 91, no. 12, p. 123121, 2007.

[39] T. P. Burg, M. Godin, S. M. Knudsen, W. Shen, G. Carlson, J. S. Foster, K. Babcock, and S. R. Manalis, "Weighing of biomolecules, single cells and single nanoparticles in fluid," *nature*, vol. 446, no. 7139, pp. 1066–1069, 2007.

[40] M. Godin, F. F. Delgado, S. Son, W. H. Grover, A. K. Bryan, A. Tzur, P. Jorgensen, K. Payer, A. D. Grossman, M. W. Kirschner *et al.*, "Using buoyant mass to measure the growth of single cells," *Nature methods*, vol. 7, no. 5, pp. 387–390, 2010.

[41] G. Tomaiuolo, "Biomechanical properties of red blood cells in health and disease towards microfluidics," *Biomicrofluidics*, vol. 8, no. 5, p. 051501, 2014.

[42] M. N. Starodubtseva, "Mechanical properties of cells and ageing," *Ageing research reviews*, vol. 10, no. 1, pp. 16–25, 2011.

[43] J. Arlett, E. Myers, and M. Roukes, "Comparative advantages of mechanical biosensors," *Nature nanotechnology*, vol. 6, no. 4, pp. 203–215, 2011.

[44] A. K. Bryan, V. C. Hecht, W. Shen, K. Payer, W. H. Grover, and S. R. Manalis, "Measuring single cell mass, volume, and density with dual suspended microchannel resonators," *Lab on a Chip*, vol. 14, no. 3, pp. 569–576, 2014.

[45] Y. Weng, F. F. Delgado, S. Son, T. P. Burg, S. C. Wasserman, and S. R. Manalis, "Mass sensors with mechanical traps for weighing single cells in different fluids," *Lab on a Chip*, vol. 11, no. 24, pp. 4174–4180, 2011.

[46] J. H. Kang, T. P. Miettinen, L. Chen, S. Olcum, G. Katsikis, P. S. Doyle, and S. R. Manalis, "Noninvasive monitoring of single-cell mechanics by acoustic scattering," *Nature methods*, vol. 16, no. 3, pp. 263–269, 2019.

[47] O. Otto, P. Rosendahl, A. Mietke, S. Golfier, C. Herold, D. Klaue, S. Girardo, S. Pagliara, A. Ekpenyong, A. Jacobi *et al.*, "Real-time deformability cytometry: on-the-fly cell mechanical phenotyping," *Nature methods*, vol. 12, no. 3, pp. 199–202, 2015.

[48] A. Mietke, O. Otto, S. Girardo, P. Rosendahl, A. Taubenberger, S. Golfier, E. Ulbricht, S. Aland, J. Guck, and E. Fischer-Friedrich, "Extracting cell stiffness from real-time deformability cytometry: theory and experiment," *Biophysical Journal*, vol. 109, no. 10, pp. 2023–2036, 2015.

[49] B. Ziaie, A. Baldi, and M. Z. Atashbar, "Introduction to micro-/nanofabrication," in *Springer handbook of nanotechnology*. Springer, 2010, pp. 231–269.

[50] T. Xu, M. Bachman, F.-G. Zeng, and G.-P. Li, "Polymeric microcantilever array for auditory front-end processing," *Sensors and Actuators A: Physical*, vol. 114, no. 2-3, pp. 176–182, 2004.

[51] S. Mouaziz, G. Boero, R. S. Popovic, and J. Brugger, "Polymer-based cantilevers with integrated electrodes," *Journal of microelectromechanical systems*, vol. 15, no. 4, pp. 890–895, 2006.

[52] A. W. McFarland, M. A. Poggi, L. A. Bottomley, and J. S. Colton, "Injection moulding of high aspect ratio micron-scale thickness polymeric microcantilevers," *Nanotechnology*, vol. 15, no. 11, p. 1628, 2004.

[53] P. Urwyler, H. Schift, J. Gobrecht, O. Häfeli, M. Altana, F. Battiston, and B. Müller, "Surface patterned polymer micro-cantilever arrays for sensing," *Sensors and Actuators A: Physical*, vol. 172, no. 1, pp. 2–8, 2011.

[54] S. Schmid, *Electrostatically actuated all-polymer microbeam resonators: Characterization and application*. ETH Zurich, 2009, vol. 6.

[55] C. Liao, A. Wuethrich, and M. Trau, "A material odyssey for 3d nano/microstructures: two photon polymerization based nanolithography in bioapplications," *Applied Materials Today*, vol. 19, p. 100635, 2020.

[56] C. N. LaFratta and T. Baldacchini, "Two-photon polymerization metrology: Characterization methods of mechanisms and microstructures," *Micromachines*, vol. 8, no. 4, p. 101, 2017.

[57] Z. Gan, Y. Cao, R. A. Evans, and M. Gu, "Three-dimensional deep sub-diffraction optical beam lithography with 9 nm feature size," *Nature communications*, vol. 4, no. 1, pp. 1–7, 2013.

[58] M. Emons, K. Obata, T. Binhammer, A. Ovsianikov, B. N. Chichkov, and U. Morgner, "Two-photon polymerization technique with sub-50 nm resolution by sub-10 fs laser pulses," *Optical Materials Express*, vol. 2, no. 7, pp. 942–947, 2012.

[59] I. S. Ladner, M. A. Cullinan, and S. K. Saha, "Tensile properties of polymer nanowires fabricated via two-photon lithography," *RSC Advances*, vol. 9, no. 49, pp. 28 808–28 813, 2019.

[60] E. D. Lemma, F. Rizzi, T. Dattoma, B. Spagnolo, L. Sileo, A. Qualtieri, M. De Vittorio, and F. Pisanello, "Mechanical properties tunability of three-dimensional polymeric structures in two-photon lithography," *IEEE transactions on nanotechnology*, vol. 16, no. 1, pp. 23–31, 2016.

[61] C. Accoto, A. Qualtieri, F. Pisanello, C. Ricciardi, C. F. Pirri, M. De Vittorio, and F. Rizzi, "Two-photon polymerization lithography and laser doppler vibrometry of a su-8-based suspended microchannel resonator," *Journal of Microelectromechanical Systems*, vol. 24, no. 4, pp. 1038–1042, 2014.

[62] G. Genolet, J. Brugger, M. Despont, U. Drechsler, P. Vettiger, N. De Rooij, and D. Anselmetti, "Soft, entirely photoplastic probes for scanning force microscopy," *Review of scientific instruments*, vol. 70, no. 5, pp. 2398–2401, 1999.

[63] S. Schmid and C. Hierold, "Damping mechanisms of single-clamped and prestressed double-clamped resonant polymer microbeams," *Journal of Applied Physics*, vol. 104, no. 9, p. 093516, 2008.

[64] S. Schmid, P. Wägli, and C. Hierold, "All-polymer microstring resonant humidity sensor with enhanced sensitivity due to change of intrinsic stress," *Micro and Nanosystems*, 2008.

[65] A. W. McFarland, M. A. Poggi, L. A. Bottomley, and J. S. Colton, "Production and characterization of polymer microcantilevers," *Review of scientific instruments*, vol. 75, no. 8, pp. 2756–2758, 2004.

[66] M. Calleja, M. Nordström, M. Álvarez, J. Tamayo, L. M. Lechuga, and A. Boisen, "Highly sensitive polymer-based cantilever-sensors for dna detection," *Ultramicroscopy*, vol. 105, no. 1-4, pp. 215–222, 2005.
[67] G. Zhang, V. Chu, and J. P. Conde, "Conductive blended polymer mems microresonators," *Journal of microelectromechanical systems*, vol. 16, no. 2, pp. 329–335, 2007.
[68] G. K. Fedder, C. Hierold, J. G. Korvink, and O. Tabata, *Resonant MEMS: fundamentals, implementation, and application*. John Wiley & Sons, 2015, vol. 22.

# Part II

# Paper
# Toward 3D printed suspended microchannel resonators

# Toward 3D printed suspended microchannel resonators

Jikke de Winter

*Abstract*—**Biosensing properties like mass, density and stiffness on a single cell level can help diagnose diseases. Mass sensing of cells and subcellular components is typically performed with resonant microstructures. Recently such microstructures were fabricated using an emerging 3D printing technique called two-photon polymerization (2PP) contrary to conventional lithography-based fabrication. The suspended microchannel resonator (SMR) is such a resonant microstructure with an embedded fluidic channel for buoyant mass sensing, which has not yet been fabricated using 2PP. This work aims to 3D print an SMR with a sufficient mass resolution to detect the buoyant mass of E. Coli bacteria ($175\ fg$ in water). It was realized by first characterizing the damping in 3D printed polymer microbeam resonators for a better understanding of dominating damping sources. Followed by maximizing their quality factor and fabricating a prototype 3D printed SMR. The characterized devices set a record-breaking standard for damping of polymer microbeam resonators: Cantilevers and bridges approached quality factors of 1000 and tensile stressed narrow bridges achieved a quality factor of 1819. These polymer resonators were dominated by bulk friction damping, but still had a mass resolution advantage over similar silicon-based devices when working in lower quality factor ($Q < 1000$) conditions, due to the low mass density of the polymer. Subsequently, prototypes of the suspended microchannel resonator were fabricated with multi-scale 3D printing containing a plug-and-play connection to fluidics and measurement equipment. Their theoretical mass resolution was estimated to be $\leq\ 60\ fg$, which is sensitive enough to detect E. Coli bacteria and compete with conventional fabricated SMRs. This paves the path towards actual biosensing 3D printed SMRs with the capabilities of lithography-based fabricated devices but with additional design and fabrication flexibility.**

*Index Terms*—**Suspended microchannel resonator, 3D printing, Two-photon polymerization, Polymer microbeam resonator, Damping, Quality factor, Mass sensing, Mass resolution and E. Coli bacteria.**

## I. Introduction

Mechanical biosensing can be of great benefit to the fields of biology and medicine. Research has shown that mechanical properties like mass and stiffness of cells can be linked to a variety of diseases [1]–[5]. For example, blood cells can be distinguished from circulating tumor cells based on their deformability and mass [6]. This label-free method could help with diagnosing diseases such as cancer or bacterial and viral infections. Mechanical analysis of biological material on a single (sub)cellular level has a big potential, but device fabrication could still be improved. Conventional device fabrication techniques involve complex lithography steps, which can be time-consuming, expensive and impose design constraints [7].

Microelectromechanical systems (MEMS) can be used to measure parameters such as mass and stiffness on a microscale size. These systems often use electrical transducers combined with mechanical moving parts. Mass sensing with MEMS and NEMS (nanoelectromechanical systems) has reached spectacular resolutions down to the boundary of single atoms [8]. Mass sensing of cells and subcellular components is commonly performed with resonant beams. A special case is a beam with an embedded microfluidic channel, the suspended microchannel resonator (SMR). This yields the advantages of higher throughput of analytes and the possibility to operate in a vacuum. Higher quality factors are achieved by decreasing the viscous drag of liquids or gasses by operating the devices in a vacuum, this is key in achieving a better mass resolution [9]. Decreasing beam mass can be another key factor in achieving a better mass resolution. Despite the significant friction damping of polymer microstructures, their lower mass density could compensate for the loss and still achieve a good mass resolution.

Typically SMRs are fabricated out of silicon-based materials using semiconductor-like manufacturing processes, which can be complex, expensive and require high-grade cleanroom facilities. These processes also limit geometrical freedom, material choice and prototyping speed. Recently 3D printed microbeam resonators were fabricated using two-photon polymerization (2PP) [10] [11]. This fabrication technique yields rapid prototyping speed, 3D design space and can be utilized outside of high-grade cleanroom facilities. Polymer microbeam resonators with more geometrical freedom can be fabricated using this technique, opening up new possibilities for improvements. Polymers also have distinct mechanical properties compared to the typically used silicon-based materials, leading to reduced device mass but also increased intrinsic damping of the resonators. The latter can result in a lower measurement sensitivity but can be mitigated by adjustment of resonant frequency and inducing tensile stress in the beam [12]. A key advantage to the work of Kramer et al was that fabrication by multi-scale 3D printing enabled rapid prototyping, easy connection to macrofluidics and measurement equipment [11]. Making end-to-end fabrication flexible, accessible and without manual procedures.

Polymer microbeam resonators are not a recent development, but the applications are generally limited to the field of research [13], [14]. They were developed for applications such as scanning probe microscopy, chemical sensing, biological sensing, humidity sensing and cellular handling [11], [12], [15]. Performance of the state of the art in polymer microbeam resonators will be reviewed based on their frequency and quality factor, as displayed in Figure 1 [10], [11], [13], [14], [16]–[24]. Operating conditions and beam type will also be indicated additionally.

The goal of this work was to find the smallest mass resolution for a 3D printed suspended microchannel resonator

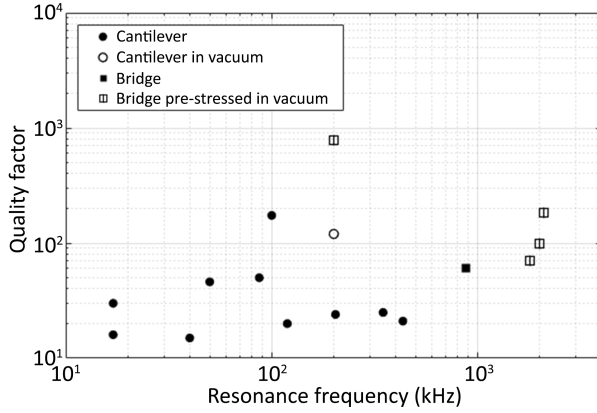


Fig. 1: Polymer microbeam resonators state of the art [10], [11], [13], [14], [16]–[24]

designed for mass sensing of E.Coli bacteria. Multi-scale 3D printing was utilized to ensure easy connection to fluidics and measurement equipment. This research was focused on understanding the fundamentals of damping in 3D printed polymer microbeam resonators, improving their quality factor and therefore their mass resolution. The theoretical dependency of variables were identified to be able to single out damping sources and improve quality factors experimentally. Improvement of the signal-to-noise ratio in the measurement of the vibrations lies beyond the scope of this work. The theoretical background for the performance of mass sensing microbeam resonators will be discussed below, including the fundamentals of damping phenomena applicable to polymer microbeam resonators. Materials and methods of device fabrication and characterization and performance improvement experiments will be described in section II. Section III will show the obtained results of fabrication, experimental device characterization and attempted performance improvements. Section IV will present a discussion about those observations and their implications in relation to literature and the state of the art. Concluding remarks will be stated in section V. Followed by the outlook for 3D printed suspended microchannel resonators in section VI.

## II. Damping theory

The theoretical resonance frequency of a beam is defined in equation 1 [25]. Frequency is denoted as $f$ with subscript $_R$ for resonant and $n$ for resonant mode number. Beam stiffness is depicted as $k$, beam mass $m$, Young's modulus $Y$, beam moment of inertia $I$ and beam length $l$. Constant $a_n$ can be calculated with equation 2 for single-clamped beams (cantilevers) and double-clamped beams (bridges) [25], [26].

$$f_{R,n} = \frac{a_n^2}{2\pi}\sqrt{\frac{k}{m}} = \frac{a_n^2}{2\pi}\sqrt{\frac{YI}{ml^3}} \tag{1}$$

$$a_n = \begin{cases} 1.875, 4.694, 7.854, 11.0, (n-0.5)\pi & Cantilever \\ 4.7300, 7.8532, 10, 9956, (n+0.5)\pi & Bridge \end{cases} \tag{2}$$

Mass resolution is a performance indicator for resonant mass sensors, indicating the minimal observable mass. The mass resolution $\delta m$ can be calculated with equation 3 adapted from [4]. It does not only depend on resonance frequency and effective mass $m_{eff}$, but also on the quality factor $Q$ and the signal-to-noise ratio ($SNR$). The fluctuation of the observed resonance frequency is denoted with $\delta f$ and the mass responsivity by $\Re$. Effective mass $m_{eff}$ can be calculated with $m_{eff} \approx 0.25m$ for cantilevers and $m_{eff} \approx 0.39m$ for bridges at their fundamental mode [27].

$$\delta m \approx \frac{\delta f}{\Re} = -2m_{eff}\frac{\delta f}{f_{R,n}} \approx -2m_{eff}\frac{1}{Q}\frac{1}{SNR} \tag{3}$$

The quality factor of a resonator is defined in equation 4 as the ratio between stored energy $E$ and lost energy $\Delta E$ for a single resonant cycle [28]. The loss of energy is caused by energy dissipation due to damping.

$$Q = 2\pi\frac{E}{\Delta E} \tag{4}$$

Four main sources of damping can be identified for polymer microbeam resonators: Medium interaction damping, clamping damping, friction damping and thermoelastic damping (TED) [22]. The quality factor of such a resonator can be calculated with equation 5 [28].

$$Q = \left(\frac{1}{Q_{medium}} + \frac{1}{Q_{clamping}} + \frac{1}{Q_{friction}} + \frac{1}{Q_{TED}}\right)^{-1} \tag{5}$$

Medium interaction damping are losses caused by gaseous or fluidic media interacting with the vibrating beam. Clamping damping is caused by energy dissipation at the connection between the beam and the substrate. Intrinsic damping types are caused by energy losses inside the beam material. Those losses are dependent on material properties, fabrication processes and temperature. The following loss mechanisms are defined as intrinsic damping: Friction losses, thermoelastic damping and phonon-phonon interaction losses. The latter is an atomic interaction with the strain field, which only occurs in crystalline materials. Friction damping is caused by molecular motions in the polymer and thermoelastic damping is caused by strain leading to a thermal gradient across the beam. Other damping sources caused by electrostatic charges and magnetic fields were neglected because they are more effecting resonators using magnetic actuation and electric sensing.

### *Medium interaction damping*

Medium interaction damping can be subdivided into damping by liquid or gas. Damping by surrounding liquid typically results in very small quality factors for microcantilevers and microbridges. This arises from viscous loading of the beam by the fluid. Quality factors close to unity have been reported at the fundamental resonant mode of microcantilevers, but increasing mode number yields better quality factors up to 30 [29], [30]. A theoretical model for damping by the liquid inside the resonator was introduced to determine the quality factor of suspended microchannel resonators, see equation 8 [31]. The following variables had been used to be able to calculate this

quality factor denoted by $Q_{liquidinside}$: 'Normalized quality factor' $F_Q$ approximated in equation 7, Reynolds number $\beta$ and calculated in equation 6, the dynamic viscosity denoted with $\mu$, $h$ the thickness of the beam, the beam width $w$ and $l$ length of the beam. Subscript $_c$ denoted the internal channel and $liq$ the liquid environment.

$$\beta = \frac{2\pi\rho_{liq} f_{R,1} h_c^2}{\mu_{liq}} \tag{6}$$

$$F_Q \approx \frac{38.73}{\beta} + 0.1521\sqrt{\beta} \tag{7}$$

$$Q_{liquidinside} = F_Q \left(\frac{\rho}{\rho_{liq}}\right)\left(\frac{h}{h_c}\right)\left(\frac{w}{w_c}\right)\left(\frac{l}{h_c}\right)^2 \tag{8}$$

Gas damping is dependent on the geometry of the microstructure, vibrational frequency, gas type and gas pressure. A ballistic and a fluidic regime can be depending on the pressure range of the gas interacting with the vibrating beam. In the fluidic regime, the gas can be modeled as a continuous fluid and in the ballistic regime it can be modeled as an exchange of kinetic energy between the gas molecules and the beam. Quality factors can increase orders of magnitude by moving from the fluidic regime to the ballistic regime, as depicted by Schmid et al. in [28]. Pressure dependency of the quality factor is linear until an intrinsic limit is reached inside the ballistic regime. The vacuum allows the resonator to be operated at this limit, yielding minimal gas damping. The remaining gas damping can be divided into 2 models: Squeeze-film damping and drag-force damping, which are only valid for the ballistic regime. Ballistic squeeze-film damping $Q_{bsf}$ and ballistic drag-force damping $Q_{bdf}$ can be calculated using equations 9 and 10 respectively [28] [32]. Where mass density is denoted by $\rho$, $d_0$ distance from the beam to the substrate, $L_p$ peripheral length of the beam, $p$ gas pressure, $R_{gas}$ universal gas constant, $T$ temperature in Kelvin and $M_m$ the molar mass of the gas.

$$Q_{bsf} = (2\pi)^{\frac{5}{2}} \frac{\rho h f_{R,n} d_0}{p L_p} \sqrt{\frac{R_{gas} T}{M_m}} \tag{9}$$

$$Q_{bdf} = \frac{\rho h f_{R,n}}{p} \sqrt{\frac{\pi^3}{8}} \sqrt{\frac{R_{gas} T}{M_m}} \tag{10}$$

*Clamping damping*

Clamping damping is defined as a transfer of vibrational kinetic energy from the beam to the supporting substrate, this is highly dependent on the geometry of the beam and the substrate. Two equations can be used to approximate the quality factor due to clamping damping of a cantilever resonating at the fundamental mode $Q_{clampsc}$, see equation 11 [28]. Subscript $sub$ stands for substrate and $\lambda$ is the wavelength. The clamping damping of a double-clamped bridge resonator $Q_{clampdc}$ can be calculated with equation 12 [33]. The factor in front of the brackets is only valid for the fundamental mode and varies per resonant mode. It should be noted that clamping losses increase with mode number. Generally clamping losses can be reduced by increasing the slenderness of the cantilever and increasing the thickness of the supporting substrate.

$$Q_{clampsc} \approx \begin{cases} 1.05 \frac{l}{w} \frac{h_{sub}^2}{h^2}, & h_{sub} \leq \lambda \\ 3.2 \frac{l}{w} \left(\frac{l}{h}\right)^4, & h_{sub} > \lambda \end{cases} \tag{11}$$

$$Q_{clampdc} \approx 0.638 \left(\frac{l}{h}\right)^3 \tag{12}$$

*Friction damping*

Surface friction is a loss phenomenon caused by imperfections and roughness of the beam's top and bottom surfaces. This damping phenomenon can become dominant when the beam's surface-to-volume ratio is high, this typically occurs when the beam's thickness is on the nanometer scale [28]. Bulk friction losses arise from atomic or molecular motions which are not reversible and were regarded as friction damping for this work. The effect of this loss mechanism depends on a material's relaxation rate $\bar{\tau}$ in relation to the excitation frequency. Significant damping occurs when the frequency and the relaxation rate are in the same order of magnitude. The relaxation rate at constant strain $\tau_\epsilon$ and constant stress $\tau_\sigma$ can be calculated with equation 13 and 14. The geometrical average of the relaxation rate can be calculated by $\bar{\tau} = \sqrt{\tau_\epsilon \tau_\sigma}$. The unrelaxed Young's modulus caused by stress $Y_u$ and the relaxed Young's modulus $Y_r$ is related as $Y_u = Y_r + \Delta Y$. Finally, $\eta$ is the loss coefficient of the beam material. The resulting quality factor for friction damping can be calculated with equation 15 [28].

$$\tau_\epsilon = \frac{\eta}{\Delta Y} \tag{13}$$

$$\tau_\sigma = \tau_\epsilon \frac{Y_r + \Delta Y}{Y_r} \tag{14}$$

$$Q_{friction}^{-1} = \left(\frac{\Delta Y}{\sqrt{Y_r Y_u}}\right) \frac{2\pi f \bar{\tau}}{1 + (2\pi f)^2 \bar{\tau}^2} \tag{15}$$

*Thermoelastic damping*

Thermoelastic damping is a loss mechanism that is caused by local strain inside the beam material, resulting in local temperature differences. Energy dissipation occurs because of the localized heat flow creating entropy. The relaxation time of thermoelastic damping can be calculated using equation 16 and the quality factor can be calculated using equation 17 [28]. The material properties are denoted with the following variables: Specific heat capacity $c_p$, thermal conductivity $\kappa$ and thermal expansion coefficient $\alpha$.

$$\tau_{TED} = \frac{h^2 \rho c_p}{\pi^2 \kappa} \tag{16}$$

$$Q_{TED}^{-1} = \left(\frac{Y \alpha^2 T}{\rho c_p}\right) \frac{2\pi f \tau_{TED}}{1 + (2\pi f)^2 \tau_{TED}^2} \tag{17}$$

## III. Materials and methods

Three kinds of devices were fabricated with different experimental goals: Pillars for material characterization, solid resonant beams on different substrate materials for the determination of damping sources and hollow resonant beams on fluidic interfaces for fluid tests and prototyping purposes.

*Resonant beam fabrication*

Solid and hollow resonators shaped like cantilevers and bridges were fabricated using two-photon polymerization (2PP) 3D printing with the Professional GT (Nanoscribe GmbH & Co. KG, Germany). See appendix A for the step-by-step fabrication protocol. The structures were printed in Dip-in Laser Lithography configuration using 25x NA 0.8 lens (Carl Zeiss AG, Germany) in galvo mode at 100% (50 $mW$) laser power and 100 $mm/s$ scanspeed using IP-S resin (Nanoscribe GmbH & Co. KG, Germany). IP-S was selected for its superior Young's modulus and other mechanical properties. Table I displays the dimensions of the different structure types. Solid beams were suspended by rectangular pillars and SMRs by domes. The domes provided a microfluidic connection between the fluidic interface (substrate) and the hollow bridge. Each fluidic interface contained a single hollow bridge. Solid Cantilevers and bridges were printed on the same substrate, but only with varying beam lengths (with steps of 50 $\mu m$) to avoid the crosstalk between different devices due to mechanical coupling through the substrate. Three types of beams had distinguished printing methods: Thick and hollow beams were printed using block splitting in the longitudinal direction with blocks of 4 $\mu m$ and 2 $\mu m$ overlap. Thin beams were printed without block splitting.

TABLE I: Dimensions of 3D printed structures

| Structure type | Length ($\mu m$) | Width ($\mu m$) | Thickness ($\mu m$) |
|---|---|---|---|
| Thin cantilever | 50-100 | 17.5 | 5 |
| Thin bridge | 100-300 | 17.5 | 5 |
| Thin narrowed bridge | 100-300 | 17.5 (base)<br>6 (center) | 5 |
| Thick cantilever | 50-300 | 17.5 | 14 |
| Thick bridge | 150-300 | 17.5 | 14 |
| Pillar supporting solid beams | 35 | 17.5 | 25 |
| Hollow bridge (SMR) | 119 | 12 (external)<br>10 (internal) | 16 (external)<br>10 (internal) |
| Dome supporting hollow bridge | 395 | 395 | 85 |

The following development procedure was used for the printed structures: 25 minutes of submersion in $\geq$ 99.5% Propylene glycol monomethyl ether acetate (MilliporeSigma, United States) followed by 30 seconds of submersion in Methoxy-nonafluorobutane known as Novec 7100 engineering fluid (MilliporeSigma, United States). Hollow beams were flushed additionally with Novec using a manual syringe.

The structures were 3D printed on top of 4 different substrates described in Table II: Standard in this work is diced Silicon wafer pieces with $\{100\}$ orientation. SiC-6H wafer dices and polymerized 3DM TOUGH clear (an acrylate-methacrylate 3D printing resin by ADMAT SASU, France) were used for substrate comparison experiments. Hollow beams were printed on top of a fluidic interface made of polymerized 3DM TOUGH clear. All polymerized 3DM TOUGH clear substrates were sputtercoated using the JFC-1300 Sputtercoater (JEOL Ltd., Japan) with approximately 2 $nm$ of gold for increased reflectivity necessary for device fabrication.

TABLE II: Dimensions of different substrates

| Substrate | Length ($mm$) | Width ($mm$) | Thickness ($mm$) |
|---|---|---|---|
| Silicon $\{100\}$ wafer dices | 25 | 25 | 0.700 |
| SiC-6H wafer dices | 10 | 10 | 0.200 |
| 3DM TOUGH clear flat | 25 | 25 | 2.9 |
| 3DM TOUGH clear fluidic interface | 8.2 | 4.0 | 3.7 |

*Pillar fabrication*

The Young's modulus of pillars was determined using FT-NMT03 Nanomechanical Testing System (FemtoTools AG, Switzerland). Square pillars were designed to match the tip shape, dimensions and stay within the force-displacement limits of the measurement system. Fields of 25 pillars (each 50 $\mu m$ by 50 $\mu m$ and 100 $\mu m$ height) were fabricated in the same manner as mentioned before but had an extra treatment post-development with the purpose of studying the effects of the treatments on the material properties. The following post-development treatments were used: Thermal treatment with the UN30 oven (Memmert GmbH + Co. KG, Germany) and ultraviolet light exposure for 40 minutes ranging from 320 to 550 $nm$ in the PHOTOPOL light (Dentalfarm SRL, Italy). The thermal treatments were performed at different temperatures (120, 200, 240, and 280°C) and duration (15 and 45 minutes) without preheating the oven. A combined treatment was also used, consisting of ultraviolet light exposure followed by thermal treatment at 200°C for 15 minutes.

*Fluidic interface fabrication*

The fluidic interface was used for creating an easy connection between macrofluidic tubes and the microfluidic channels of the resonator, embedded in the fabrication process without adding manual steps. This is shown in the step-by-step fabrication protocol in appendix A. The fluidic interface consisted of a flat surface with two microfluidic holes of about 200 $\mu m$ in diameter channeling to macrofluidic tube connections. A specially designed 2PP adapter with 8 fluidic interfaces was 3D printed using the Micro Plus Hi-Res (EnvisionTEC US LLC, United States). The 3D printing was performed with Digital Light Processing (DLP) (at a wavelength of approximately 385 $nm$) for 3.5 seconds per layer of 35$\mu m$ thick using 3DM TOUGH clear resin. 3DM TOUGH clear resin was used for its improved adhesion strength contrary to earlier work [11] where HTM-140v2 was used, see appendix E for the adhesion strength experiment. The unpolymerized resin was removed with 2 times 5 minutes submersion in $\geq$ 99.8% 2-Propanol (Honeywell International Inc, United States) combined with ultrasonic cleaning using the Sonorex Super RK31 (BANDELIN electronic GmbH & Co. KG, Germany) followed by a single ultraviolet light exposure for 6 minutes ranging from 320 to 550 $nm$ in the PHOTOPOL light (Dentalfarm SRL, Italy).

*Young's modulus quantification*

The Young's modulus of pillars was determined using FT-NMT03 Nanomechanical Testing System (FemtoTools AG, Switzerland) with non-destructive compression experiments.

Silicon flat punch tip type FT-S200000 (FemtoTools AG, Switzerland) was used to compress the pillars vertically with a speed of 0.104 $\mu m/s$ up to a maximal force of 80000 $\mu N$, see appendix B for visualization. The reference stiffness was measured on the surface of the substrate to compensate for the stiffness of the measurement chain. The pillar dimensions were measured afterward using the 6010LA Scanning Electron Microscope (JEOL Ltd., Japan).

*Resonator characterization*

The resonant frequencies and corresponding quality factors of the solid beams were determined with the MSA-400-PM2-D Laser Doppler vibrometer (Polytec GmbH, Germany) equipped with the MSA-A-M20X lens. The samples were sputtercoated using the JFC-1300 Sputtercoater with approximately 72 $nm$ of gold prior to the measurements, to increase the reflectivity of the devices. Post-development thermal treatments of devices were performed at 200°C for 15 minutes, before sputter coating gold and within the same day of characterization. Single-point and multi-point measurements were used to find the velocity peaks at the resonant frequencies and their mode shape. The samples were mounted on top of a piezoelectric actuator with a resonance frequency of approximately $4MHz$ made of PIC255 (PI Ceramic GmbH, Germany) using double-sided carbon tape inside a homemade vacuum chamber. Measurements were performed at room temperature (20°C) and high vacuum pressure ($\leq 5 * 10^{-5}$ $mbar$). The actuating signal used was Pseudo-random with an amplitude of 10 $V$ ranging from 1 $Hz$ to 2 $MHz$.

## IV. Results

*3D printed microbeam resonators*

Polymer solid microbeam resonators were 3D printed using two-photon polymerization (2PP) with IP-S resin. Solid devices were fabricated first to analyze the effects of damping sources on a fundamental level. Beam lengths were varied to be able to characterize the devices at frequencies between 50 $kHz$ and 1500 $kHz$. The cantilevers and bridges were fabricated on the same substrate, but only with varying beam lengths to avoid the crosstalk between different devices due to mechanical coupling through the substrate. Two different types of microbeam were fabricated; thick type beams with a thickness of 14 $\mu m$ and thin type beams 5 $\mu m$. See Figure 2 for thick type resonators. Length of thick type cantilevers was ranging from 50 $\mu m$ to 300 $\mu m$ with steps of 50 $\mu m$ and from 150 $\mu m$ to 300 $\mu m$ for bridges with equal steps.

See Figure 3 for the thin type cantilever and bridge successfully fabricated as 50 $\mu m$ and 100 $\mu m$ long cantilevers and bridges from 150 $\mu m$ to 300 $\mu m$ with steps of 50 $\mu m$. Large deformations and stiction were observed for cantilevers from 150 $\mu m$ and longer, due to the surface tension of the evaporating development liquid (Novec).

Special thin type bridges were fabricated with a tapered width in the center to locally reduce the cross-sectional area. The narrowed bridge is shown in Figure 4, of which the width was narrowed down from 17.5 $\mu m$ at the supports to 6 $\mu m$ in the middle section. These bridges were fabricated with lengths varying from 100 $\mu m$ to 300 $\mu m$ (with steps of 50 $\mu m$) in order to characterize them at varying frequencies.

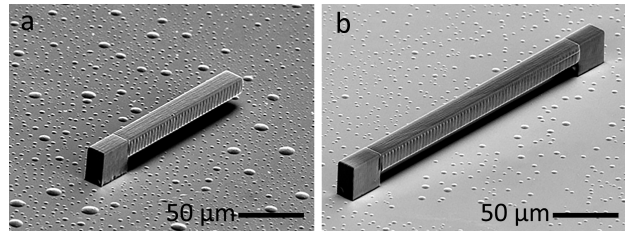


Fig. 2: Thick type microbeams consisting of IP-S on Silicon substrates. (a) Cantilever 150 $\mu m$ long, 17.5 $\mu m$ wide and 14 $\mu m$ thick. (b) Bridge 250 $\mu m$ long, 17.5 $\mu m$ wide and 14 $\mu m$ thick.

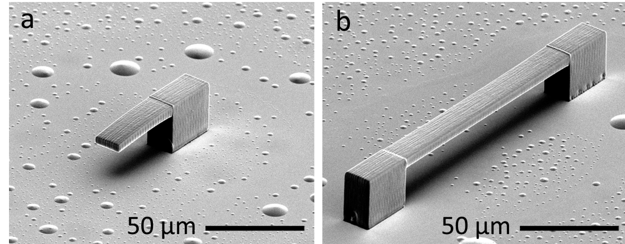


Fig. 3: Thin type microbeams consisting of IP-S on Silicon substrates. (a) Cantilever 50 $\mu m$ long, 17.5 $\mu m$ wide and 5 $\mu m$ thick. (b) Bridge 150 $\mu m$ long, 17.5 $\mu m$ wide and 5 $\mu m$ thick.

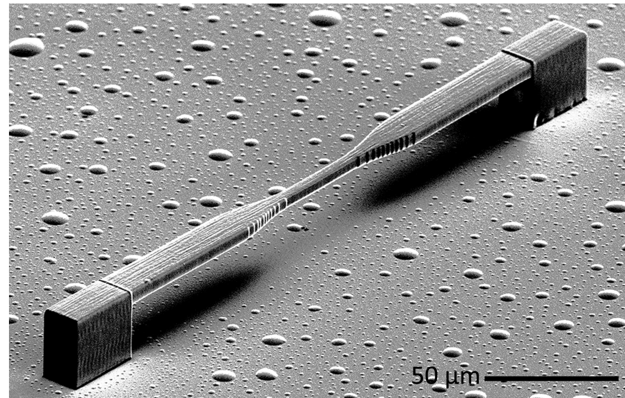


Fig. 4: Thin type narrowed bridge consisting of IP-S on Silicon substrate. The bridge is 250 $\mu m$ long, 17.5 $\mu m$ wide at the base, 6 wide $\mu m$ at its center and 5 $\mu m$ thick.

*Young's modulus after post-development treatments*

Thermal treatments have been shown to improve the mechanical properties of IP-DIP (Nanoscribe GmbH & Co. KG, Germany) significantly, which was attributed to an increase in crosslinks between polymer chains [34]. Friction damping in polymer resonators is caused by the movement of polymer chains and is determined by the molecular structure of

the material [22] [28]. These statements suggest that post-development thermal treatment should consequently change friction damping of IP-DIP resonators. We were unable to directly measure friction damping with our equipment, so we performed an experiment on increasing Young's modulus of IP-S with different post-development treatments. Non-destructive compression experiments were conducted on IP-S square pillars to determine Young's modulus after different treatments. Each treatment was performed on separate samples of one substrate with 25 pillars.

The Young's modulus of untreated pillars was determined to be 2.3 $GPa$ on average, this was used as the reference value in Figure 5. An increase in Young's modulus was observed after all performed treatments. The largest increase (factor 1.5) was the thermal treatment at 200°C for 15 minutes, with a resulting average Young's modulus of 3.6 $GPa$. Ultraviolet light exposure for 40 minutes also showed a similar increase of Young's modulus with a factor of 1.4 to 3.3 $GPa$. Performing thermal treatment at both 200°C and 280°C for a longer duration of 45 minutes showed a smaller increase in Young's modulus. It is worth noting that the combination of ultraviolet light exposure for 40 minutes followed by thermal treatment of 200°C for 15 minutes showed a smaller increase than the separate treatments.

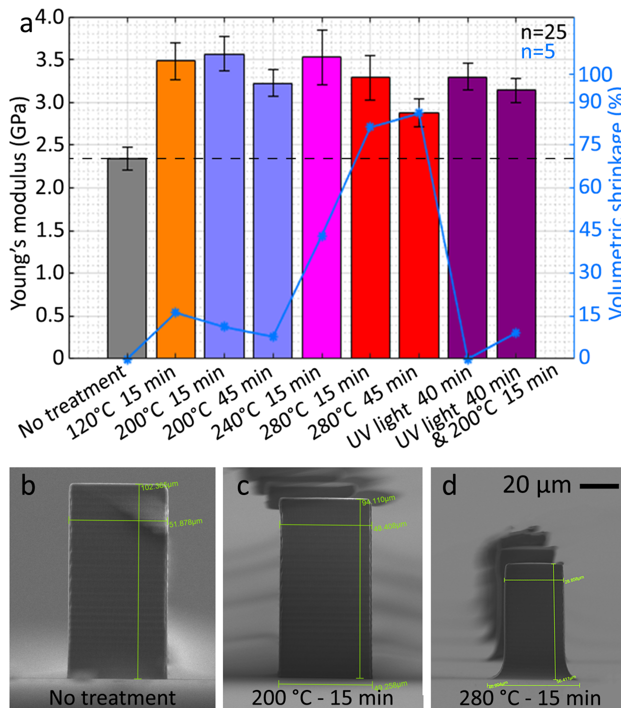


Fig. 5: (a) Young's modulus and volumetric shrinkage of IP-S pillars after different post-development treatments. (b) Pillar without post-development treatment. (c) Pillar after thermal treatment of 200°C for 15 minutes. (d) Pillar after thermal treatment of 280°C for 15 minutes. Images shown in (b), (c) and (d) have equal scales.

Shrinking of the pillars has only been observed for thermal treatments, see Figure 5 and appendix B for quantification and visualization. This effect has been accounted for during calculation of the Young's modulus. All thermal treatments at 200°C, including the combined treatment, showed a volumetric shrinkage within the same range of 8% and 11%. The thermal treatment at 240°C showed a volumetric shrinkage of 43%, while thermal treatments at 280°C had a volumetric shrinkage of 81% and 86%. Shrinkage showed a temperature-dependent upwards trend for post-development thermal treatments of IP-S, but it was not as clearly time-dependent for the shift of 15 to 45 minutes.

*Frequency spectra of 3D printed devices*

Characterization of the microbeams was performed using a Laser Doppler Vibrometer and excitation by a piezoelectric transducer using a pseudo-random signal with a frequency sweep ranging from 1 $Hz$ to 2 $MHz$. The fundamental resonant frequencies of the beams were identified by magnitude peaks and their matching mode shape. Figure 6 shows a part of the recorded frequency spectrum of a cantilever containing a distinct highest peak (number 2) and its corresponding mode shape, which is the fundamental resonant mode of the cantilever. The remaining magnitude peaks have similar mode shapes but with a moving anchor point. Peak 1 with a lower frequency has the anchor point moving in phase with the free end of the beam and peak 3 with a higher frequency has the anchor point moving anti-phase with the free end, as pointed out with the black arrow. This behavior has been observed across all devices. The peaks with a mode shape containing minimum displacement at the anchor points were selected to be the fundamental resonant frequency during this research. The phenomenon of multiple peaks also known as "forest of peaks" with similar mode shapes was observed across all experiments, despite efforts of changing the excitation voltage, single-point measurement, changing anchor geometry, distance from beam to the substrate, block splitting of beams or fabricating a single beam per substrate.

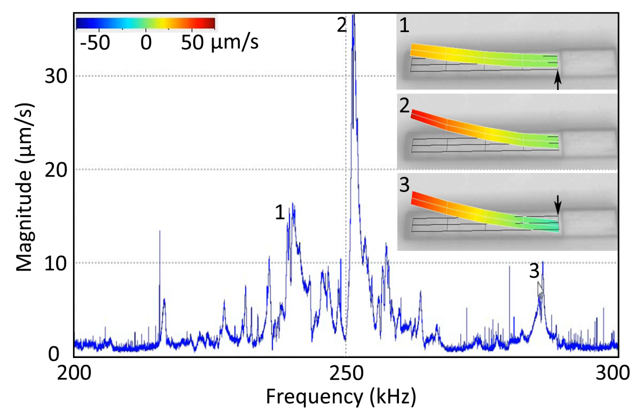


Fig. 6: The frequency spectrum of a thin type cantilever 100 $\mu m$ long consisting of IP-S on Silicon substrate, numbered peaks displayed with matching mode shape.

Figure 7 shows a bridge where this phenomenon was more apparent, peak 1 was assumed to be the fundamental resonant

frequency based on the fact that the anchor point moves less, even though it is not the peak with the largest magnitude. Figure 8 shows a bridge with a narrowed middle section where the forest of peaks is the most profound. Peak 2 was the assumed fundamental resonant frequency for that device, because of the mode shape containing minimal displacement at the anchor points.

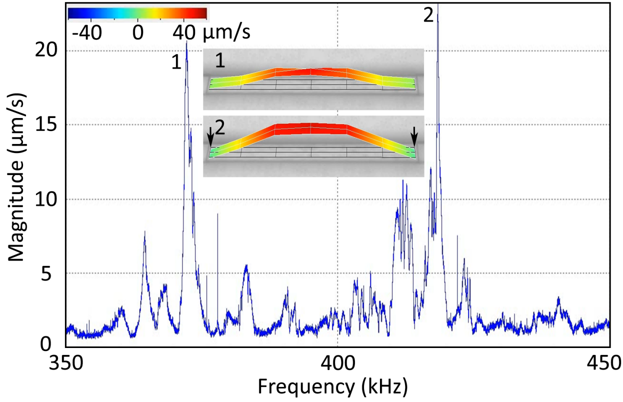


Fig. 7: The frequency spectrum of a thin type bridge 200 $\mu m$ long consisting of IP-S on Silicon substrate, numbered peaks displayed with matching mode shape.

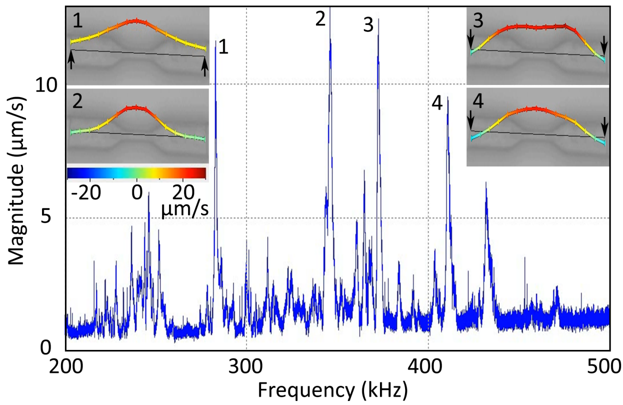


Fig. 8: The frequency spectrum of a thin type narrowed bridge 200 $\mu m$ long consisting of IP-S on Silicon substrate, numbered peaks displayed with matching mode shape.

*Substrate material vs. Quality factor*

Creating an impedance mismatch between the resonator and the substrate can help to increase the quality factor of a resonator that is dominated by clamping losses [35]. This impedance mismatch was used to reflect acoustic waves traveling from the resonator into the substrate, conserving energy in the resonator [36]. Changing the material of the substrate or resonator is a method of increasing the acoustic impedance mismatch between the resonator and the substrate. An experiment was performed to investigate the influence of the different substrate materials on the quality factor of 3D printed devices. The resonator material and substrate materials are shown in Table III with subsequent specific acoustic impedance. Characteristic specific acoustic impedance was calculated using equation 18, assuming longitudinal waves in a single-dimensional solid [37]. Young's modulus is denoted with $Y$, density with $\rho$ and specific acoustic impedance with $z0$.

$$z0 = \sqrt{Y * \rho} \tag{18}$$

TABLE III: Resonator and substrate materials with their subsequent specific acoustic impedance.

| Material | Specific acoustic impedance ($MPa * s/m$) | Source |
|---|---|---|
| IP-S | 1.7 | [38] |
| 3DM Tough clear | 1.4 | [39] [40] |
| Monocrystalline Silicon ⟨100⟩ | 17.4 | [41] [42] |
| Silicon Carbide polymorph 6H | 37.6 | [41] [43] |

Solid thick type cantilevers and bridges were 3D printed on top of the substrate materials and characterized. Beam lengths were varied to determine quality factors of the fundamental mode at frequencies between 50 $kHz$ and 1500 $kHz$. Results of this experiment are plotted in Figure 9 and shown in appendix C, showing that devices 3D printed on Silicon or Silicon Carbide substrates have similar averaged quality factor values at matching resonance frequencies with exception of some outliers. Cantilevers on Silicon showed a clear upwards curve that flattened out at higher resonance frequencies. Even though clamping conditions were different, bridges on Silicon were matching this trend. The highest average quality factor in this experiment was for the 100 $\mu m$ long cantilever on Silicon Carbide with 1126 at 455 $kHz$. This is a record-breaking quality factor value for polymer microbeam resonators, where the highest quality factor reported (of which the authors were aware at the time of writing this document) is 790 at 200 $kHz$ for a stressed double clamped beam [15]. Devices 3D printed on 3DM clear tough show a different quality factor trend, which contains lower averaged quality factor values with an exception of 2 points. Especially the 250 $\mu m$ long bridge deviated from the trend with the highest quality factor among bridges, namely 914 at 459 $kHz$. It should be noted that devices on 3DM had a shift in resonance frequency relative to the other substrate materials.

*Thermal treatment vs. Quality factor*

Previous research showed that friction damping has been the dominant damping phenomenon limiting the quality factors of most polymer microbeam resonators [15] [21], except for string-like microresonators. This material intrinsic phenomenon is not only dependent on temperature and frequency, but also on the molecular structure of the polymer. The previous experiment on post-development treatments of IP-S showed an increased Young's modulus of IP-S by thermal treatment after the development of the structures. In an attempt to improve the quality factor by changing the molecular structure of the polymer, microbeams were characterized after

thermal treatment at 200°C for 15 minutes. During this experiment, thick and thin type solid cantilevers and bridges of varying lengths were characterized at high vacuum pressure ($\leq 5 * 10^{-5} mbar$).

Results of this experiment were plotted in Figure 10 and shown in appendix C, showing that untreated cantilevers and bridges of both types have similar averaged quality factor values at matching resonance frequencies. All thermally treated devices showed an increase in resonance frequency compared to untreated devices, this can mostly be attributed to the increased Young's modulus observed in previous experiments. A generally small increase of the averaged quality factor has been observed for thermally treated devices in comparison to untreated devices, except for the thick type cantilevers with 200 $\mu m$ and 250 $\mu m$ length. Those two thermally treated devices with a resonant frequency of around 100 $kHz$ show a significantly lower averaged quality factor compared to the untreated ones with the same length. The largest increase in averaged quality factor is for the thin 200 $\mu m$ bridge with 136 at 135 $kHz$ for untreated devices, to a quality factor of 506 at 181 $kHz$ for thermally treated devices. The highest average quality factor in this experiment was for the thermally treated 100 $\mu m$ long thick cantilever with 993 at 473 $kHz$.

*Modelling damping source(s)*

Theoretical models for different damping phenomena are plotted together with the experimental data in Figure 10. The theoretical total damping is denoted by the dashed line, which can be calculated with equation 5. Theoretical values of $Q_{medium}$ were in the order of $10^6$, so they are out of range of the figure. In general, all devices showed an upwards trend in average quality factor plateauing from around 200 $kHz$. Although this trend was observed across all devices, the theoretical models did not fit the trend or the experimental data. The theoretical models of $Q_{TED}$ and $Q_{friction}$ from section II are highly dependent on the material properties of IP-S, which can vary strongly with different fabrication parameters [38] [44]. The material properties used for modeling are shown in Table IV. There was limited data available on the thermal and mechanical properties of IP-S, so the following assumptions and estimations were made in order to be able to plot models for thermoelastic damping and friction damping: Unavailable data for IP-S was replaced by data of IP-DIP (displaced with a *) and the Loss coefficient was conservatively estimated to be 0.1 from the Young's modulus - Loss coefficient graph in [45].

TABLE IV: Material properties of IP-S used for theoretical models and calculations

| Material property | Value | Source |
|---|---|---|
| Young's modulus | 2.3 $GPa$ | Used in this work |
| Relaxed Young's modulus* | 2.6 $GPa$ | [46] |
| Unrelaxed Young's modulus* | 3.2 $GPa$ | [46] |
| Loss coefficient | 0.1 | [45] |
| Mass density* | 1189 $kg/m^3$ | [38] |
| Thermal conductivity | 0.3 $W/mK$ | [47] |
| Coefficient of expansion | $100 * 10{-}6\ K^{-1}$ | [47] [44] |
| Heat capacity | 1500 $J/kgK$ | [47] |

*Thermal treatment of narrowed bridges*

String-like polymer microbeam resonators have been reported to achieve the highest quality factors [15], especially when tensile stress was present in the longitudinal direction of the beam. Tensile stress in strings led to an increased quality factor [48] because this adds stored energy to the system, changing the proportion between stored and lost energy (damping) [49]. A narrowed middle section on a double-clamped resonator was used to locally increase stress by reducing the cross-sectional area, therefore increasing the quality factor by strain engineering [50] [51]. Bridges were 3D printed with a narrowed middle section and thermally treated, in an attempt to create tensile stress by incorporating the thermally induced shrinkage observed in a previous experiment with 3D printed pillars.

Results of this narrowed bridge experiment are plotted in Figure 11 and shown in appendix C. Showing that narrowed bridges with and without thermal post-development treatment (200°C for 15 minutes) had similar averaged quality factor values with one pronounced exception: The narrowed bridge with a length of 200 $\mu m$ showed a significant increase in average quality factor, from 522 at 361 $kHz$ for no treatment to 1819 at 424 $kHz$ for 200°C for 15 minutes. This averaged value is considered the new record for polymer microbeam resonators (of which the authors were aware at the time of writing this document), more than doubling the previous record of 790 at 200 $kHz$ for a stressed double-clamped beam [15]. Pushing the mass resolution of the 200 $\mu m$ long devices down to $19 \frac{1}{SNR}\ fg$. An increase in resonance frequency was observed from untreated to the treated narrowed bridges as shown in Figure 12. The largest relative frequency increase was for the 200 $\mu m$ long devices, which also had a significant increase in quality factor. This could be an indication of tensile stress in this particular device length.

A formula was derived to estimate the tensile stress in the narrowed bridges, based on the experimentally observed shift in resonance frequency between untreated and treated devices. The following assumptions were made during the derivation of the formula for tensile stress: Conservation of mass, untreated beams had no prior stress present, cross-section did not vary along the length of the beam and length did not change by the treatment. The resonance frequency shift will be denoted with $F$, which is the frequency shift factor calculated in equation 19.

$$F = \frac{f_{R,treated}}{f_{R,untreated}} \tag{19}$$

The resonance frequency of a double-clamped beam with tensile stress $\sigma$ can be calculated using equation 20 [22].

$$f_{R,n} = \frac{n^2\pi}{2l^2}\sqrt{\frac{YI}{\rho A}}\sqrt{1+\frac{\sigma A l^2}{YIn^2\pi^2}} \tag{20}$$

Substitution of $A = bh$ and $I = \frac{1}{12}bh^3$ [52] led to equation 21.

$$f_{R,n} = \frac{n^2\pi}{2l^2}\sqrt{\frac{Yh^2}{12\rho}}\sqrt{1+\frac{12\sigma l^2}{Yh^2n^2\pi^2}} \tag{21}$$

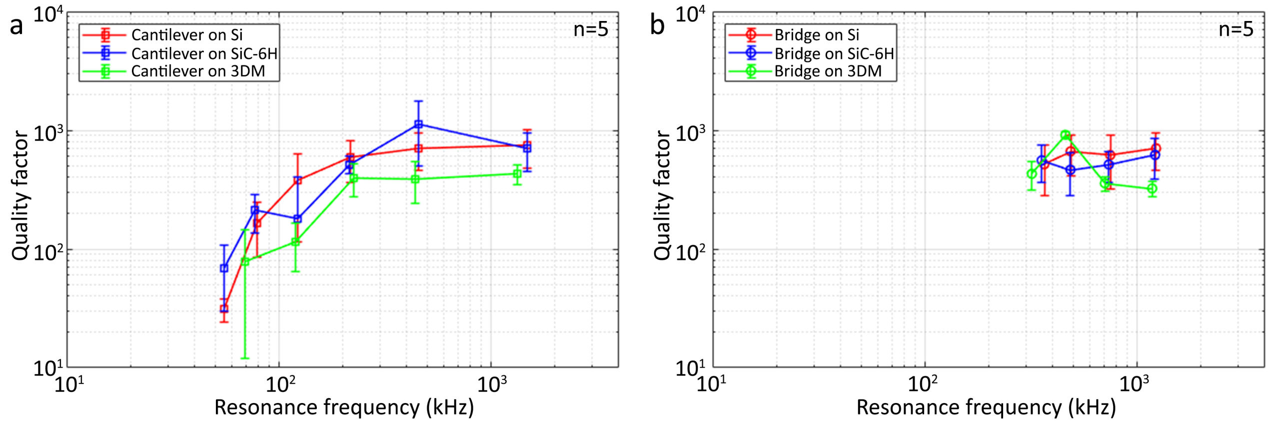


Fig. 9: Quality factors of a) thick cantilevers and b) thick bridges printed on three different substrate materials.

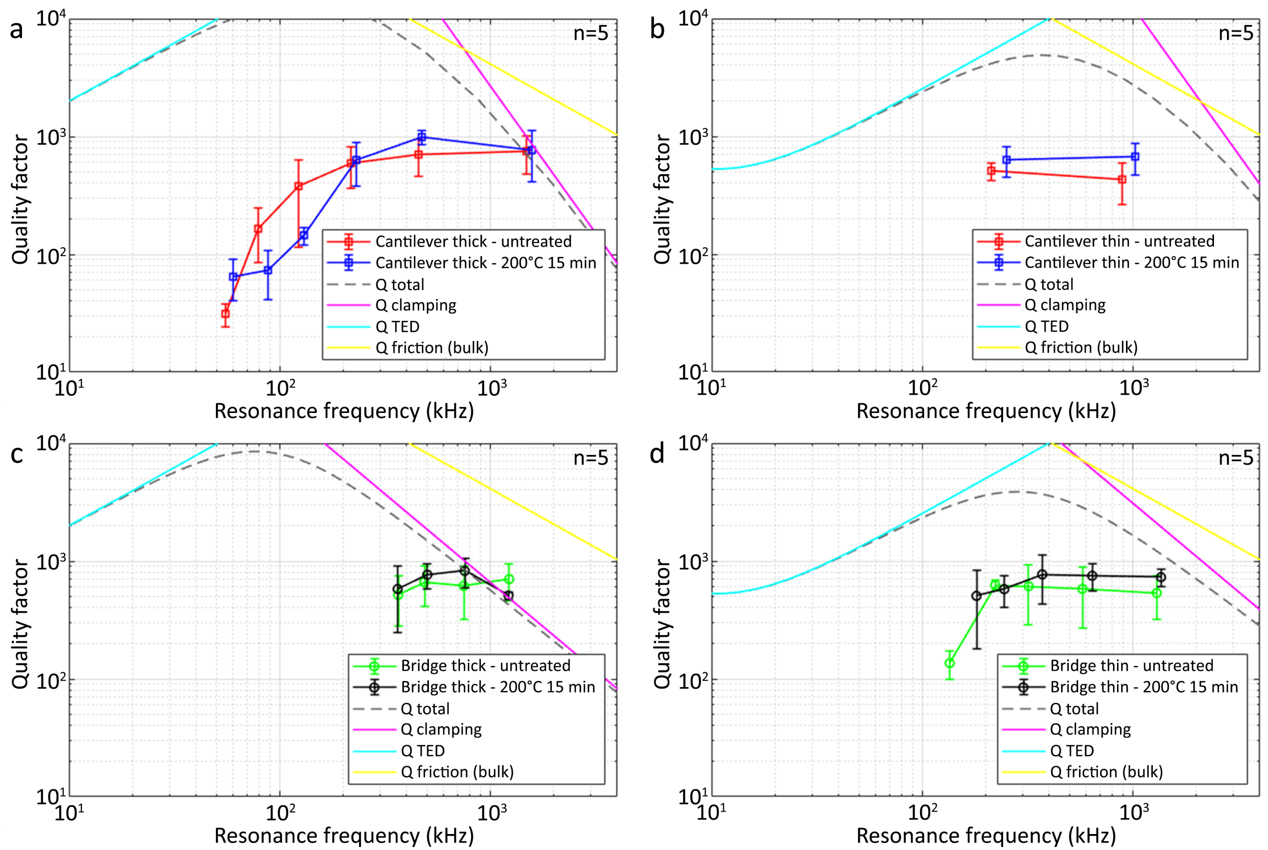


Fig. 10: Quality factors of a) thick cantilevers, b) thin cantilevers, c) thick bridges and d) thin bridges with and without thermal treatment. Plotted quality factor lines represent theoretical models of different damping phenomena.

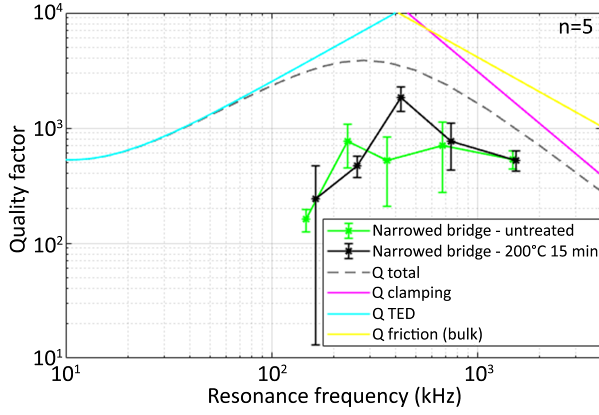


Fig. 11: The quality factor of thin type narrowed bridges with and without thermal treatment. Plotted quality factor lines represent theoretical models of different damping phenomena.

It should be noted that Young's modulus, mass density and height changed by the thermal treatment. The resulting effects on the resonance frequency were accounted for using correction factor $C_F$, which was calculated using equation 22. That was derived from the dependent variables of the first part of equation 21.

$$C_F = \frac{\sqrt{\frac{Y_{treated}h^2_{treated}}{\rho_{treated}}}}{\sqrt{\frac{Y_{untreated}h^2_{untreated}}{\rho_{untreated}}}} \tag{22}$$

Substitution of equation 21 in equation 19, correcting $F$ through dividing it by the correction factor and isolation of tensile stress yielded equation 23. The tensile stress in the thermally treated bridges was calculated with equation 23.

$$\sigma_{n,treated} = \left(\left(\frac{F}{C_F}\right)^2 - 1\right) * \left(\frac{Y_{treated}h^2_{treated}n^2\pi^2}{12l^2}\right) \tag{23}$$

The local tensile stress in the narrowed part of the bridge was calculated with equation 24 [52].

$$\sigma_{narrowed} = \sigma_{n,treated}\frac{A}{A_{narrowed}} \tag{24}$$

The estimated tensile stress in the thermally treated narrowed bridges are plotted in blue against their length in Figure 12. The 200 $\mu m$ long devices were the only ones containing positive tensile stress ($1.4 * 10^5\ Pa$). Simulations were performed to verify if the observed shift in resonance frequency between untreated and treated devices was caused by tensile stress. The analytically calculated tensile stress was used to estimate the expected values of $F$ through FEM simulation. The change in Young's modulus, mass density and beam thickness by the thermal treatment were also incorporated in the simulation. Simulated frequency shift factors were plotted together with the experimentally determined values in Figure 12. Experimental values of $F$ were not fitting the simulated values, but follow the same trend. The analytical model indicated that only the 200 $\mu m$ long devices had positive tensile stress, and simulations showed qualitative agreement. Additionally, both models showed that positive tensile stress should have been present in thermally treated narrowed bridges for frequency shift factors above 1.13.

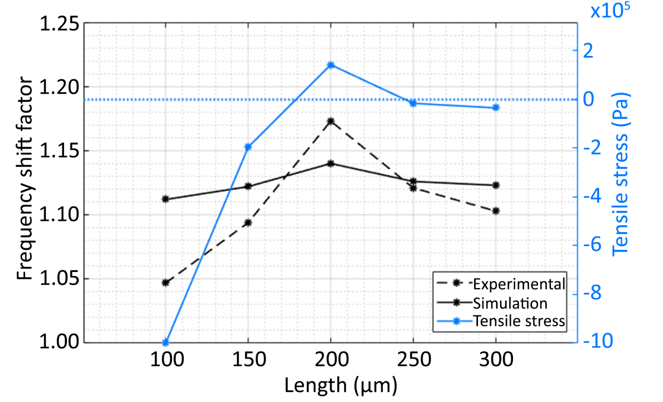


Fig. 12: The dashed black line indicates the experimentally determined frequency shift factor $F$ of thin type narrowed bridges of different beam lengths. The blue line indicates the tensile stress calculated with the model based on the experimental determined $F$ values. The black solid line shows the $F$ from simulations using the calculated tensile stress.

*Suspended microchannel resonator*

Following the study of the damping mechanisms on solid 3D printed beams, suspended microchannel resonators (hollow beams) were printed to demonstrate the suitability of the process to fabricate devices that can carry liquids. Theoretical optimization was performed to determine the best geometry of the suspended microchannel resonator within the bounds of fabrication capabilities and limitations of our measurement equipment, see Table V for the boundary conditions. The goal of optimization was to maximize the mass responsivity of the device, in order to make the shift in resonance frequency due to added mass as large as possible. The suspended microchannel resonator will be double clamped because of the design simplicity when incorporating fluidic channels and the comparable performance of cantilevers and bridges in the previous experiments. The mass responsivity of a bridge with a square channel can be calculated with Equation 25 [53]. Subscript $_c$ denotes the channel and $_{fluid}$ the fluid in the channel. Note that beam mass should be minimized and resonance frequency should be maximized to obtain maximal mass responsivity.

$$\Re = \frac{\partial f}{\partial m} = -\frac{f_{R,n}}{2m_{eff}} = -\frac{a_n^2}{4\pi}\sqrt{\frac{Y(wh^3 - w_ch_c^3)}{12l^6(wh\rho + w_ch_c(\rho_{fluid} - \rho))^3}} \tag{25}$$

The resulting optimal dimensions are a 119 $\mu m$ long bridge with an internal square channel of 10 $\mu m$ by 10 $\mu m$, a width of 12 $\mu m$ and a height of 16 $\mu m$. This suspended microchannel resonator has a theoretical mass responsivity of $-6.5 * 10^{19}\ Hz/kg$ when filled with water. Prototypes

TABLE V: Boundary conditions for optimization of suspended microchannel resonator.

| Boundary condition | Origin of limit | Value |
|---|---|---|
| Size of voxel XY-direction | Fabrication tool | 1 $\mu m$ |
| Size of voxel Z-direction | Fabrication tool | 3 $\mu m$ |
| Minimal channel diameter | Chemical development | 10 $\mu m$ |
| Maximal resonance frequency | Characterization tool | 1.5 $MHz$ |

were fabricated on top of 3DM fluidic interfaces for easy fluidic connection, see Figure 13 and 14 for the SMR and the interface. Unfortunately, we were unable to demonstrate the mass sensing capabilities of the prototypes due to clogging and leaking. Adhesion problems between the fluidic interface and 2PP-fabricated domes prevented leak-tight connections.

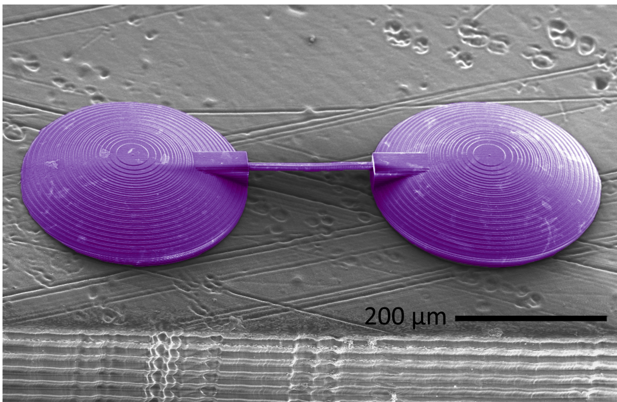


Fig. 13: Colored electron microscopy image of suspended microchannel resonator with domes (purple) for microfluidic connection to the interface (grey).

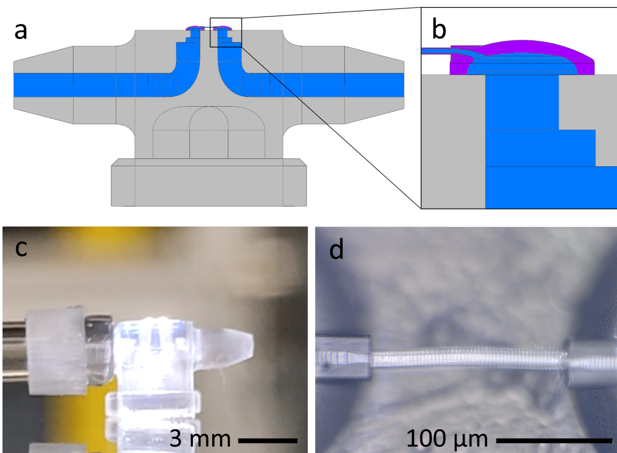


Fig. 14: a) Schematic of the internal fluidic channel (blue) inside interface (grey). b) Zoom on the schematic of the internal fluidic channel (blue) with domes and suspended microchannel resonator (purple) connected to the interface (grey). c) Interface with fluidic connection to tubing on the left and unused connection on the right. d) Top view of suspended microchannel resonator with the visible internal channel.

The mass resolution of the SMR was estimated to be $47\frac{1}{SNR}\ fg$ when theoretical models from section II were used to calculate the effective quality factor ($Q = 414$), see in Table VI for the values. It should be noted that clamping damping was the most dominant type of damping followed by medium interaction damping by the liquid inside the resonator. The mass resolution of the SMR was estimated to be $60\frac{1}{SNR}\ fg$, solely based on the experimentally determined quality factor of thick bridges on 3DM substrates around $1.5MHz$ ($Q = 323$).

TABLE VI: Quality factor values for different damping sources of the suspended microchannel resonator.

| Damping type | Q |
|---|---|
| Theoretical medium interaction damping (liquid inside resonator) | 1251 |
| Theoretical clamping damping | 622 |
| Theoretical total damping | 414 |
| Estimated total damping (based on experimental findings) | 323 |

## V. Discussion

*Post-development treatments*

A clear increase in Young's modulus was observed for both thermal treatments and ultraviolet light exposure of IP-S post-development. The increased Young's modulus after ultraviolet light exposure suggests incomplete polymerization of the monomers in the IP-S material. Hence the combination of ultraviolet light exposure for 40 minutes followed by thermal treatment of 200°C for 15 minutes showed a slightly smaller increase than the separate treatments. Suggesting that the mechanisms involved with increasing Young's modulus for those treatments did not add up and had the same effect. Shrinkage was within equal range for thermal treatment of 200°C for 15 minutes with and without prior ultraviolet light exposure, this suggests that only thermally driven mechanisms were involved with volumetric change. It should be noted that the degradation temperature of IP-S is 300°C and that a weight loss of 2% was observed at 280°C [54]. This in addition to the observed shape of the thermally treated pillars, shown in Figure 5 and appendix B, verified that the material shrunk and was not degraded.

*Origins of multiple resonance peaks*

Fundamental resonant frequencies of the beams were identified by magnitude peaks and their matching mode shape. Multiple peaks with similar mode shapes were observed across all experiments, but only the peak with a mode shape containing minimum displacement at the anchor point(s) was selected to be the fundamental resonant frequency. Coupling of the resonators with each other through the substrate could be argued to cause multiple peaks. Although the resonators fabricated on a single substrate had different fundamental resonant frequencies, different modes could still be coupled with the fundamental mode of another resonator fabricated on the same substrate. This cause was ruled out because the devices with the lowest resonant frequencies still had multiple peaks and fabricating a single beam per substrate didn't solve the issue. ”Additional” resonant peaks with similar mode shapes but moving anchor points suggest a mechanical coupling between

the beam and other resonating parts such as the piezoelectric transducer assembly, substrate or the anchor itself. Energy transfer through this coupling intensifies when the frequencies of substrate and resonator modes are closer together [55] [56]. This suggests that those ”additional” peaks are coupled substrate modes or anchor modes, which should not be fitted for characterization. Literature suggests that the resonances of the piezoelectric transducer (assembly) could also be the cause of the ”forest of peaks” phenomenon [57] [58]. Both causes agreed with the following unsuccessful attempts performed to solve this problem: Varying the excitation voltage, performing single point measurement, changing anchor geometry, varying distance from beam to the substrate, eliminating block splitting of beams or fabricating a single beam per substrate.

*Acoustic mismatch substrate materials*

The experiment on the effect of different substrate materials on the quality factor of resonators showed the following: 3DM clear tough (polymer) had generally lower averaged quality factor values than Silicon or Silicon Carbide. The characteristic specific acoustic impedance of 3DM clear tough (1.4 $MPa*s/m$) was close to that of IP-S (1.7 $MPa*s/m$), but those of Silicon (17.4 $MPa*s/m$) and Silicon Carbide (37.6 $MPa*s/m$) were significantly larger. Suggesting that the impedance mismatch, created by changing the material of the substrate, increased the averaged quality factors by conserving energy in the resonators. Hence it could be argued that resonators on 3DM substrates were (partly) dominated by clamping losses, caused by acoustic waves traveling from the resonator into the substrate.

*Discrepancy between damping models and experimental results*

The theoretical damping models did not fit the experimental data across all devices. The models of thermoelastic damping and friction damping are highly dependent on material properties, which can vary strongly with different fabrication parameters [38] [44]. Furthermore unavailable data for IP-S was replaced by data of IP-DIP on the following material properties: Relaxed Young’s modulus, Unrelaxed Young’s modulus and mass density. In addition to that, the loss coefficient used in the friction damping model was estimated to be 0.1, because there was no data available on similar materials. This high uncertainty of the material properties used in these models explains the mismatch between theory and experiments. Fitting the models to experimental data was not possible without significantly tuning the values of material properties. Studying those material properties is recommended for future work. Finally, the friction damping model was based on a single relaxation time in contrary to a real polymer, which could have multiple relaxation times [59]. These were enough reasons to not take the quality factor values of the theoretical models into account during the determination of the dominant damping phenomenon, but only the theoretical dependencies.

*Dominant damping source*

The fundamental question of finding the dominant damping source(s) for solid devices was answered by eliminating damping sources in equation 5. Experimental results and theoretical models will be compared in order to eliminate damping sources based on their theoretical dependencies. In order to be able to single out damping sources, the following variations were fabricated: Beam length (resonance frequency), beam thickness and clamping type. The quality factor values of thermoelastic damping are dependent on beam thickness, which is also displayed by the model used in Figure 10. The experimental results show that changing the thickness of beams didn’t affect the quality factor values at matching resonant frequencies. This suggests that thermoelastic damping can be eliminated as a dominant damping source. The quality factor values of the models for clamping damping are different for cantilevers, bridges and varying beam thicknesses. Cantilevers and bridges showed to have similar quality factors at matching resonant frequencies for both thick and thin devices, suggesting that clamping damping can also be eliminated as a dominant damping source. Medium interaction damping will be eliminated based on the theoretical values of $Q_{bsf}$ and $Q_{bdf}$, being 3 orders of magnitude higher than the total quality factor in the experiments. S. Schmid showed experimentally that the influence of air damping vanishes for comparable devices with pressures below ($10^{-1}$ $mbar$) [22]. All devices in this work are measured at a high vacuum pressure of $\leq 5*10^{-5}$ $mbar$, therefore medium interaction damping could be eliminated based on theoretical models and experimental findings from the literature. After eliminating damping sources based on their theoretical dependencies and the experimental results, bulk friction damping was determined to be the dominant damping source for all devices. The large discrepancies between the theoretical estimations and the measured quality factors can be explained by the uncertainty in material properties, as discussed above.

*Effects of thermal treatment on quality factor*

Quality factors of solid cantilevers and bridges, dominated by friction damping, didn’t change significantly by post-development thermal treatment at 200°C for 15 minutes, even though Young’s modulus changed by a factor of 1.5. This suggests that the friction damping was not changed (significantly) by the supposed increase in cross-links between polymer chains. Only the narrowed bridges of 200 $\mu m$ long did see a large increase in quality factor after thermal treatment. This was not caused by a change in friction damping but by the change in the proportion between stored and lost energy (damping) due to the tensile stress adding stored energy to the system [48] [49]. The largest average frequency shift and average quality factor increase were observed for the 200 $\mu m$ long narrowed bridges. This not only indicated that tensile stress was present in devices with these dimensions (n=5), but that locally increasing this stress by reducing the cross-sectional area led to significantly increased average quality factors. This demonstrated a successful case of strain engineering because only a small increase in average quality factor was observed

for the thin type bridges (without narrowing) of 200 $\mu m$ long with the same thermal treatment. Although simulations verified that a frequency shift factor above 1.13 is caused by positive tensile stress in the beam, it didn't give an explanation why only 200 $\mu m$ long devices had it. It is suspected that prior plastic deformation and negative tensile stress were present in the beams before thermal treatment. It was observed that narrowed bridges were slightly bent down towards the surface of the substrate after fabrication, see appendix D, supposedly caused by capillary forces generated by the surface tension of the evaporating development liquid [60]. Increasing plastic deformation was expected for longer beams due to their lower stiffness. The previous phenomenon was believed to have a competing effect with a length dependency of induced (positive) tensile stress by volumetric shrinkage. Increasing tensile stress should be induced for longer beams, assuming uniform shrinkage, fixed anchor points and constant cross-sectional area for different beam lengths. The combination of the two competing effects left long beams too deformed to shrink enough to induce positive tensile stress and short beams with not enough longitudinal shrinkage to induce positive tensile stress. This provided a speculative explanation for the local maximum in the frequency shift factor plot and its derived stress.

*Comparison with state of the art*

The quality factors of the devices in this work have exceeded the state of the art in polymer microbeam resonators. Figure 15 displays the state of the art including the devices from this work based on their resonance frequency and quality factor. The figure shows that the 3D printed devices in this work set a new standard for polymer microbeam resonators in a resonance frequency range from 60 $kHz$ to 1500 $kHz$, with a single exception to the stressed bridge of Schmid et al, with a Q of 790 at 200 $kHz$ [49]. The figure not only showed that these polymer cantilevers and bridges approached a quality factor of 1000, but also that tensile-stressed narrow bridges went beyond that.

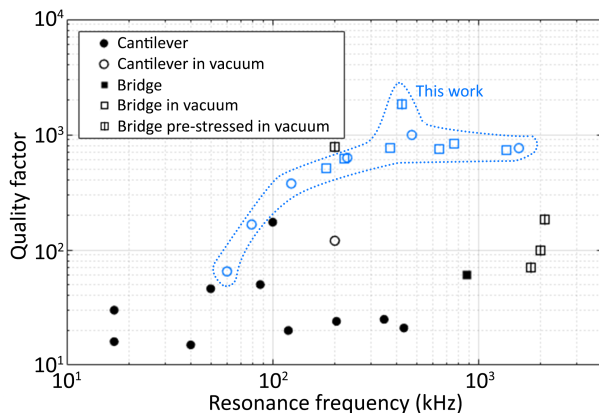


Fig. 15: State of the art for the performance of polymer microbeam resonators including this work in blue [10], [11], [13], [14], [16]–[24]

*Multiscale 3D printed suspended microchannel resonator*

Clogging and leaking of the suspended microchannel resonator prototypes prevented us from performing mass sensing experiments and demonstrating the capabilities of the device. Leakages occurred at the interface of the 3DM tough clear and IP-S, suggesting weak adhesion between the two materials. This could be caused by the 2 $nm$ layer of gold-sputtered prior to the 3D printing of IP-S structures. Bubble formation during printing, prior substrate UV light exposure and varying laser dosages were also speculated to influence adhesion quality between the two materials. Geometrical optimization of the suspended microchannel resonator for maximal theoretical mass responsivity was limited by the capabilities of fabrication and measurement equipment. Further improvement could be achieved by overcoming these limitations by improving the chemical development process, using a higher magnification printing lens and changing measurement equipment. These improvements will enhance the mass resolution. It could be argued that the estimated mass resolution of $60\frac{1}{SNR}$ $fg$ was correct, because it was based on the experimentally determined average quality factor of thick bridges on 3DM substrates around $1.5MHz$. These bridges had comparable dimensions and resonance frequency, their experimentally determined quality factor was smaller than the theoretical values of the clamping damping model and the model for medium interaction damping by the liquid inside the resonator. The results demonstrate that the mass resolution of this device is enough to be able to detect live E. Coli bacteria with a buoyant mass in water of 175 $fg$ [61].

Our SMR had a smaller theoretical mass resolution as the Silicon Dioxide one from Calmo et al (110 $fg$) with the same channel diameter [7], a similar mass resolution as the Silicon device from Manalis et al. with a slightly larger channel (50 $fg$) [62] and a larger mass resolution than the Silicon devices from Manalis et al. with a smaller channel (3 $fg$ and 26 $fg$) [63], all without including the signal-to-noise ratio to our SMR. It could be argued that the mass resolution of our SMR will only improve when the signal-to-noise ratio $(SNR)$ is determined, because the signal-to-noise ratio should be $> 1$ to be able to measure any signal. It should be noticed that the mass density of IP-S (1189 $kg/m3$) is significantly lower than materials typically used for SMRs and resonant microbeams, such as Silicon (2330 $kg/m3$) and Silicon-based materials like Silicon Dioxide or Silicon Nitride ($2201 - 3187$ $kg/m3$) [41] [4]. Giving the devices in this work a great advance in mass resolution when working in lower quality factor ($Q < 1000$) conditions dominated by medium interaction damping, such as submerged in liquid, atmospheric pressure or certain liquid inside the resonator cases. Another key advantage of these multi-scale 3D printed devices was the flexible and accessible end-to-end fabrication.

## VI. Conclusion

The goal of this work was to find the smallest mass resolution of a 3D printed suspended microchannel resonator designed for buoyant mass sensing of E. Coli bacteria. This was realized by focusing the research on understanding the

fundamentals of damping in 3D printed polymer microbeam resonators, maximizing their quality factor and therefore minimizing their mass resolution. Laying the foundations for future applications of 3D printed polymer resonators, considering the damping behavior of these materials was previously unknown. Important design considerations and potential methods of improving the quality factor were investigated. Showing that thermal post-development treatment had increased Young's modulus of the 3D printing material IP-S by a factor of 1.5 and also shrank the material substantially. This effect was incorporated to enhance the quality factor of microbeam resonators by creating tensile stress in narrow bridges. Furthermore, the influence of substrate acoustic impedance on the quality factor of microbeam resonators was studied, concluding that a small acoustic impedance mismatch between the materials of the resonator and substrate could degrade the quality factor significantly.

The fundamental question; "What is the dominant damping source?" was answered by eliminating sources based on experimental results and their theoretical dependencies. The theoretical damping models did not fit the experimental data across all devices, because the models were highly dependent on uncertain or unknown material properties. Nevertheless, damping sources could be singled out by varying the resonator beam length (resonance frequency), beam thickness and clamping type. Concluding that bulk friction damping was the dominant damping source for all devices.

The 3D printed devices from this work set a new quality factor standard among polymer microbeam resonators. Cantilevers and bridges characterized at high vacuum pressure ($\leq 5 * 10^{-5} mbar$) approached quality factors of 1000 and the tensile-stressed narrow bridges went beyond this achieving a quality factor of 1819. The theoretical mass resolution of the 200 $\mu m$ long tensile stressed narrow bridges was determined to be $7\frac{1}{SNR}\ fg$.

Prototypes of the suspended microchannel resonator were fabricated with multi-scale 3D printing creating an easy connection to fluidics and measurement equipment. Unfortunately, we were unable to demonstrate the mass sensing capabilities of the prototypes due to temporal limitations. Nevertheless, its mass resolution was estimated to be $60\frac{1}{SNR}\ fg$ based on the experimentally determined quality factor of solid bridges with similar dimensions and resonance frequency. The mass resolution of this SMR will only improve when the signal-to-noise ratio ($SNR$) is determined. This device would be able to detect E.Coli bacteria (175 $fg$ buoyant in water) and compete with (similar channel diameter) SMRs typically made of silicon-based materials. It should be noticed that the mass density of IP-S is significantly lower than Silicon-based materials, giving the devices in this work a great advantage when working in lower quality factor ($Q < 1000$) conditions dominated by medium interaction damping.

The key advantage of multi-scale 3D printed suspended microchannel resonators was the flexible and accessible end-to-end fabrication, yielding rapid prototypes of plug-and-play devices. Characterizing 3D printed polymer microbeam resonators, maximizing their quality factor and determining their theoretical mass resolution paves the path towards actual biosensing 3D printed SMRs with the capabilities of lithography-based fabricated devices but with additional design and fabrication flexibility.

## VII. Outlook

Solving leaking and clogging problems of the SMR would make it able to demonstrate biological mass sensing capabilities. Further mass resolution improvements could be feasible by breaching fabrication limits, upgrading measurement equipment, changing device material, improving the incorporation of strain engineering and higher resonant mode operation. A novel method for 3D printing of Silicon Dioxide and ceramics has already been achieved by suspending nanoparticles in the 2PP polymer resin and performing post-development thermal treatment and sintering. 3D printed Silicon Dioxide and ceramic resonators have been demonstrated to push the quality factors beyond $10^4$ [64] [65]. The mass resolution of solid devices has been shown to improve significantly ($0.45\ ag$) using these materials (and smaller dimensions), even though the materials have a larger mass density compared to polymer devices. Making the 3D printed Silicon Dioxide and ceramic resonators superior in low medium interaction damping environments. The novel method had a sub-$200nm$ fabrication resolution, pushing 3D printed beam resonators toward the capabilities of lithography-based fabricated devices with additional design and fabrication flexibility. Single-cell analysis with multi-scale 3D printed devices could also be advanced by combining the SMR for mass sensing with the high volume resolution pipetting systems from [66] [67]. Arrays of suspended nanochannel resonators with integrated piezo actuators are expected to increase capabilities for the detection of (biological) nanoparticles [68]. While multi-material multi-photon polymerization has been opening up new fabrication possibilities for multi-material 3D printing of MEMS and NEMS with integrated electrical components [69]. Leading to a promising future for a flexible and accessible end-to-end fabrication of biological sensors.

## Acknowledgment

I would like to express my gratitude to my supervisors Tomás Manzaneque Garcia and Murali Krishna Ghatkesar for their weekly advice, discussions and constructive feedback. Their contribution to this work are of great value. I would like to thank Murali for initialising this project and having a decisive role in terms of the research aim. I am thankful for Tomás his guidance and experimental expertise during this project. Furthermore, I would like to thank my colleague Pieter van Altena for the practical training and lab brainstorm sessions. I would also like thank the MNE lab staff for their practical support.

## References

[1] S. E. Cross, Y.-S. Jin, J. Rao, and J. K. Gimzewski, "Nanomechanical analysis of cells from cancer patients," *Nature nanotechnology*, vol. 2, no. 12, pp. 780–783, 2007.

[2] U. F. Greber, "Virus and host mechanics support membrane penetration and cell entry," *Journal of virology*, vol. 90, no. 8, pp. 3802–3805, 2016.

[3] S. Suresh, J. Spatz, J. Mills, A. Micoulet, M. Dao, C. Lim, M. Beil, and T. Seufferlein, "Reprint of: connections between single-cell biomechanics and human disease states: gastrointestinal cancer and malaria," *Acta biomaterialia*, vol. 23, pp. S3–S15, 2015.

[4] A. De Pastina and L. G. Villanueva, "Suspended micro/nano channel resonators: a review," *Journal of Micromechanics and Microengineering*, vol. 30, no. 4, p. 043001, 2020.

[5] E. Gil-Santos, J. J. Ruz, O. Malvar, I. Favero, A. Lemaître, P. M. Kosaka, S. García-López, M. Calleja, and J. Tamayo, "Optomechanical detection of vibration modes of a single bacterium," *Nature nanotechnology*, pp. 1–6, 2020.

[6] S. Byun, S. Son, D. Amodei, N. Cermak, J. Shaw, J. H. Kang, V. C. Hecht, M. M. Winslow, T. Jacks, P. Mallick *et al.*, "Characterizing deformability and surface friction of cancer cells," *Proceedings of the National Academy of Sciences*, vol. 110, no. 19, pp. 7580–7585, 2013.

[7] R. Calmo, A. Lovera, S. Stassi, A. Chiadò, D. Scaiola, F. Bosco, and C. Ricciardi, "Monolithic glass suspended microchannel resonators for enhanced mass sensing of liquids," *Sensors and Actuators B: Chemical*, vol. 283, pp. 298–303, 2019.

[8] J. Chaste, A. Eichler, J. Moser, G. Ceballos, R. Rurali, and A. Bachtold, "A nanomechanical mass sensor with yoctogram resolution," *Nature nanotechnology*, vol. 7, no. 5, pp. 301–304, 2012.

[9] T. P. Burg, A. R. Mirza, N. Milovic, C. H. Tsau, G. A. Popescu, J. S. Foster, and S. R. Manalis, "Vacuum-packaged suspended microchannel resonant mass sensor for biomolecular detection," *Journal of Microelectromechanical Systems*, vol. 15, no. 6, pp. 1466–1476, 2006.

[10] L. Frehner and D. Maillard, "Optimization of channel design and fabrication for suspended microchannels resonators with a 3d nanoprinter," Tech. Rep., 2018.

[11] R. C. Kramer, E. J. Verlinden, L. Angeloni, A. Van Den Heuvel, L. E. Fratila-Apachitei, S. M. Van Der Maarel, and M. K. Ghatkesar, "Multiscale 3d-printing of microfluidic afm cantilevers," *Lab on a Chip*, vol. 20, no. 2, pp. 311–319, 2020.

[12] S. Schmid, P. Wägli, and C. Hierold, "All-polymer microstring resonant humidity sensor with enhanced sensitivity due to change of intrinsic stress," *Micro and Nanosystems*, 2008.

[13] G. Genolet, J. Brugger, M. Despont, U. Drechsler, P. Vettiger, N. De Rooij, and D. Anselmetti, "Soft, entirely photoplastic probes for scanning force microscopy," *Review of scientific instruments*, vol. 70, no. 5, pp. 2398–2401, 1999.

[14] P. Urwyler, H. Schift, J. Gobrecht, O. Häfeli, M. Altana, F. Battiston, and B. Müller, "Surface patterned polymer micro-cantilever arrays for sensing," *Sensors and Actuators A: Physical*, vol. 172, no. 1, pp. 2–8, 2011.

[15] S. Schmid and C. Hierold, "Damping mechanisms of single-clamped and prestressed double-clamped resonant polymer microbeams," *Journal of Applied Physics*, vol. 104, no. 9, p. 093516, 2008.

[16] A. W. McFarland, M. A. Poggi, L. A. Bottomley, and J. S. Colton, "Production and characterization of polymer microcantilevers," *Review of scientific instruments*, vol. 75, no. 8, pp. 2756–2758, 2004.

[17] ——, "Injection moulding of high aspect ratio micron-scale thickness polymeric microcantilevers," *Nanotechnology*, vol. 15, no. 11, p. 1628, 2004.

[18] T. Xu, M. Bachman, F.-G. Zeng, and G.-P. Li, "Polymeric microcantilever array for auditory front-end processing," *Sensors and Actuators A: Physical*, vol. 114, no. 2-3, pp. 176–182, 2004.

[19] M. Calleja, M. Nordström, M. Álvarez, J. Tamayo, L. M. Lechuga, and A. Boisen, "Highly sensitive polymer-based cantilever-sensors for dna detection," *Ultramicroscopy*, vol. 105, no. 1-4, pp. 215–222, 2005.

[20] S. Mouaziz, G. Boero, R. S. Popovic, and J. Brugger, "Polymer-based cantilevers with integrated electrodes," *Journal of microelectromechanical systems*, vol. 15, no. 4, pp. 890–895, 2006.

[21] G. Zhang, V. Chu, and J. P. Conde, "Conductive blended polymer mems microresonators," *Journal of microelectromechanical systems*, vol. 16, no. 2, pp. 329–335, 2007.

[22] S. Schmid, *Electrostatically actuated all-polymer microbeam resonators: Characterization and application*. ETH Zurich, 2009, vol. 6.

[23] C. Accoto, A. Qualtieri, F. Pisanello, C. Ricciardi, C. F. Pirri, M. De Vittorio, and F. Rizzi, "Two-photon polymerization lithography and laser doppler vibrometry of a su-8-based suspended microchannel resonator," *Journal of Microelectromechanical Systems*, vol. 24, no. 4, pp. 1038–1042, 2014.

[24] N. Hosseini, M. Neuenschwander, O. Peric, S. H. Andany, J. D. Adams, and G. E. Fantner, "Integration of sharp silicon nitride tips into high-speed su8 cantilevers in a batch fabrication process," *Beilstein Journal of Nanotechnology*, vol. 10, no. 1, pp. 2357–2363, 2019.

[25] M. K. Ghatkesar, V. Barwich, T. Braun, J.-P. Ramseyer, C. Gerber, M. Hegner, H. P. Lang, U. Drechsler, and M. Despont, "Higher modes of vibration increase mass sensitivity in nanomechanical microcantilevers," *Nanotechnology*, vol. 18, no. 44, p. 445502, 2007.

[26] A. Cleland and M. Roukes, "Noise processes in nanomechanical resonators," *Journal of applied physics*, vol. 92, no. 5, pp. 2758–2769, 2002.

[27] B. Hauer, C. Doolin, K. Beach, and J. Davis, "A general procedure for thermomechanical calibration of nano/micro-mechanical resonators," *Annals of Physics*, vol. 339, pp. 181–207, 2013.

[28] S. Schmid, L. G. Villanueva, and M. L. Roukes, *Fundamentals of nanomechanical resonators*. Springer, 2016, vol. 49.

[29] M. K. Ghatkesar, T. Braun, V. Barwich, J.-P. Ramseyer, C. Gerber, M. Hegner, and H. P. Lang, "Resonating modes of vibrating microcantilevers in liquid," *Applied Physics Letters*, vol. 92, no. 4, p. 043106, 2008.

[30] J. E. Sader, "Frequency response of cantilever beams immersed in viscous fluids with applications to the atomic force microscope," *Journal of applied physics*, vol. 84, no. 1, pp. 64–76, 1998.

[31] J. E. Sader, T. P. Burg, and S. R. Manalis, "Energy dissipation in microfluidic beam resonators," 2010.

[32] M. Bao, H. Yang, H. Yin, and Y. Sun, "Energy transfer model for squeeze-film air damping in low vacuum," *Journal of Micromechanics and Microengineering*, vol. 12, no. 3, p. 341, 2002.

[33] Z. Hao, A. Erbil, and F. Ayazi, "An analytical model for support loss in micromachined beam resonators with in-plane flexural vibrations," *Sensors and Actuators A: Physical*, vol. 109, no. 1-2, pp. 156–164, 2003.

[34] A. Schroer, J. Bauer, R. Schwaiger, and O. Kraft, "Optimizing the mechanical properties of polymer resists for strong and light-weight micro-truss structures," *Extreme Mechanics Letters*, vol. 8, pp. 283–291, 2016.

[35] L. Sementilli, E. Romero, and W. P. Bowen, "Nanomechanical dissipation and strain engineering," *Advanced Functional Materials*, vol. 32, no. 3, p. 2105247, 2022.

[36] R. A. Norte, J. P. Moura, and S. Gröblacher, "Mechanical resonators for quantum optomechanics experiments at room temperature," *Physical review letters*, vol. 116, no. 14, p. 147202, 2016.

[37] L. E. Kinsler, A. R. Frey, A. B. Coppens, and J. V. Sanders, *Fundamentals of acoustics*. John wiley & sons, 2000.

[38] E. D. Lemma, F. Rizzi, T. Dattoma, B. Spagnolo, L. Sileo, A. Qualtieri, M. De Vittorio, and F. Pisanello, "Mechanical properties tunability of three-dimensional polymeric structures in two-photon lithography," *IEEE transactions on nanotechnology*, vol. 16, no. 1, pp. 23–31, 2016.

[39] "3dm tough resin," 2018. [Online]. Available: https://www.3dm-shop.com/product-page/3DM-TOUGH

[40] T. Bieling, "Tensile test 3dm tough," 2022.

[41] J. F. Shackelford and W. Alexander, *CRC materials science and engineering handbook*. CRC press, 2000.

[42] M. A. Hopcroft, W. D. Nix, and T. W. Kenny, "What is the young's modulus of silicon?" *Journal of microelectromechanical systems*, vol. 19, no. 2, pp. 229–238, 2010.

[43] T. K. Hossain, S. MacLaren, J. M. Engel, C. Liu, I. Adesida, and R. S. Okojie, "The fabrication of suspended micromechanical structures from bulk 6h-sic using an icp-rie system," *Journal of Micromechanics and Microengineering*, vol. 16, no. 4, p. 751, 2006.

[44] W. Huang and K. M. de Payrebrune, "Experimental investigation on the thermal length expansion of direct laser writing material," *PAMM*, vol. 19, no. 1, p. e201900485, 2019.

[45] M. F. Ashby, "Overview no. 80: On the engineering properties of materials," *Acta metallurgica*, vol. 37, no. 5, pp. 1273–1293, 1989.

[46] N. Rohbeck, R. Ramachandramoorthy, D. Casari, P. Schürch, T. E. Edwards, L. Schilinsky, L. Philippe, J. Schwiedrzik, and J. Michler, "Effect of high strain rates and temperature on the micromechanical properties of 3d-printed polymer structures made by two-photon lithography," *Materials & Design*, vol. 195, p. 108977, 2020.

[47] M. Babaei, S. Kim, C. Velez, D. K. Patel, and S. Bergbreiter, "Increasing the energy efficiency of niti unimorph actuators with a 3d-printed passive layer," *Journal of Microelectromechanical Systems*, vol. 29, no. 5, pp. 797–803, 2020.

[48] S. S. Verbridge, J. M. Parpia, R. B. Reichenbach, L. M. Bellan, and H. G. Craighead, "High quality factor resonance at room temperature with nanostrings under high tensile stress," *Journal of Applied Physics*, vol. 99, no. 12, p. 124304, 2006.

[49] S. Schmid, K. Jensen, K. Nielsen, and A. Boisen, "Damping mechanisms in high-q micro and nanomechanical string resonators," *Physical Review B*, vol. 84, no. 16, p. 165307, 2011.

[50] R. A. Minamisawa, M. J. Süess, R. Spolenak, J. Faist, C. David, J. Gobrecht, K. K. Bourdelle, and H. Sigg, "Top-down fabricated silicon nanowires under tensile elastic strain up to 4.5%," *Nature communications*, vol. 3, no. 1, pp. 1–6, 2012.
[51] A. H. Ghadimi, S. A. Fedorov, N. J. Engelsen, M. J. Bereyhi, R. Schilling, D. J. Wilson, and T. J. Kippenberg, "Elastic strain engineering for ultralow mechanical dissipation," *Science*, vol. 360, no. 6390, pp. 764–768, 2018.
[52] R. C. Hibbeler, *Mechanics of materials*. Pearson Educación, 2005.
[53] T. Braun, V. Barwich, M. K. Ghatkesar, A. H. Bredekamp, C. Gerber, M. Hegner, and H. P. Lang, "Micromechanical mass sensors for biomolecular detection in a physiological environment," *Physical Review E*, vol. 72, no. 3, p. 031907, 2005.
[54] "Ip-s tables." [Online]. Available: https://support.nanoscribe.com/hc/en-gb/articles/360009156133-IP-S-Tables
[55] D. H. Zanette, "Energy exchange between coupled mechanical oscillators: linear regimes," *Journal of Physics Communications*, vol. 2, no. 9, p. 095015, 2018.
[56] M. H. de Jong, M. A. t. Wolde, A. Cupertino, P. G. Steeneken, and R. A. Norte, "Mechanical dissipation by substrate-mode coupling in sin resonators," *arXiv preprint arXiv:2206.00990*, 2022.
[57] C. Carrasco, P. Ares, P. De Pablo, and J. Gómez-Herrero, "Cutting down the forest of peaks in acoustic dynamic atomic force microscopy in liquid," *Review of Scientific Instruments*, vol. 79, no. 12, p. 126106, 2008.
[58] J. Kokavecz and A. Mechler, "Investigation of fluid cell resonances in intermittent contact mode atomic force microscopy," *Applied physics letters*, vol. 91, no. 2, p. 023113, 2007.
[59] R. J. Young and P. A. Lovell, *Introduction to polymers*. CRC press, 2011.
[60] R. Legtenberg, H. A. Tilmans, J. Elders, and M. Elwenspoek, "Stiction of surface micromachined structures after rinsing and drying: model and investigation of adhesion mechanisms," *Sensors and actuators A: Physical*, vol. 43, no. 1-3, pp. 230–238, 1994.
[61] C. L. Lewis, C. C. Craig, and A. G. Senecal, "Mass and density measurements of live and dead gram-negative and gram-positive bacterial populations," *Applied and environmental microbiology*, vol. 80, no. 12, pp. 3622–3631, 2014.
[62] N. Cermak, S. Olcum, F. F. Delgado, S. C. Wasserman, K. R. Payer, M. A Murakami, S. M. Knudsen, R. J. Kimmerling, M. M. Stevens, Y. Kikuchi *et al.*, "High-throughput measurement of single-cell growth rates using serial microfluidic mass sensor arrays," *Nature biotechnology*, vol. 34, no. 10, pp. 1052–1059, 2016.
[63] J. Lee, R. Chunara, W. Shen, K. Payer, K. Babcock, T. Burg, and S. Manalis, "Suspended microchannel resonators with piezoresistive sensors," *Lab on a Chip*, vol. 11, no. 4, pp. 645–651, 2011.
[64] S. Stassi, I. Cooperstein, M. Tortello, C. F. Pirri, S. Magdassi, and C. Ricciardi, "Reaching silicon-based nems performances with 3d printed nanomechanical resonators," *Nature Communications*, vol. 12, no. 1, pp. 1–9, 2021.
[65] X. Wen, B. Zhang, W. Wang, F. Ye, S. Yue, H. Guo, G. Gao, Y. Zhao, Q. Fang, C. Nguyen *et al.*, "3d-printed silica with nanoscale resolution," *Nature Materials*, vol. 20, no. 11, pp. 1506–1511, 2021.
[66] P. van Altena, "Multiscale 3d printed polymer probes for single cell experiments: A rapid prototyping method to fabricate microfluidic atomic force microscopy cantilevers for single cell studies," 2021.
[67] M. Blankespoor, "Liquid dosing on the micro-scale: A quest for increased resolution," 2022.
[68] M. Gagino, G. Katsikis, S. Olcum, L. Virot, M. Cochet, A. Thuaire, S. R. Manalis, and V. Agache, "Suspended nanochannel resonator arrays with piezoresistive sensors for high-throughput weighing of nanoparticles in solution," *ACS sensors*, vol. 5, no. 4, pp. 1230–1238, 2020.
[69] L. Yang, F. Mayer, U. H. Bunz, E. Blasco, and M. Wegener, "Multi-material multi-photon 3d laser micro-and nanoprinting," *Light: Advanced Manufacturing*, vol. 2, no. 3, pp. 296–312, 2021.

# Conclusion

The goal of this research was to find the smallest mass resolution of a 3D printed suspended microchannel resonator (SMR) designed for buoyant mass sensing of E. Coli bacteria ($175\ fg$ in water). This was realized by focusing the research on fundamentally understanding and characterizing the damping sources of 3D printed polymer microbeam resonators. Followed by maximizing their quality factor, consequently improving mass resolution and finally fabricating an optimized prototype SMR with multi-scale 3D printing accordingly.
Firstly, the dominant damping source of 3D printed polymer microbeam resonators was identified by eliminating damping sources based on experimental results from characterization and their theoretical dependencies. Characterization was performed across a range of microbeam resonator variations to systematically map the damping behavior of the 3D printed polymer named IP-S. It was concluded that bulk friction damping was the dominant damping source for all devices, but it showed a strong dependency on resonance frequency. The least damping was measured above a resonance frequency of $200\ KHz$ with record-breaking quality factors up to $1000$.
Secondly, design considerations and potential methods of improving the quality factor were investigated experimentally. Results showed that thermal post-development treatment did not change the quality factor of resonators significantly, but it had increased Young's modulus of the material by a factor of 1.5 and also shrank the material substantially. This effect was later incorporated to enhance the quality factor of one specific device design to $1819$, by creating a tensile stress in the narrowed bridge structures. Furthermore, the influence of substrate acoustic impedance on the quality factor of microbeam resonators was studied, concluding that a small acoustic impedance mismatch between the materials of the resonator and substrate could degrade the quality factor significantly.
In order to answer the research question, prototypes of the SMR were optimized for the smallest mass resolution within the limitations of our fabrication and measurement facilities, by minimizing device mass and maximizing resonance frequency therefore also quality factor. Their mass resolution was estimated to be at least $60\ fg$, which is sensitive enough to detect E. Coli bacteria and compete with conventional fabricated SMRs. Finally, prototypes of the SMR were fabricated with multi-scale 3D printing creating a plug–and–play connection to fluidics and measurement equipment. Unfortunately due to temporal limitations, we were unable to demonstrate the mass sensing capabilities of the prototypes as proposed in the literature survey. It is recommended for future work to demonstrate the biosensing capabilities of the 3D printed SMR by performing actual buoyant mass sensing experiments with cells. Single-cell analysis with multi-scale 3D printed devices could also be advanced by combining the SMR for mass sensing with 3D printed pipetting systems.

Systematically mapping the damping behavior of the IP-S microbeam resonators laid a foundation for future applications of 3D printed polymer resonators, considering the damping behavior of this material was previously unknown. A drawback of this experimental approach to damping quantification is that the theoretical models could not be fitted with experimental data, because the models were highly dependent on uncertain and unknown material properties. It is recommended to quantify thermal and mechanical material properties before further studying damping behavior depending on those properties. Additionally, it is recommended to study the effect of temperature on the quality factor of polymer resonators as bulk friction damping varies with temperature.
The theoretical mass resolution of the devices in this work showed that polymer SMRs would be able to compete with conventional SMRs (typically made of silicon-based materials) or even have an advantage over them when working in lower quality factor ($Q < 1000$) conditions. This advantage resulted from the significantly lower mass density of IP-S compared to Silicon-based materials. When working towards the smallest mass resolution, it is recommended to not only focus on improving the quality factor, but also minimize the effective mass of the resonating structure. Further mass resolution improvements for our devices could be accomplished by breaching fabrication limits, upgrading measurement equipment, changing device material, improving the incorporation of strain engineering and performing higher resonant mode operation.

This work showcased that multi-scale 3D printing is a fabrication method for SMRs capable of rapid prototyping and incorporating fluidic connections among different scales easily. In addition, 2PP showed to be a good method of fabrication for resonant microstructures with a high level of design freedom. This fabrication method still remains limited in material options, however, recent developments showed that even Silicon Dioxide and other ceramic structures could be fabricated. This pushes 3D printed beam resonators towards the low-damping capabilities of lithography-based fabricated devices with additional design freedom. Opening up promising possibilities for future low-damping resonator applications. The key advantage of multi-scale 3D printed SMRs is the flexible and accessible end-to-end fabrication, yielding rapid prototypes of plug-and-play devices. Characterizing 3D printed polymer microbeam resonators, maximizing their quality factor and determining their theoretical mass resolution paved the path towards actual biosensing 3D printed SMRs with the capabilities of lithography-based fabricated devices but with additional design and fabrication flexibility.

# Part III

# Appendices

## A.1. Introduction

This appendix contains a step-by-step fabrication protocol for the fabrication of a suspended microchannel resonator (SMR) mounted on top of a plug-and-play fluidic interface. Both are 3D printed polymer structures but they were fabricated with separate fabrication techniques: Digital Light Processing (DLP) for the fluidic interface and two-photon polymerization (2PP) for the SMR. A fabrication process flowchart is given in Figure A.1 followed by an in-depth step-by-step visual guide in the next sections. The 2PP printing program code is given in the last section.

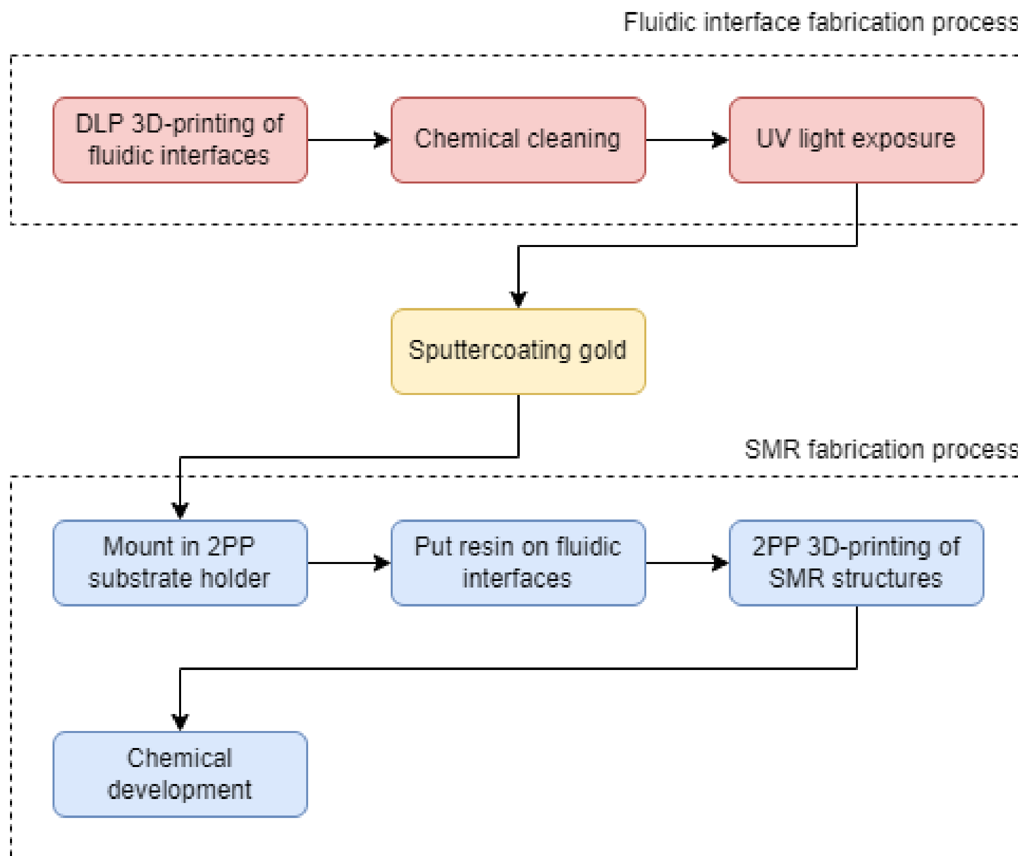


Figure A.1: Fabrication process flowchart for the SMR mounted on top of a plug-and-play fluidic interface.

## A.2. Fluidic interface fabrication

Fluidic interfaces were fabricated with the DLP 3D-printing process using the Micro Plus Hi-Res (EnvisionTEC US LLC, United States). 3DM TOUGH clear resin was used with the HTM-140v2 material license. The printed structure will consist of 8 fluidic interfaces and a $25mm$ by $25mm$ disposable adapter for the Nanoscribe substrate holder.

### Step 1: Generate printing file

Import the design .STL file in the Perfactory (Envisiontec) software, select $35\mu m$ layer height settings of HTM-140v2 material, add $1.5mm$ z-distance between structure and build plate and add ”small” support structures.

### Step 2: DLP Print

Poor approximately $75ml$ of the 3DM TOUGH clear resin in the printing tray, perform ”move” and ”home” of the build plate and start the print job.

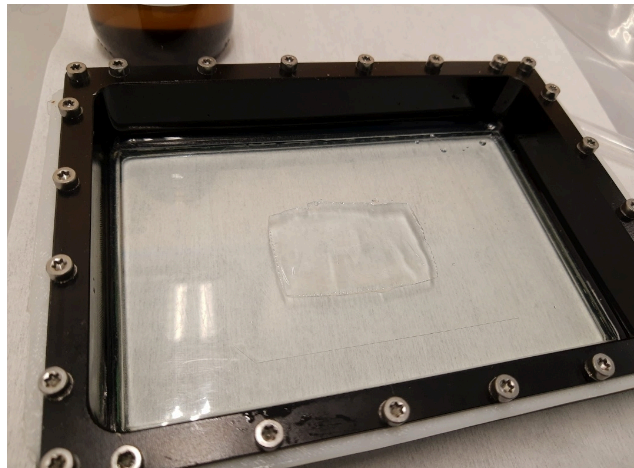

Figure A.2: Printing tray filled with resin.

Figure A.3: Envisiontec control menu.

## Step 3: Chemical cleaning

Remove printed structure from the build plate with a knife or razor blade, submerge the structure in a beaker with IPA ($99.8\%$ 2-Propanol) and place the beaker in an ultrasonic bath (Sonorex Super RK31) for 5 minutes. Repeat with clean IPA.

## Step 4: UV light exposure

Blow dry fluidic channels of the interfaces carefully and expose the structure to 6 minutes of ultraviolet light ($320to550nm$) with the PHOTOPOL light (Dentalfarm SRL, Italy).

## Step 5: Remove printing supports

Remove the supporting structures of the adapter using a putty knife or other knife and blow off any polymer debris.

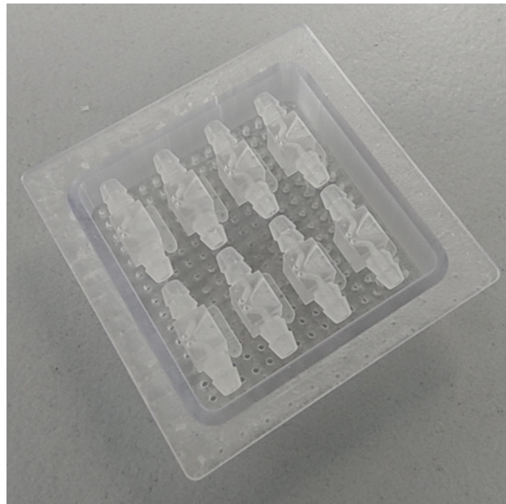

Figure A.4: 2PP adapter with 8 fluidic interfaces.

## A.3. Sputtercoating gold

Sputtercoating gold provides the fluidic interfaces with a reflective layer needed to find the surface of the substrate (z-coordinate), also called the "interface" necessary for 2PP printing. This is to focus the laser on the correct printing height to be able to print structures on top of the substrate and not inside or flying off the substrate. Sputtercoating is performed with the JFC-1300 Sputtercoater (JEOL Ltd., Japan).

### Step 6: Sputtercoating gold

Place the 3D printed adapter with the interfaces facing up in the center of the sputtercoater. Coat for 10 seconds on $10mA$ to get approximately $2nm$ of gold.

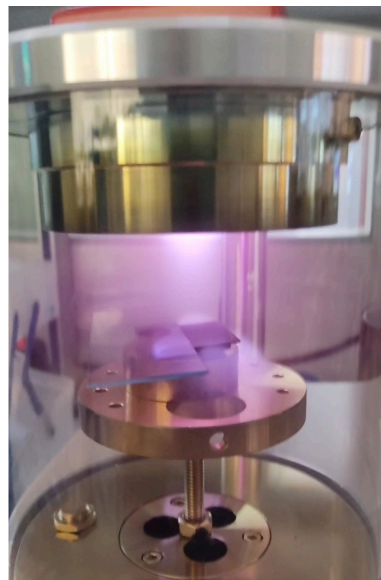

Figure A.5: Sputtercoating gold.

## A.4. Suspended microchannel resonator fabrication

Suspended microchannel resonators were fabricated with the 2PP 3D-printing technique using the Professional GT (Nanoscribe GmbH & Co. KG, Germany). The 25x NA 0.8 lens (Carl Zeiss AG, Germany) was used in combination with IP-S resin (Nanoscribe GmbH & Co. KG, Germany). Unconventional polymer substrates (consisting of 8 fluidic interfaces in a disposable adapter) were used to directly fabricate the microscale SMR's connected to macroscale fluidic interfaces. The connection between IP-S and 3DM TOUGH clear is the most challenging part of fabrication. Variations in UV light

exposure of 3DM tough clear, gold sputtering, 2PP printing dosage and 2PP printing depth (inside the substrate) could cause improper adhesion and leakages.

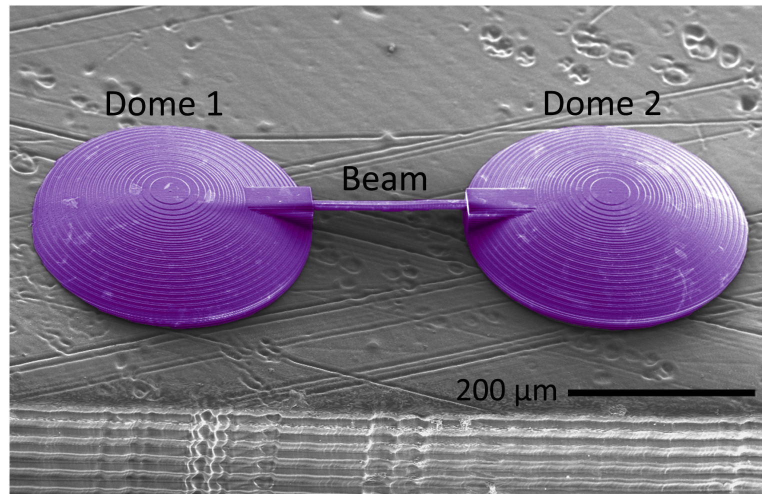


Figure A.6: SMR with named parts: ”Dome 1”, ”Beam” and ”Dome 2”.

## Step 7: Generate printing file

Import the SMR design as separate .STL files for the fluid connecting ”domes” and resonant ”beam” in the DeScribe (Nanoscribe) software, select ”IP-S 25x ITO Solid(3D MF)” and keep standard settings for the ”dome”.

The .STL files of the resonant ”beam” should be imported with adjusted standard settings: In the ”Hatching” tab change the contour to $0$ and the hatching angle such that the lines are along the beam length.

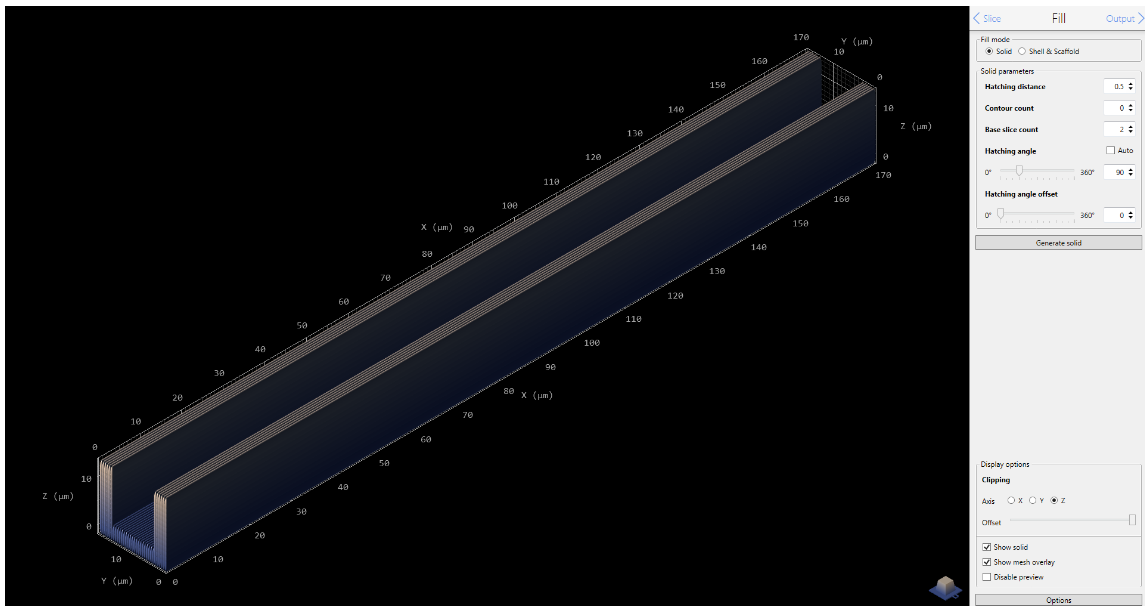


Figure A.7: Adjusted setting in ”Hatching” tab.

In the ”Output tab” change the splitting mode to rectangular and block size to $4\mu m$ in direction of the length of the beam. Block shear angle to $0\,\mathrm{deg}$, block overlap to $2\mu m$, check boxes of avoid flying blocks, group neighboring blocks and backlash correction.

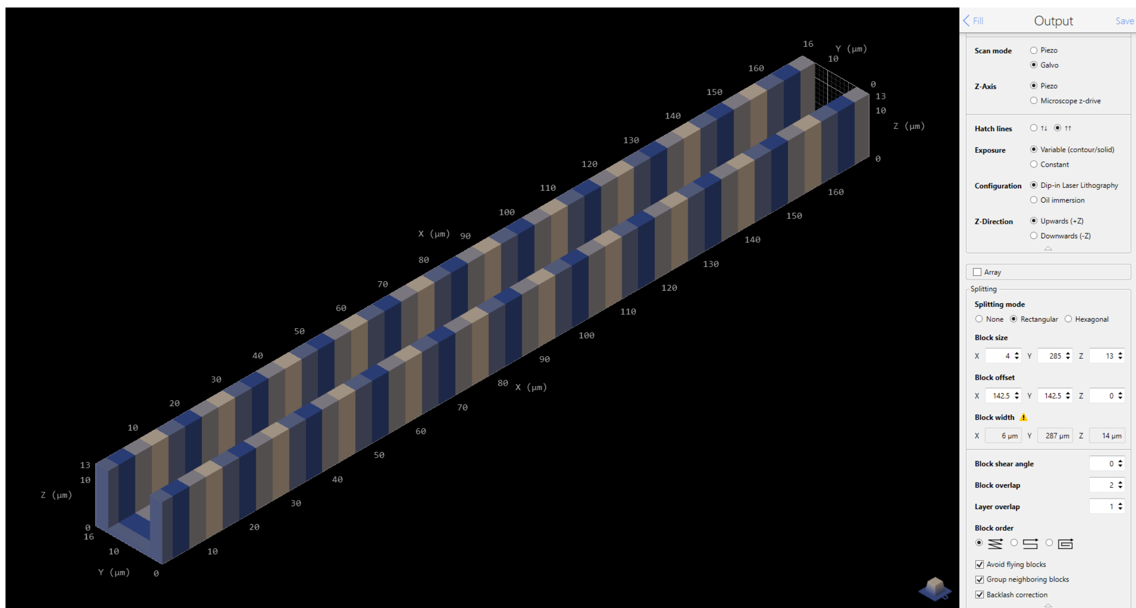


Figure A.8: Adjusted setting in ”Output” tab.

Remove all ”FindInterface” commands from ”data” files of the beam and the domes to be printed (to keep the whole structure on the same relative z-coordinate)

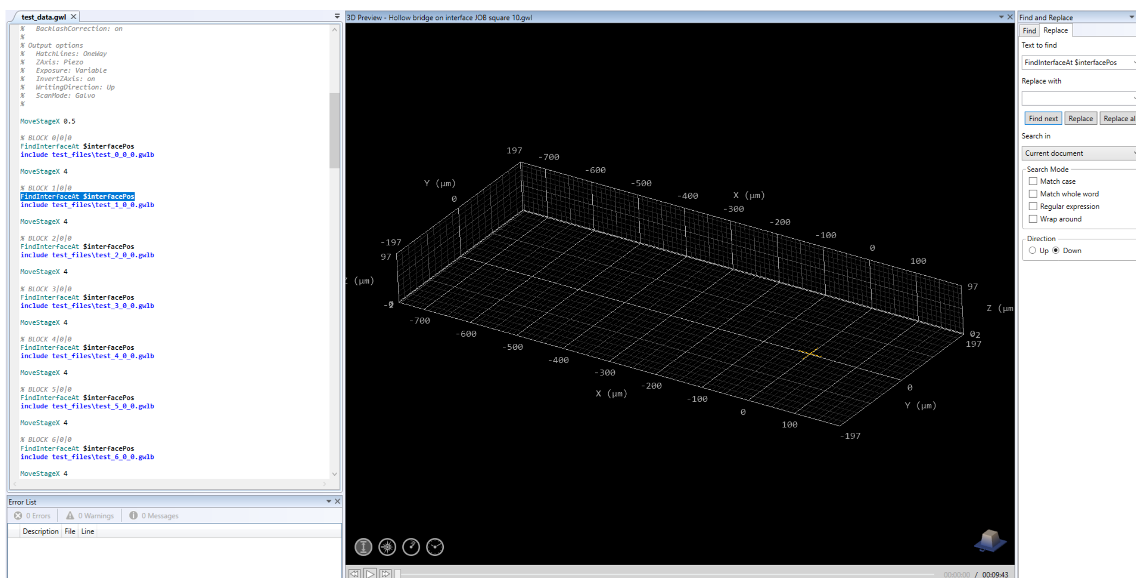


Figure A.9: Removing ”FindInterface” commands.

Create a ”job” file for the assembly of the SMR comprising of two domes and a single beam and program printing in this order. To create a connected SMR assembly try to adjust XYZ spacing between parts with the following commands: ”MoveStageX””MoveStageY””AddZDrivePosition”.

Change dosage for domes to $solidLaserPower = 85$ $solidScanSpeed = 100000$ and printing into substrate depth to ”interfacepos=2.0” or a different sufficient depth. Change dosage for the beam back to the standard $solidLaserPower = 100$ $solidScanSpeed = 100000$.

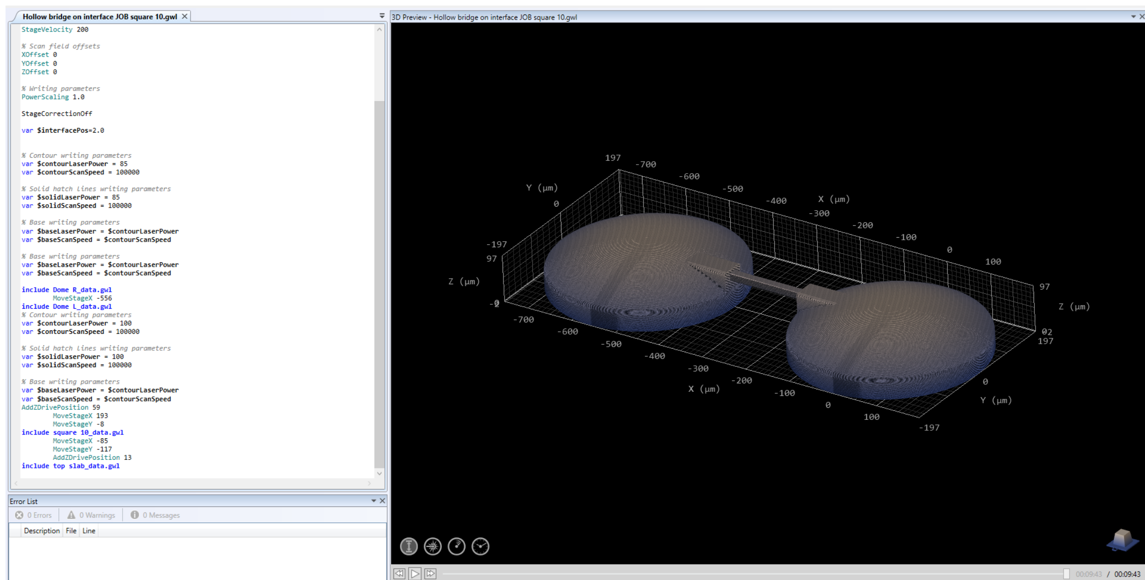


Figure A.10: Programming assembly code.

## Step 8: Mount in substrate holder

Place the 3D printed adapter with the interfaces facing up in the 2PP substrate holder, center position (number 5) of the 9 square substrate positions. Tape the adapter to the substrate holder in order to secure it.

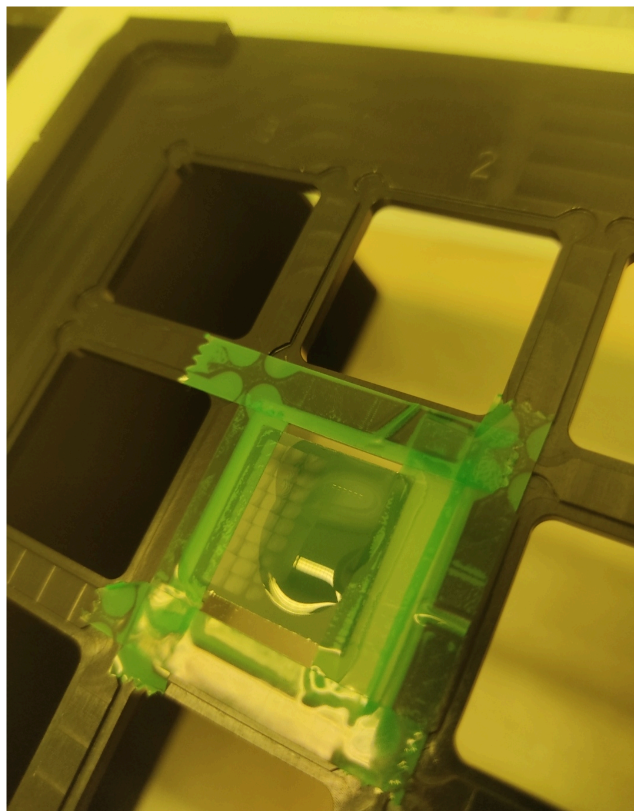

Figure A.11: Mounted substrate fixed with tape in 2PP substrate holder.

## Step 9: Put resin on fluidic interfaces

Put the IP-S resin droplet for droplet onto the fluidic interface without scraping the surface and prepare the Nanoscribe for printing. (Putting a droplet of resin onto the lens could help improve finding the ”interface”, but must be performed with the highest care.)

## Step 10: Find the surface of the fluidic interface

**WARNING: The lens could crash into the fluidic interfaces when this step is not performed correctly or when automatic ”interface” finding is performed. This step should always be performed in the presence of an experienced Nanoscribe user.** Moved the lens down to about $10mm$ in the Z-direction. Move the XY stage to the approximate coordinates of the holes from the fluidic channels. The lens should not have touched the resin on the fluidic interfaces yet.

Move around slowly with the XY stage to about $2000\mu m$ in each direction. Now notice the increase and decrease in light on the screen and in the graphs. (This is reflected light by the fluidic interface and not reflected light when the lens is above a gap between fluidic interfaces.)

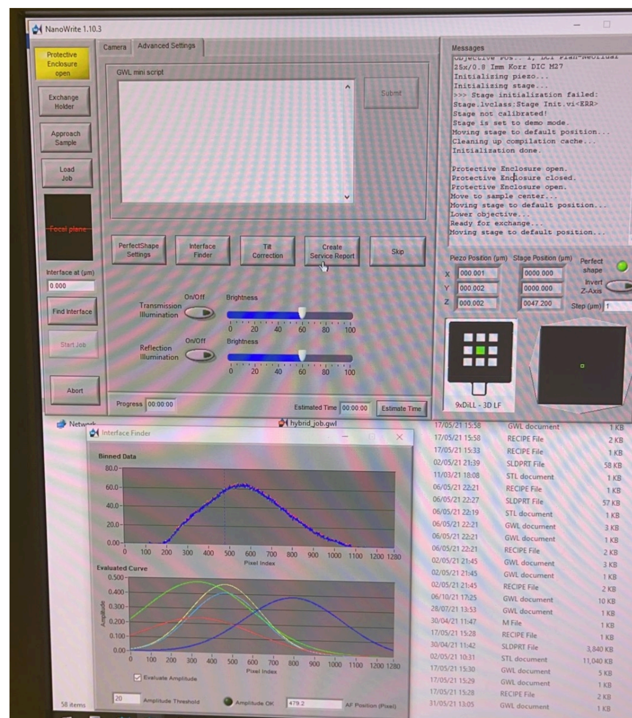


Figure A.12: The graphs at the bottom of the control screen indicate reflected light.

Move the XY stage to the area with the most reflected light and start moving down the lens in the Z-direction **very slowly**. You will first notice the lens touching the resin, very abruptly shifting the light. When you continue you will see the surface (”interface”) of the fluidic interface getting into focus.

Figure A.13: Surface of the fluidic interface in focus.

Move the XY stage to find the fluidic channel holes and align the center with the center of the left hole. Press automatic ”interface” finding. (To find the center of the lens on the screen you could turn on the laser manually and turn it off again.)

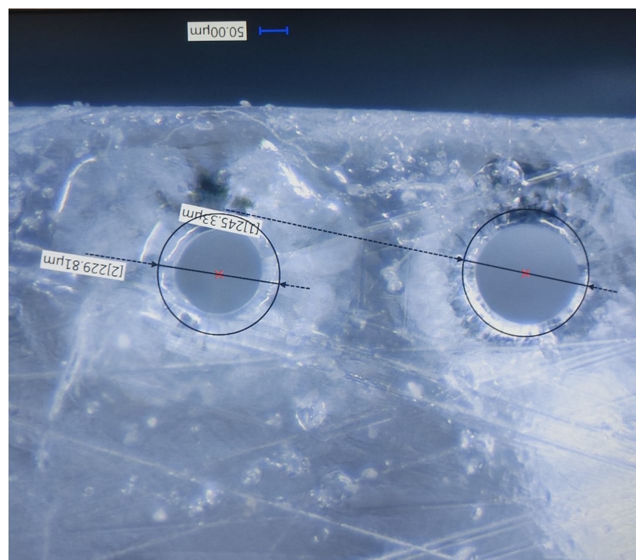


Figure A.14: The fluidic channel holes.

## Step 11: Start printing

Load your assembly job and start printing. It should take about 10 minutes for a single SMR.

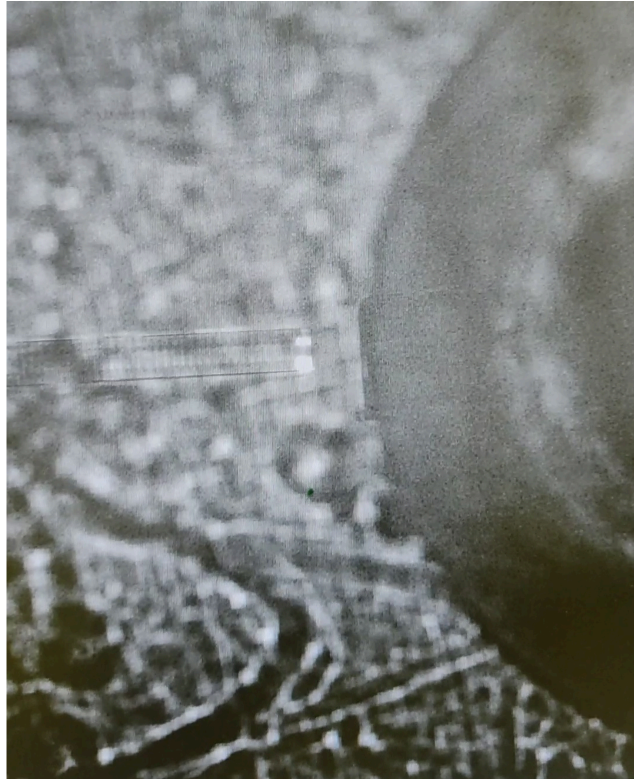

Figure A.15: Nearly finished SMR during printing.

## Step 12: Chemical development

Submerge the structures for 25 minutes in $\geq 99.5\%$ Propylene glycol monomethyl ether acetate (MilliporeSigma, United States) followed by 30 seconds of submersion in Methoxy-nonafluorobutane known as Novec 7100 engineering fluid (MilliporeSigma, United states).

## Step 13: Remove devices from adapter

Carefully remove devices from the adapter with tweezers.

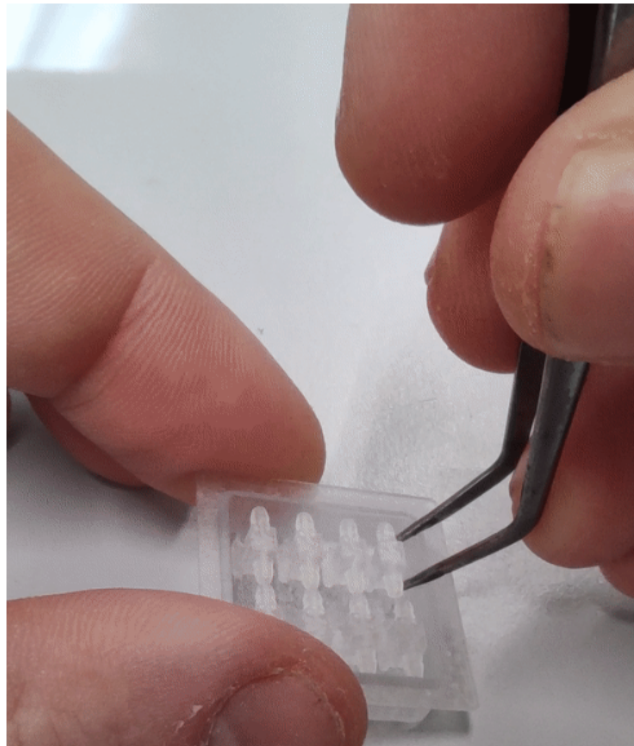

Figure A.16: Removing devices from adapter with tweezers.

### Step 14: Flush fluidic channels

Fluidic channels should be flushed additionally with Novec using a manual syringe connected with tubing to the fluidic interface.

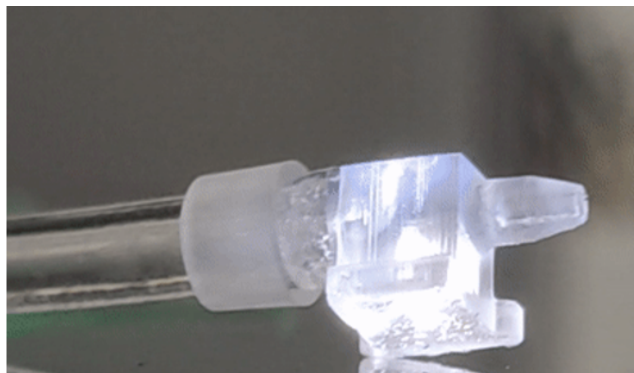

Figure A.17: Flushing device with connected tube.

## A.5. 2PP printing code

### SMR assembly job file

```
% File generated by DeScribe 2.5.5

% System initialization
InvertZAxis 1

% Writing configuration
GalvoScanMode
ContinuousMode
PiezoSettlingTime 10
GalvoAcceleration 10
StageVelocity 200
```

```
12
13 % Scan field offsets
14 XOffset 0
15 YOffset 0
16 ZOffset 0
17
18 % Writing parameters
19 PowerScaling 1.0
20
21 StageCorrectionOff
22
23 var $interfacePos=2.0
24
25
26 % Contour writing parameters
27 var $contourLaserPower = 85
28 var $contourScanSpeed = 100000
29
30 % Solid hatch lines writing parameters
31 var $solidLaserPower = 85
32 var $solidScanSpeed = 100000
33
34 % Base writing parameters
35 var $baseLaserPower = $contourLaserPower
36 var $baseScanSpeed = $contourScanSpeed
37
38 % Base writing parameters
39 var $baseLaserPower = $contourLaserPower
40 var $baseScanSpeed = $contourScanSpeed
41
42 include Dome R_data.gwl  %Dome 1
43     MoveStageX -556
44 include Dome L_data.gwl   %Dome 2
45 % Contour writing parameters
46 var $contourLaserPower = 100
47 var $contourScanSpeed = 100000
48
49 % Solid hatch lines writing parameters
50 var $solidLaserPower = 100
51 var $solidScanSpeed = 100000
52
53 % Base writing parameters
54 var $baseLaserPower = $contourLaserPower
55 var $baseScanSpeed = $contourScanSpeed
56 AddZDrivePosition 59
57     MoveStageX 193
58     MoveStageY -8
59 include square 10_data.gwl %Beam 1
60     MoveStageX -85
61     MoveStageY -117
62     AddZDrivePosition 13
63 include top slab_data.gwl %Beam 2
```

## Dome 1 data file

```
1  % File generated by DeScribe 2.5.5
2  %
3  % Creation time
4  %   2022-05-03T09:32:06+02:00
5  %
6  % Source file
7  %   Type: Mesh
8  %   Path: D:\Jikke\Google Drive\School\Master Mechanical Engineering\Jaar 3 Afstuderen\2020-Jikke-
       MassSensingPolymerProbes\Fabrication\Nanoscribe\22-05-03 Hollow bridge on interface square
       channel 10 mu L170\Dome v6 hollow bridge connection square channel 10 mu.STL
9  %
10 % Volume
11 %   0.00515 mm³
12 %
13 % Bounding box
```

```
%   Minimum X: -197.5 Y: -197.496 Z: 0
%   Maximum X: 197.5 Y: 197.496 Z: 95
%
% Transformation
%   Scaling X: 1 Y: 1 Z: 1
%   Rotation X: 0.5 Y: -0.5 Z: -0.5 W: 0.5
%   Translation X: 197.5 Y: 197.5 Z: -0.5
%
% Slicing
%   SlicingMode: Fixed
%   Distance: 1
%   SimplificationTolerance: 0.01
%   FixSelfIntersections: on
%
% Hatching
%   HatchingDistance: 0.5
%   HatchingAngle: 90
%   HatchingAngleOffset: 0
%
% Output options
%   HatchLines: OneWay
%   ZAxis: Piezo
%   Exposure: Variable
%   InvertZAxis: on
%   WritingDirection: Up
%   ScanMode: Galvo
%

% BLOCK 0|0|0
include Dome R_files\Dome R_0_0_0.gwlb
```

## Dome 2 data file

```
% File generated by DeScribe 2.5.5
%
% Creation time
%   2022-05-03T09:45:19+02:00
%
% Source file
%   Type: Mesh
%   Path: D:\Jikke\Google Drive\School\Master Mechanical Engineering\Jaar 3 Afstuderen\2020-Jikke-
    MassSensingPolymerProbes\Fabrication\Nanoscribe\22-05-03 Hollow bridge on interface square
    channel 10 mu L170\Dome v6 hollow bridge connection square channel 10 mu.STL
%
% Volume
%   0.00515 mm³
%
% Bounding box
%   Minimum X: -197.5 Y: -197.496 Z: 0
%   Maximum X: 197.5 Y: 197.496 Z: 95
%
% Transformation
%   Scaling X: 1 Y: 1 Z: 1
%   Rotation X: 0.5 Y: 0.5 Z: 0.5 W: 0.5
%   Translation X: -197.5 Y: -197.5 Z: -0.5
%
% Slicing
%   SlicingMode: Fixed
%   Distance: 1
%   SimplificationTolerance: 0.01
%   FixSelfIntersections: on
%
% Hatching
%   HatchingDistance: 0.5
%   HatchingAngle: 90
%   HatchingAngleOffset: 0
%
% Output options
%   HatchLines: OneWay
%   ZAxis: Piezo
```

```
36 %   Exposure: Variable
37 %   InvertZAxis: on
38 %   WritingDirection: Up
39 %   ScanMode: Galvo
40 %
41
42
43 % BLOCK 0|0|0
44 include Dome L_files\Dome L_0_0_0.gwlb
```

## Beam part 1 data file

```
1 % File generated by DeScribe 2.5.5
2 %
3 % Creation time
4 %   2022-05-03T09:38:17+02:00
5 %
6 % Source file
7 %   Type: Mesh
8 %   Path: D:\Jikke\Google Drive\School\Master Mechanical Engineering\Jaar 3 Afstuderen\2020-Jikke-
    MassSensingPolymerProbes\Fabrication\Nanoscribe\22-05-03 Hollow bridge on interface square
    channel 10 mu L170\Bridge square channel 16,14,10,10 u shape.STL
9 %
10 % Volume
11 %   1.5×10^-5 mm³
12 %
13 % Bounding box
14 %   Minimum X: 0 Y: 0 Z: 0
15 %   Maximum X: 170 Y: 16 Z: 12
16 %
17 % Transformation
18 %   Scaling X: 1.7 Y: 1 Z: 1
19 %   Rotation X: 0.5 Y: -0.5 Z: -0.5 W: 0.5
20 %   Translation X: 170 Y: 16 Z: 0
21 %
22 % Slicing
23 %   SlicingMode: Fixed
24 %   Distance: 1
25 %   SimplificationTolerance: 0.01
26 %   FixSelfIntersections: on
27 %
28 % Hatching
29 %   HatchingDistance: 0.5
30 %   HatchingAngle: 90
31 %   HatchingAngleOffset: 0
32 %
33 % Splitting
34 %   Mode: Rectangular
35 %   BlockSize X: 4 Y: 250 Z: 20
36 %   Offset X: 0 Y: 0 Z: 0
37 %   Shear: 0
38 %   Overlap: XY: 2 Z: 0
39 %   BlockWidth X: 6 Y: 252 Z: 20
40 %   BlockOrder: Lexical
41 %   AvoidFlyingBlocks: on
42 %   GroupBlocks: off
43 %   BacklashCorrection: on
44 %
45 % Output options
46 %   HatchLines: OneWay
47 %   ZAxis: Piezo
48 %   Exposure: Variable
49 %   InvertZAxis: on
50 %   WritingDirection: Up
51 %   ScanMode: Galvo
52 %
53
54 MoveStageY 125
55 MoveStageX 2
56
```

```
57 % BLOCK 0|0|0
58
59 include square 10_files\square 10_0_0_0.gwlb
60
61 MoveStageX 4
62
63 % BLOCK 1|0|0
64
65 include square 10_files\square 10_1_0_0.gwlb
66
67 MoveStageX 4
68
69 % BLOCK 2|0|0
70
71 include square 10_files\square 10_2_0_0.gwlb
72
73 MoveStageX 4
74
75 % BLOCK 3|0|0
76
77 include square 10_files\square 10_3_0_0.gwlb
78
79 MoveStageX 4
80
81 % BLOCK 4|0|0
82
83 include square 10_files\square 10_4_0_0.gwlb
84
85 MoveStageX 4
86
87 % BLOCK 5|0|0
88
89 include square 10_files\square 10_5_0_0.gwlb
90
91 MoveStageX 4
92
93 % BLOCK 6|0|0
94
95 include square 10_files\square 10_6_0_0.gwlb
96
97 MoveStageX 4
98
99 % BLOCK 7|0|0
100
101 include square 10_files\square 10_7_0_0.gwlb
102
103 MoveStageX 4
104
105 % BLOCK 8|0|0
106
107 include square 10_files\square 10_8_0_0.gwlb
108
109 MoveStageX 4
110
111 % BLOCK 9|0|0
112
113 include square 10_files\square 10_9_0_0.gwlb
114
115 MoveStageX 4
116
117 % BLOCK 10|0|0
118
119 include square 10_files\square 10_10_0_0.gwlb
120
121 MoveStageX 4
122
123 % BLOCK 11|0|0
124
125 include square 10_files\square 10_11_0_0.gwlb
126
127 MoveStageX 4
```

```
128
129 % BLOCK 12|0|0
130
131 include square 10_files\square 10_12_0_0.gwlb
132
133 MoveStageX 4
134
135 % BLOCK 13|0|0
136
137 include square 10_files\square 10_13_0_0.gwlb
138
139 MoveStageX 4
140
141 % BLOCK 14|0|0
142
143 include square 10_files\square 10_14_0_0.gwlb
144
145 MoveStageX 4
146
147 % BLOCK 15|0|0
148
149 include square 10_files\square 10_15_0_0.gwlb
150
151 MoveStageX 4
152
153 % BLOCK 16|0|0
154
155 include square 10_files\square 10_16_0_0.gwlb
156
157 MoveStageX 4
158
159 % BLOCK 17|0|0
160
161 include square 10_files\square 10_17_0_0.gwlb
162
163 MoveStageX 4
164
165 % BLOCK 18|0|0
166
167 include square 10_files\square 10_18_0_0.gwlb
168
169 MoveStageX 4
170
171 % BLOCK 19|0|0
172
173 include square 10_files\square 10_19_0_0.gwlb
174
175 MoveStageX 4
176
177 % BLOCK 20|0|0
178
179 include square 10_files\square 10_20_0_0.gwlb
180
181 MoveStageX 4
182
183 % BLOCK 21|0|0
184
185 include square 10_files\square 10_21_0_0.gwlb
186
187 MoveStageX 4
188
189 % BLOCK 22|0|0
190
191 include square 10_files\square 10_22_0_0.gwlb
192
193 MoveStageX 4
194
195 % BLOCK 23|0|0
196
197 include square 10_files\square 10_23_0_0.gwlb
198
```

```
MoveStageX 4

% BLOCK 24|0|0

include square 10_files\square 10_24_0_0.gwlb

MoveStageX 4

% BLOCK 25|0|0

include square 10_files\square 10_25_0_0.gwlb

MoveStageX 4

% BLOCK 26|0|0

include square 10_files\square 10_26_0_0.gwlb

MoveStageX 4

% BLOCK 27|0|0

include square 10_files\square 10_27_0_0.gwlb

MoveStageX 4

% BLOCK 28|0|0

include square 10_files\square 10_28_0_0.gwlb

MoveStageX 4

% BLOCK 29|0|0

include square 10_files\square 10_29_0_0.gwlb

MoveStageX 4

% BLOCK 30|0|0

include square 10_files\square 10_30_0_0.gwlb

MoveStageX 4

% BLOCK 31|0|0

include square 10_files\square 10_31_0_0.gwlb

MoveStageX 4

% BLOCK 32|0|0

include square 10_files\square 10_32_0_0.gwlb

MoveStageX 4

% BLOCK 33|0|0

include square 10_files\square 10_33_0_0.gwlb

MoveStageX 4

% BLOCK 34|0|0

include square 10_files\square 10_34_0_0.gwlb

MoveStageX 4

% BLOCK 35|0|0

include square 10_files\square 10_35_0_0.gwlb
```

```
270
271 MoveStageX 4
272
273 % BLOCK 36|0|0
274
275 include square 10_files\square 10_36_0_0.gwlb
276
277 MoveStageX 4
278
279 % BLOCK 37|0|0
280
281 include square 10_files\square 10_37_0_0.gwlb
282
283 MoveStageX 4
284
285 % BLOCK 38|0|0
286
287 include square 10_files\square 10_38_0_0.gwlb
288
289 MoveStageX 4
290
291 % BLOCK 39|0|0
292
293 include square 10_files\square 10_39_0_0.gwlb
294
295 MoveStageX 4
296
297 % BLOCK 40|0|0
298
299 include square 10_files\square 10_40_0_0.gwlb
300
301 MoveStageX 4
302
303 % BLOCK 41|0|0
304
305 include square 10_files\square 10_41_0_0.gwlb
306
307 MoveStageX 4
308
309 % BLOCK 42|0|0
310
311 include square 10_files\square 10_42_0_0.gwlb
```

## Beam part 2 data file

```
1 % File generated by DeScribe 2.5.5
2 %
3 % Creation time
4 %   2022-05-03T09:40:25+02:00
5 %
6 % Source file
7 %   Type: Mesh
8 %   Path: D:\Jikke\Google Drive\School\Master Mechanical Engineering\Jaar 3 Afstuderen\2020-Jikke-
    MassSensingPolymerProbes\Fabrication\Nanoscribe\22-05-03 Hollow bridge on interface square
    channel 10 mu L170\Hollow bridge v2 top slab L215W12H2.STL
9 %
10 % Volume
11 %   2.18×10^-6 mm³
12 %
13 % Bounding box
14 %   Minimum X: 0 Y: 0 Z: 0
15 %   Maximum X: 170 Y: 16 Z: 0
16 %
17 % Transformation
18 %   Scaling X: 0.791 Y: 1.333 Z: 0.4
19 %   Rotation X: 0 Y: 0 Z: 0 W: 1
20 %   Translation X: 0 Y: 0 Z: 0
21 %
22 % Slicing
23 %   SlicingMode: Fixed
```

```
%   Distance: 1
%   SimplificationTolerance: 0.01
%   FixSelfIntersections: on
%
% Hatching
%   HatchingDistance: 0.5
%   HatchingAngle: 90
%   HatchingAngleOffset: 0
%
% Output options
%   HatchLines: OneWay
%   ZAxis: Piezo
%   Exposure: Variable
%   InvertZAxis: on
%   WritingDirection: Up
%   ScanMode: Galvo
%

% BLOCK 0|0|0
include top slab_files\top slab_0_0_0.gwlb
```

# Appendix B: Pillar shrinkage and Young's modulus experiments

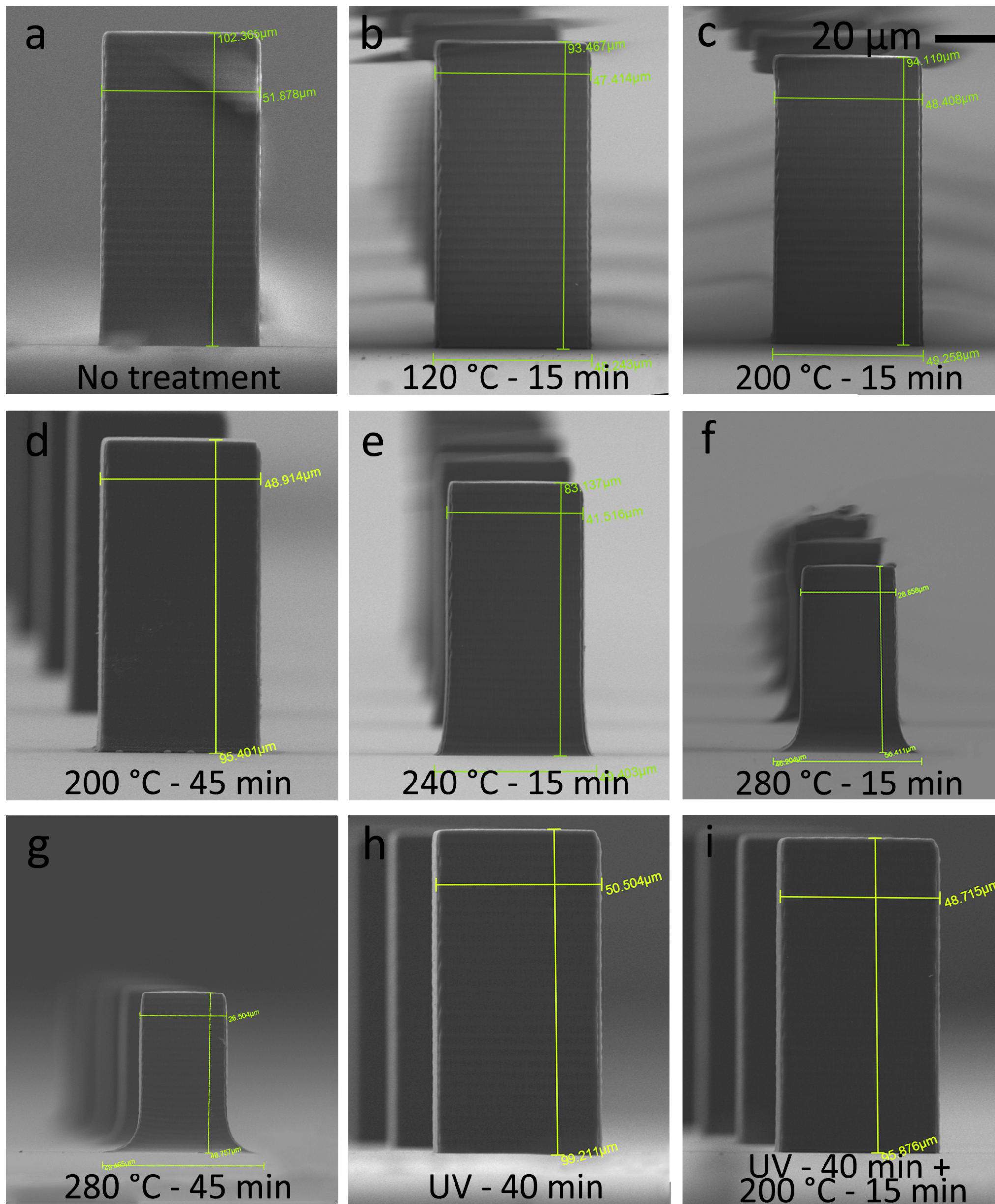


Figure B.1: Volumetric shrinkage visualized: SEM pictures of IP-S pillars after different post-development treatments. Images shown have equal scaling.

Table B.1: Young's modulus and volumetric shrinkage of IP-S pillars after different post-development treatments.

| Treatment | Young's modulus ($GPa$) n=25 | Volumetric shrinkage (%) n=5 |
|---|---|---|
| No treatment | $2.34 \pm 0.14$ | 0 |
| 120°C - 15 min | $3.48 \pm 0.21$ | 16.2 |
| 200°C - 15 min | $3.57 \pm 0.20$ | 11.2 |
| 200°C - 45 min | $3.22 \pm 0.16$ | 7.8 |
| 240°C - 15 min | $3.53 \pm 0.32$ | 43.2 |
| 280°C - 15 min | $3.29 \pm 0.26$ | 81.2 |
| 280°C - 45 min | $2.88 \pm 0.16$ | 86.1 |
| UV light 40 min | $3.30 \pm 0.16$ | 0 |
| UV light 40 min + 200°C - 15 min | $3.14 \pm 0.15$ | 9.2 |

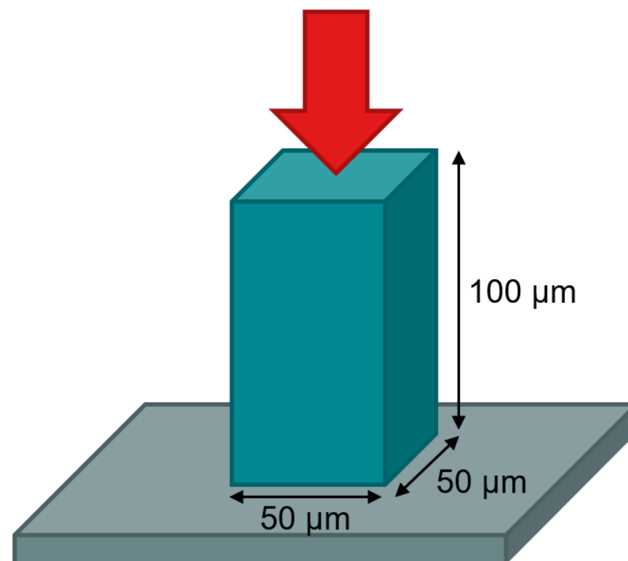


Figure B.2: Experimental approach for pillar Young's modulus quantification.

# Appendix C: Resonator characterization data

Table C.1: Resonance frequency and quality factor of thick cantilevers and bridges with varying length printed on three different substrate materials.

| **Substrate** | **Beam type** | **Length ($\mu m$)** | $f_{R1}$ **($kHz$)** | **Q n=5** |
|---|---|---|---|---|
| Silicon {100} | Cantilever thick | 50 | $1485 \pm 25$ | $747 \pm 267$ |
| | | 100 | $454 \pm 10$ | $702 \pm 242$ |
| | | 150 | $218 \pm 1$ | $590 \pm 230$ |
| | | 200 | $123 \pm 2$ | $376 \pm 261$ |
| | | 250 | $79 \pm 2$ | $166 \pm 81$ |
| | | 300 | $55 \pm 1$ | $31 \pm 7$ |
| | Bridge thick | 150 | $1227 \pm 16$ | $703 \pm 241$ |
| | | 200 | $746 \pm 17$ | $617 \pm 296$ |
| | | 250 | $486 \pm 15$ | $663 \pm 246$ |
| | | 300 | $365 \pm 4$ | $517 \pm 237$ |
| SiC-6H | Cantilever thick | 50 | $1478 \pm 26$ | $700 \pm 248$ |
| | | 100 | $455 \pm 3$ | $1126 \pm 629$ |
| | | 150 | $216 \pm 0$ | $516 \pm 89$ |
| | | 200 | $122 \pm 4$ | $178 \pm 224$ |
| | | 250 | $77 \pm 5$ | $212 \pm 75$ |
| | | 300 | $55 \pm 4$ | $69 \pm 39$ |
| | Bridge thick | 150 | $1214 \pm 34$ | $618 \pm 229$ |
| | | 200 | $735 \pm 28$ | $514 \pm 148$ |
| | | 250 | $485 \pm 11$ | $464 \pm 183$ |
| | | 300 | $355 \pm 11$ | $557 \pm 237$ |
| 3DM TOUGH clear | Cantilever thick | 50 | $1323 \pm 15$ | $429 \pm 80$ |
| | | 100 | $440 \pm 11$ | $391 \pm 148$ |
| | | 150 | $226 \pm 28$ | $396 \pm 121$ |
| | | 200 | $120 \pm 8$ | $114 \pm 50$ |
| | | 250 | $69 \pm 2$ | $79 \pm 67$ |
| | | 300 | $52 \pm 0$ | $106 \pm 63$ |
| | Bridge thick | 150 | $1176 \pm 14$ | $323 \pm 50$ |
| | | 200 | $704 \pm 6$ | $357 \pm 48$ |
| | | 250 | $459 \pm 0$ | $914 \pm 55$ |
| | | 300 | $319 \pm 3$ | $429 \pm 115$ |

Table C.2: Resonance frequency and quality factor of different beam types with varying length printed on Silicon with and without thermal treatment at 200°C for 15 minutes.

| Treatment | Beam type | Length ($\mu m$) | $f_{R1}$ ($kHz$) | Q n=5 |
|---|---|---|---|---|
| No treatment | Cantilever thick | 50 | 1485 ± 25 | 747 ± 267 |
| | | 100 | 454 ± 10 | 702 ± 242 |
| | | 150 | 218 ± 1 | 590 ± 230 |
| | | 200 | 123 ± 2 | 376 ± 261 |
| | | 250 | 79 ± 2 | 166 ± 81 |
| | | 300 | 55 ± 1 | 31 ± 7 |
| | Bridge thick | 150 | 1227 ± 16 | 703 ± 241 |
| | | 200 | 746 ± 17 | 617 ± 296 |
| | | 250 | 486 ± 15 | 663 ± 246 |
| | | 300 | 365 ± 4 | 517 ± 237 |
| | Cantilever thin | 50 | 886 ± 26 | 431 ± 167 |
| | | 100 | 213 ± 8 | 507 ± 84 |
| | Bridge thin | 100 | 1295 ± 16 | 535 ± 216 |
| | | 150 | 575 ± 6 | 580 ± 310 |
| | | 200 | 320 ± 19 | 611 ± 323 |
| | | 250 | 222 ± 11 | 623 ± 71 |
| | | 300 | 135 ± 8 | 136 ± 38 |
| 200°C - 15 min | Cantilever thick | 50 | 1565 ± 20 | 764 ± 355 |
| | | 100 | 473 ± 8 | 993 ± 139 |
| | | 150 | 230 ± 2 | 629 ± 252 |
| | | 200 | 130 ± 0 | 144 ± 24 |
| | | 250 | 88 ± 4 | 74 ± 33 |
| | | 300 | 60 ± 1 | 65 ± 25 |
| | Bridge thick | 150 | 1218 ± 20 | 510 ± 40 |
| | | 200 | 755 ± 8 | 826 ± 238 |
| | | 250 | 502 ± 9 | 766 ± 183 |
| | | 300 | 363 ± 3 | 580 ± 332 |
| | Cantilever thin | 50 | 1028 ± 27 | 668 ± 194 |
| | | 100 | 251 ± 8 | 637 ± 186 |
| | Bridge thin | 100 | 1357 ± 27 | 729 ± 118 |
| | | 150 | 640 ± 16 | 749 ± 197 |
| | | 200 | 371 ± 3 | 770 ± 343 |
| | | 250 | 245 ± 27 | 577 ± 174 |
| | | 300 | 181 ± 7 | 506 ± 328 |

Table C.3: Resonance frequency and quality factor of narrowed thin bridges with varying length printed on Silicon with and without thermal treatment at 200°C for 15 minutes.

| Treatment | Beam type | Length ($\mu m$) | $f_{R1}$ ($kHz$) | Q n=5 |
|---|---|---|---|---|
| No treatment | Narrowed bridge thin | 100 | 1472 ± 73 | 538 ± 94 |
| | | 150 | 676 ± 17 | 698 ± 425 |
| | | 200 | 361 ± 13 | 522 ± 312 |
| | | 250 | 233 ± 4 | 769 ± 320 |
| | | 300 | 147 ± 12 | 160 ± 34 |
| 200°C - 15 min | Narrowed bridge thin | 100 | 1541 ± 20 | 526 ± 105 |
| | | 150 | 740 ± 16 | 765 ± 337 |
| | | 200 | 424 ± 7 | 1819 ± 437 |
| | | 250 | 261 ± 14 | 466 ± 98 |
| | | 300 | 163 ± 5 | 242 ± 229 |

# Appendix D: Resonator deflection

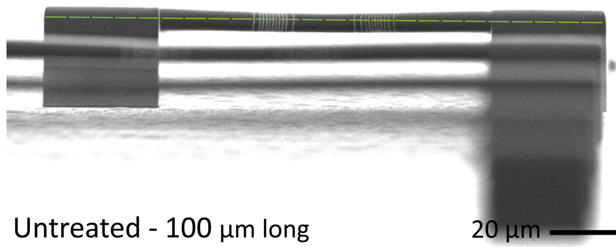


Figure D.1: Visualized deflection of narrowed bridge 100 $\mu m$ long untreated.

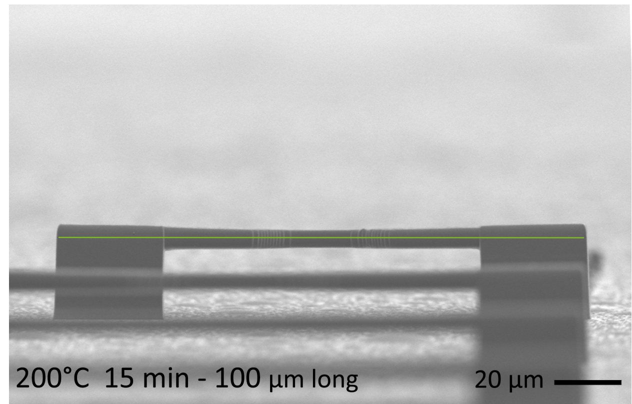


Figure D.2: Visualized deflection of narrowed bridge 100 $\mu m$ long 200°C - 15 min.

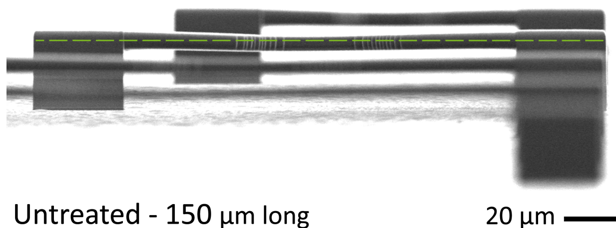


Figure D.3: Visualized deflection of narrowed bridge 150 $\mu m$ long untreated.

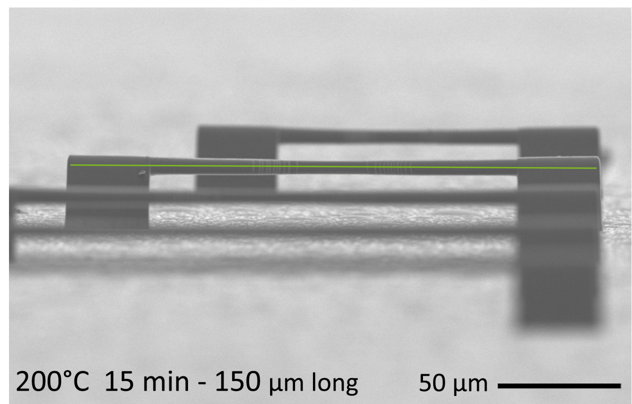


Figure D.4: Visualized deflection of narrowed bridge 150 $\mu m$ long 200°C - 15 min.

Figure D.5: Visualized deflection of narrowed bridge 200 $\mu m$ long untreated.

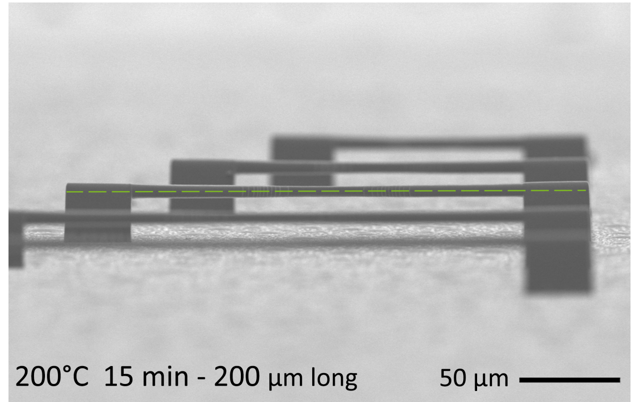
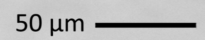


Figure D.6: Visualized deflection of narrowed bridge 200 $\mu m$ long 200°C - 15 min.

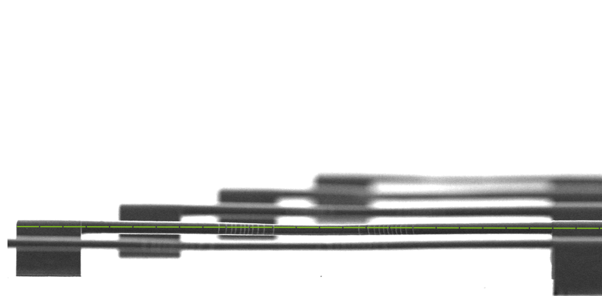
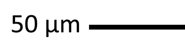


Figure D.7: Visualized deflection of narrowed bridge 250 $\mu m$ long untreated.

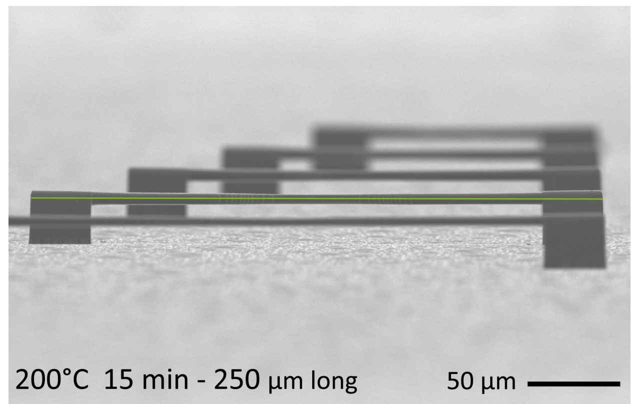
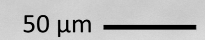


Figure D.8: Visualized deflection of narrowed bridge 250 $\mu m$ long 200°C - 15 min.

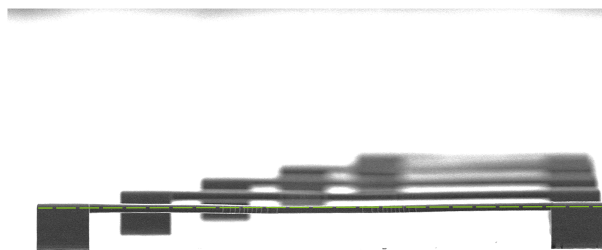
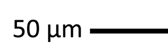


Figure D.9: Visualized deflection of narrowed bridge 300 $\mu m$ long untreated.

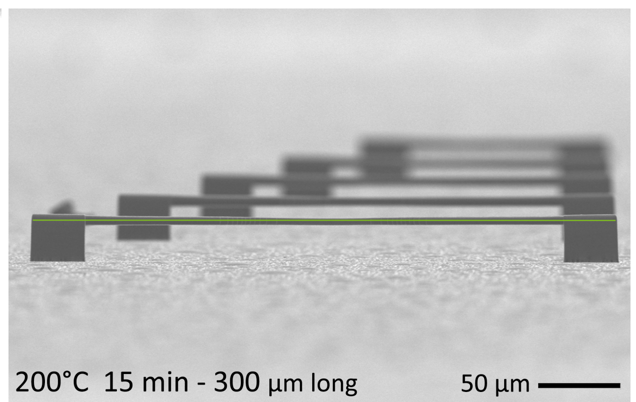
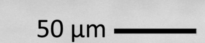


Figure D.10: Visualized deflection of narrowed bridge 300 $\mu m$ long 200°C - 15 min.

# Appendix E: Polymer substrates adhesion experiment

## E.1. Methodology

The adhesion strength of IP-S pillars on two substrate materials was quantified to determine the best DLP 3D printed polymer material for the fluidic interface. The following two materials we tested because of their high resolution in DLP 3D printing: HTM-140v2 and 3DM TOUGH clear. Additionally, gold sputtering on the substrate materials was performed to determine the influence of the $2nm$ gold layer on the adhesion strength of the IP-S pillars. This gold layer is considered necessary for printing SMRs on top of fluidic substrates.

The experimental approach for determining adhesion strength is shown in Figure E.1, where pillars were pushed from the side until they detached from the substrate. The detachment was apparent in the force-displacement curve and was confirmed visually by microscopic imaging. See Figure E.2 for confirmation of detachment.

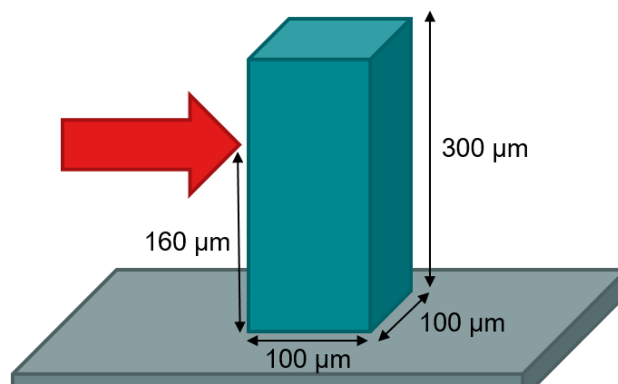


Figure E.1: Experimental approach for pillar adhesion strength quantification.

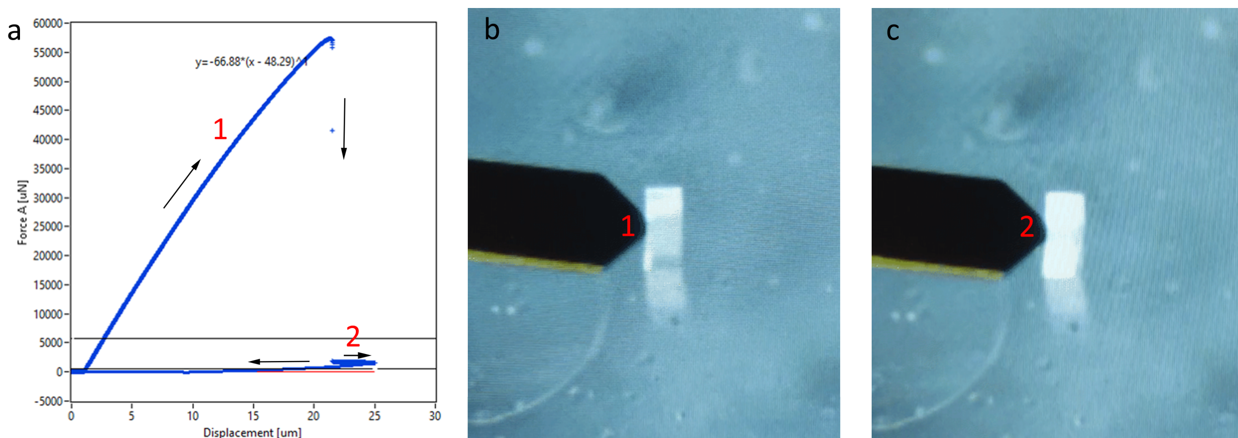


Figure E.2: Pillar adhesion strength quantification confirmation of detachment. (a) Raw data confirmation of detachment in displacement force plot, arrows show temporal order. (b) Visual confirmation before detachment. (c) Visual confirmation after detachment.

## E.2. Results and conclusions

The adhesion strength of IP-S pillars 3D printed on top of two substrate materials with and without gold sputtering is shown in Table E.1 and Figure E.3. Two conclusions could be drawn from this experiment:

- 3DM TOUGH clear has a better adhesion strength as a substrate to IP-S structures than HTM-140v2.
- The $2nm$ sputtercoated gold layer decreases the adhesion strength of IP-S on both substrate materials.

Table E.1: Pillar adhesion strength for different substrate materials with and without a sputtered gold layer of 2nm.

| Substrate material and top layer | Adhesion strength ($MPa$) | n=5 |
|---|---|---|
| HTM-140 v2 | 8.1 $\pm$ 6.1 | |
| HTM-140 v2 + 2nm gold | 2.0 $\pm$ 2.0 | |
| 3DM TOUGH clear | 55.8 $\pm$ 5.1 | |
| 3DM TOUGH clear + 2nm gold | 27.5 $\pm$ 3.7 | |

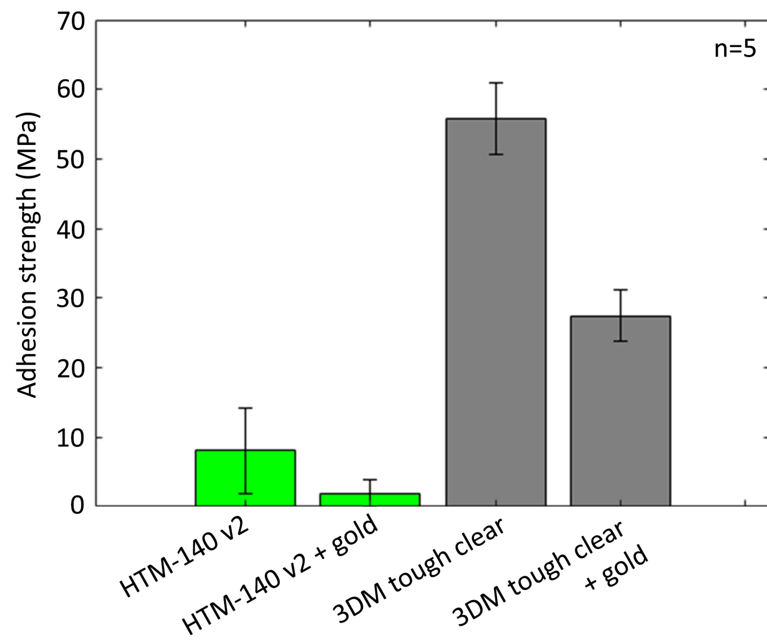


Figure E.3: Pillar adhesion strength for different substrate materials with and without a sputtered gold layer of 2nm.